2013

STRUCTURAL TAILORING OF NANOPOROUS METALS AND STUDY OF THEIR MECHANICAL BEHAVIOR

Lei Wang
University of Kentucky, lwa222@uky.edu

STUDENT AGREEMENT:

I represent that my thesis or dissertation and abstract are my original work. Proper attribution has been given to all outside sources. I understand that I am solely responsible for obtaining any needed copyright permissions. I have obtained and attached hereto needed written permission statements(s) from the owner(s) of each third-party copyrighted matter to be included in my work, allowing electronic distribution (if such use is not permitted by the fair use doctrine).

I hereby grant to The University of Kentucky and its agents the non-exclusive license to archive and make accessible my work in whole or in part in all forms of media, now or hereafter known. I agree that the document mentioned above may be made available immediately for worldwide access unless a preapproved embargo applies.

I retain all other ownership rights to the copyright of my work. I also retain the right to use in future works (such as articles or books) all or part of my work. I understand that I am free to register the copyright to my work.

REVIEW, APPROVAL AND ACCEPTANCE

The document mentioned above has been reviewed and accepted by the student's advisor, on behalf of the advisory committee, and by the Director of Graduate Studies (DGS), on behalf of the program; we verify that this is the final, approved version of the student's dissertation including all changes required by the advisory committee. The undersigned agree to abide by the statements above.

Lei Wang, Student

Dr. T John Balk, Major Professor

Dr. Fuqian Yang, Director of Graduate Studies

STRUCTURAL TAILORING OF NANOPOROUS METALS AND STUDY OF THEIR MECHANICAL BEHAVIOR

DISSERTATION

A dissertation submitted in partial fulfillment of the requirements for the degree of Doctor of Philosophy in the College of Engineering at the University of Kentucky

By
Lei Wang

Lexington, KY

Director: Dr. T. John Balk, Professor of Chemical and Materials Engineering

Lexington, KY

2013

ABSTRACT OF DISSERTATION

STRUCTURAL TAILORING OF NANOPOROUS METALS AND STUDY OF THEIR MECHANICAL BEHAVIOR

Student: Lei Wang
Advisor: Dr. T. John Balk

University of Kentucky, Chemical and Materials Engineering, Lexington, KY

Nanoporous (np) metals and alloys are the subject of increasing research attention due to their high surface-area-to-volume ratio. Numerous methods exist to create np metals, with dealloying being a common approach. By dissolving one or more elements from certain alloy systems, porous structure can be generated. Utilizing this method, multiple np metals, including np-Ni, np-Ir, and np-Au were created. By carefully adjusting precursor type and dealloying conditions for each system, nanoporous Ni/Ir/Au with different morphologies and even controllable ligament/pore size were achieved.

The mechanical behavior of porous materials is related to their fully dense counterparts by scaling equations. Established scaling laws exist and are widely applied for low relative density, micro- and macro-scale open-cell porous materials. However, these laws are not directly applicable to nanoporous metals, due to higher relative density and nanoscale cells. In this study, scaling laws were reviewed in light of the thermomechanical behavior of multilayer np-Ir thin films subjected to thermal cycling. Thermal cycling allows measurement of biaxial modulus from thermoelastic segments, and also causes film thickness to contract, with increases in relative density. A modified scaling equation was generated for biaxial modulus of np-Ir, and differed significantly from the classic equation.

KEYWORDS: Nanoporous, Nickel, Iridium, Scaling law, Thermomechanical behavior

STRUCTURAL TAILORING OF NANOPOROUS METALS AND STUDY OF THEIR MECHANICAL BEHAVIOR

By

Lei Wang

T. John Balk, Ph. D.

Director of Dissertation

Fuqian Yang, Ph. D.

Director of Graduate Studies

November 23, 2013

ACKNOWLEDGEMENTS

I am very thankful to all the people who had helped me to finish my doctoral study.

First, I would like to start with my Ph. D. advisor Dr. T. John Balk. Thanks for advising, helping me becoming a better researcher in Materials Science. Thanks for spending time to review every single sentence in all my papers. Thanks for encouraging me while I encountered troubles in research.

I thank the members of my committee: Dr. Y.T. Cheng, Dr. Stephen Rankin, Dr. Gang Cao, and Dr. Todd Hastings. Thanks for your time to attend my qualifying exam. Thanks for the helpful discussion. And thanks for being in my committee and reading my dissertation.

I would also like to thank my colleagues as well as friends: Nicolas Briot, Phillip Swartzentruber, Xu Jiang, Dr. Wayne Li, Dr. Ye Sun and other members in my group. Thanks for sharing discussion, knowledge and ideas, and collaboration with experiment and research. Thanks for making the lab life colorful.

I am also thankful to many other people in department. Thanks to Dr. Jia Ye and Larry Rice for teaching me using electron microscopes. Thanks to Dr. Tongguang Zhai, Dr. Matthew Beck, and other professors who gave me classes and answering my questions.

I also would like to thank my beloved family. Thanks to my parents and younger sister. Even you are far away in China, but without your support I won't finish my doctoral study. Special thanks to my dear husband: Shufeng. Thanks for listening to me talking over my research. Thanks for helping me preparing every single presentation I gave. Thanks for being with me in the last 5 years.

Thanks for Kentucky Science and Engineering Foundation, National Science Foundation, University of Kentucky Graduate School and Department of Chemical and Materials Engineering for their financial support of this work.

TABLE OF CONTENT

List of Tables

List of Figures

1 Introduction

1.1 Motivation

It has been widely accepted that materials science, together with energy technology and information technology, is one of the three pillars of the modern civilization. Materials have played an essential role in human development, not only in the modern times, but throughout human history. Historians divided human prehistory into three periods, according to their respective tool-making technologies, namely Stone Age, Bronze Age, and Iron Age. Indeed, materials science defines the level of human civilization. Materials science is one of the oldest sciences on earth. However, it was not until the second industrial revolution that materials science became an independent discipline. Since then it has driven the technological revolution further and further. These inventions of new materials have transformed the way we experience our world, e.g., semiconductors in the electronic devices, high temperature alloys in the air and space crafts, and bio-materials in medicine.

Beginning in the mid-20th century, humans have entered a brand new stage of world exploration. The development of space technology allows people explore the vast expanses of space, where distance is measured by light-year. Meanwhile, nanotechnology enables people work with materials or devices at molecular, atomic, and even sub-atomic level. Recently, the rapid development of semiconductor industry has filtered the concept of ‘smaller is better’ into everyone’s minds. Nano-science and nano-technology, the keywords of 21st century, represent a new direction of materials science.

Nano-materials have features with dimensions from sub-nanometer to several hundred nanometers [1]. Although 'nano' is a popular word in everyday life of 21st century, not everyone understands what it really means. For comparison, if you are trying to see a 1 nm feature in a 1 cm×1 cm sample, the difficulty is no less than trying to find a human hair in Tiananmen Square. However, thanks to the advanced technologies, such as scanning electron microscope (SEM), transmission electron microscope (TEM) and scanning tunneling microscope (STM), people nowadays are able to visualize, and even manipulate, atoms under 1 nanometer. It is hard to predict how nanotechnology could change our life over the next decade, but no one will doubt that it's a key technology for the future.

1.2 The study of nanoporous metals

The study of nanoporous metals (np-metals) is one branch of nanotechnology. Np-metals are individual metal or alloy frameworks that support a nanoporous structure. The size of pores in np-metals is typically less than 100 nm. Due to their high surface-area-to-volume ratio, np-metals are highly appreciated as functional materials, such as catalysts [2, 3], sensors [4, 5] and energy storage materials [6]. One good example is Raney Nickel, the commercial catalyst in oil hydrogenation used in industry for more than 80 years [7].

The use of np-metal can be traced back to 80 years ago, however, the study of np-metals is relatively new. The earliest study of np-metal is by Pickering and Swan in 1960's [8]. They utilized TEM to characterize nanoporous gold (np-Au). Up to date, many metals and alloys have also been produced in np forms, including np-Cu, np-Ag, np-Pt, np-Pd, etc [9-12]. However, most of present studies are focused on np-Au, due to the noble chemical behavior of Au and ease of fabrication.

In order to implement np-metals in an application environment, the understanding of their mechanical behavior is important. Np-metals are considered to be brittle intuitively. However, recent studies in np-Au suggested it has some extraordinary mechanical properties. Researchers found that np-Au is brittle macroscopically, but ductile at the nanoscale [13], and the ligaments have a relatively high yield strength [14] than typical value of bulk Au. These preliminary works initiated more studies on mechanical behavior of np-metal, but many issues remained. First no standard method to measure strength of np-metals. Nanoindentation is the most commonly used method, due to the ease in sample preparation, but appeared to overestimate strength [15, 16]. Second controversies existed when using scaling equations by Gibson and Ashby to calculate ligament strength. Scaling equation is a relationship between mechanical properties of np-metals to those of ligament materials (bulk dense materials). Many researchers found that Gibson and Ashby's scaling equation may not be applicable to np-metals, because they were designed for very low relative density porous materials (<0.1), but np-metals typically have relative density of 0.2-0.4 [17]. More discussion about scaling equation is in Chapter 2.5.

To develop further knowledge of np-metal, nanoporous nickel (np-Ni) and nanoporous iridium (np-Ir) were studied in this research. Ni and Ir are both fcc metals. Mechanical behavior of fcc bulk metals such as Ni, Cu, Pd, and Ir are well documented, providing useful information to study their nanoporous counterparts. Because bulk Ni and Ir have higher yield strength than Au, their deformation behavior were expected differ. The study included fabrication and mechanical testing of np-Ni and np-Ir, as well as detailed microstructural characterization using electron microscopy. These results provided an

improved understanding in fabrication of nanoporous metals and study of their mechanical properties.

1.3 Outline of this doctoral work

The following is a brief outline of this thesis.

Chapter 1 presents the motivation and gives a brief introduction of this research;

Chapter 2 provides useful information of the theoretical background of the study. It includes fundamentals of nanoporous metals and dealloying, applications of np metals, and also general background, i.e. elastic and plastic deformation of metals, atomic diffusion in metals, relaxation behavior of thin film, scaling law, stress in thin films, relax behavior of thin films and at last the size effect of nanoscale mechanical behavior.

Chapter 3 describes experimental methods at a fundamental level. It includes thin film techniques, characterization methods, such as SEM, TEM, XRD, and mechanical test methods for nanoporous (np) metals.

Chapter 4-7 contains the major works of this thesis. It includes the study of thin film np-Ni (Chapter 4), the study of a multilayer fabrication approach (Chapter 5), the study of thin film np-Ir (Chapter 6), and the study of bulk np-Ir (Chapter 7).

Chapter 8 is a summary of all the works presented in this thesis. It includes conclusions and future work.

2 Background

This chapter introduces various aspects of nanoporous (np) metals, including dealloying, applications, scaling law, thin film stress, diffusion, size effect, etc., with the purpose of providing the background to better understand the remaining of this thesis.

2.1 Nanoporous metals

Even porous materials have existed in earth for ages, e.g. zeolites and sponge, the study of them is relatively new. According to the official standard of International Union of Pure and Applied Chemistry (IUPAC), porous materials can be classified as micropores (<2 nm), mesopores (>2 nm and <50 nm), and macropores (>50 nm) based on pore diameter. Nanoporous materials actually fall into all the three catalogs. They typically exhibit porosities (volume ratio of pore space to the total volume of the material) greater than 0.4, and pore diameters between 1-100 nm [18].

Nanoporous metals (np-metals) are nanoporous materials made of metals. They are sometimes described to be a two-phase system, i.e., metal ligaments and pores. For np-metals prepared by dealloying, they appear to be completely irregular in morphology, as shown in Figure 2.1 [19, 20]. Figure 2.1a and b show plan-view SEM and TEM image of a thin film nanoporous gold (np-Au), which are typical morphologies for a film thickness less than 100 nm. Figure 2.1c is a real 3-D structure of np-Au obtained from electron tomography, and it displays the interconnections of gold ligaments and nanopore channels [19, 20].

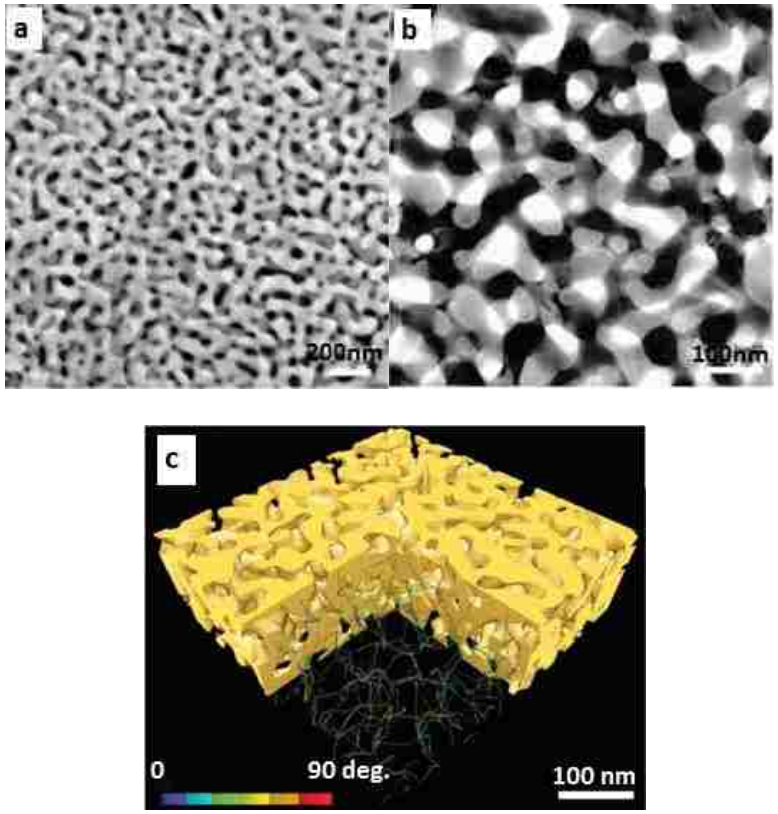

Figure 2.1. Morphologies of np-Au [19,20]. (a). Plan view scanning electron microscopy (SEM) images of np-Au; (b). Plan view transmission electron microscopy (TEM) images of np-Au; (c). Three-dimensional structure of np-Au imaged by electron tomography. The bottom part shows the skeletal network of gold ligament. The various colors of the skeletal network represent the deviation angles of the ligaments from the surface normal as indicated in the color bar.

Common terminologies used to evaluate a nanoporous structure include relative density and aspect ratio. Relative density is the ratio of porous materials density to that of fully dense material. It's equivalent to the volume ratio of ligament volume to the volume of the whole material. Aspect ratio is the ratio of ligament length to width. Note that ligament length is measured from middle points of two joint nodes. Typical nanoporous metals exhibit relative densities in the range 0.2-0.4 [17], and aspect ratio around 1.5-3 [21-23].

2.2 Dealloying

Even there are some natural porous materials, such as zeolites, wood and bones, np-metals are indeed synthetic. There are several methods available to produce np-metals [24, 25], with dealloying becoming a common approach. Dealloying refers to the selective dissolution of one or more components from an alloy. The sacrificial components are commonly the less noble (LN) elements since they are normally chemically active, and the remaining components are accordingly the more noble (MN) elements. However, it's not necessarily true in all the cases, e.g., making np-Ni from NiCu, where Cu is actually more noble than Ni [26].

Not all of the binary or trinary alloy system can yield nanoporous structure upon dealloying. Erlebacher summarized some basic shared characteristics if alloy systems can become nanoporous during dealloying: (1). the potentials required to dissolve each component in its pure form must be separated by a few hundred millivolts. The sacrificial elements are less noble (LN), and the remaining element is more noble (MN), as we discussed above. (2). the composition is usually rich in less noble components. (3). the system must be homogeneous before dealloying, i.e. only one phase for the precursor alloy. (4). diffusion of MN atoms at the solid/electrolyte interface must be sufficiently fast [27].

Depending on if voltage is applied in the process, dealloying can be classified as free corrosion and electrochemical dealloying. Dealloying condition, i.e. concentration of etchants, dealloying temperature and time can affect the dealloyed structure in ligament size and aspect ratio.

The earliest use of dealloying can be traced to fabrication of Raney nickel from alloys by dealloying Ni-Al or Ni-Si 83 years ago [28]. However, the earliest study in

dealloying was by Pickering and Swann in 1960's when they fabricated np-Au from Au alloys [29, 30]. They were also the first to use transmission electron microscopy (TEM) to study the structure of dealloyed materials, demonstrating a nanoporous structure in the dealloyed sample. In 1979, Forty successfully created freestanding np-Au film by dealloying a AuAg alloy in nitric acid [31]. Two key parameters associated with dealloying, namely, critical potential and parting limit, were determined and evaluated by Sieradzki and Newman, by studying the electrochemical behavior of AuAg alloy in dealloying [32, 33].

Critical potential is the voltage threshold above which dealloying current started to increase dramatically. Figure 2.2 shows the current density vs. voltage curve during dealloying, and the critical voltage is located at the knee point where the current density suddenly increases [32]. However, the critical potential is not clearly defined, as indicated in Figure 2.2, the region between the dashed lines indicated ambiguity in defining a critical potential. One method involves drawing the tangent line of the upper linear portion of the current density vs. potential curve, and the intersection on the voltage axis is defined as the critical potential. The other way to determine the critical potential is to find the potential corresponding to a constant current/current density.

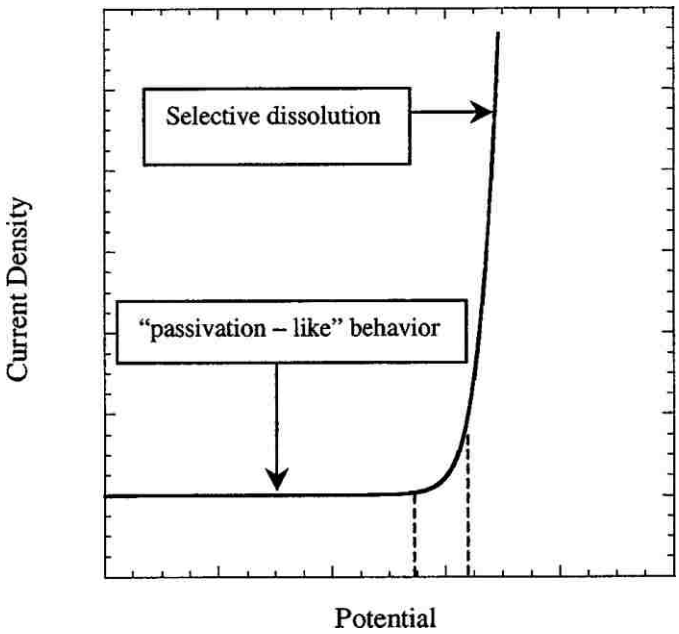

Figure 2.2. A schematic drawing of the current density vs. voltage in dealloying of an alloy. The plot is taken from work of Sieradzki et al [32]. Critical potential is the voltage threshold above which dealloying current increases dramatically, as indicated as the region between two dashes line.

Parting limit is defined as the content of non-sacrificial metal in the precursor alloy above which dealloying cannot occur. For dealloying of AuAg to fabricate np-Au, the parting limit is around 40 at.% Au [33].

These preliminary studies attracted more research interests in this field. To date, dealloying has been successfully applied in fabrication of np-Pt [34], np-Pd [12, 35], np-Cu [10], np-Ag [36], np-Ir [37] and np-Ni [38]. In 2001, Erlebacher et al. described an atomistic model of dealloying evolution [39], published in a natural paper. According to his study, dealloying is a process, in which two mechanisms happen simultaneously, i.e. dissolution of sacrificial element atoms and uphill diffusion of noble metal elements. This work was widely accepted as a successful model to describe porosity/ligament formation during dealloying.

2.3 Application of nanoporous metals

Due to the high surface-to-volume ratio inherent to the nanoscale porous structure, Many believed np-metals have great potentials for application as catalysts [3], sensors [4, 40], actuators [5, 41], and energy storage materials [6, 42]. Raney nickel is a classic example of np-metal catalyst. It's commonly used as the commercial industrial catalyst in hydrogenation of vegetable oil. Other examples of np-metals as functional materials are presented in the following sections.

2.3.1 Nanoporous metals as catalysts

In addition to Raney nickel, nanoporous Pt (np-Pt) or Pt-based alloys were also used as catalyst. They worked as electrocatalyst for oxidation of small organic molecules and also oxygen reduction [43]. Another example of np-metal catalysts is nanoporous gold (np-Au). Despite the inertness of Au, np-Au actually had been demonstrated as a great catalyst for CO/CO_2 conversion even at low temperature [44].

2.3.2 Nanoporous metals as sensors and actuators

Due to their great catalytic performance in reduction and oxidation of organic molecules, np-Pt and np-Au were also studied as sensors for detecting H_2O_2, and measuring PH [45].

Pd is used as a commercial H_2 sensor. Np-Pd has been demonstrated to be more promising for detecting H_2 due to the nanoporous structure. It had a shorter response time than dense Pd film in H_2 adsorption and desorption [12].

The application of np-metals as actuators is attribute to the high stress/strain sensibility of the porous structures. The examples can be found in np-Au as well [5, 41].

2.3.3 Nanoporous metals as energy storage materials

Energy storage is one of the hottest topics in this century. Nanoporous materials have received some research interest in their electrochemical properties, benefited from a potential energy density raise due to the high surface-area-to-volume ratio. Researchers have reported ultra-high capacitance of np-Pt [46] and np-Au [6].

2.3.4 Utilizing nanoporous metals 3-D architectures

In addition to using np-metal directly as functional materials, the application of np-metals is also benefited from its three dimensional (3D) structure. The 3-D porous structure in np-metals doesn't only increase the surface area, also offers a conductive network with adequate void space. It's reported that np-Au coated with a thin layer of polypyrrole exhibited high energy density, and also improved stability. It's a promising candidate material for super-capacitors [47]. Other example is nanoporous Ni. A slightly elevated temperature annealing can form a thin NiO layer on the Ni surface. The Ni-cole-NiO-shell structure provided the material a high specific capacity [48]. The same idea can be adopted to other systems. For the new generation of energy storage materials, 3-D architecture will be a new trend [49]. One problem of Si electrode in Li-ion battery, i.e. the poor cycling behavior due to the large volume change during lithiation and delithiation, may be solved by utilizing the 3-D metal nanoporous structure (conformal coating Si on np-metal). Np-metal structure provides space to release the volume change, and also acts as a conductive 3-D network (electron collector).

2.4 Gibson and Ashby's scaling law

In order to implement nanoporous metals in a practical environment, a more fundamental understanding of their mechanical behavior is needed. It's relatively straight forward to measure the mechanical properties of np-metals, A^*. But problems remained when translating the properties of np-metals, A^*, to the solid ligament materials, A_s. Many researchers directly took over the relationships for low density open cell foams.

Among many works to explore the relation of mechanical properties of porous materials to those of the ligament materials [50-52], Gibson and Ashby's scaling law has be widely accepted and applied in study of np-metals [53]. According to the scaling law, mechanical properties, e.g., moduli and strength, of the porous materials A^* is related to the fully dense ligament materials A_s by the following equation,

$$\frac{A^*}{A_s} = C \cdot \left(\frac{\rho^*}{\rho_s}\right)^n \qquad \text{Equation 2.1}$$

where A^* and ρ^* are mechanical property and density of the porous material respectively, and A_s and ρ_s are mechanical property and density of the ligament material (corresponding dense materials). $\frac{\rho^*}{\rho_s}$ is relative density of the porous material. As implied in its format, it's the ratio of the density of the porous material to that of its corresponding fully dense material. n, and C are empirical constants. For open cells foams with low relative density, Gibson and Ashby fount that n=2 or 1.5, respectively for relative modulus and relative strength. C is highly related to the geometry of the porous structure, and empirical data indicated that C=1 or 0.3, respectively for relative modulus and relative strength, over a broad range of relative density (0.01 to 1) [53].

For example, yield strength of a single crystal np-Au column sample, σ^*, is measured as 100 MPa from a nano-indentation test. According to the scaling equation, the calculated yield strength of the Au ligaments, σ_s, is 1.5 GPa. Here, $\frac{\rho^*}{\rho_s}$ is equivalent to the volume percentage of the gold in the porous sample, which is 36%. *C* and *n* are 0.3 and 1.5 respectively. The calculated yield strength (1.5 GPa) is 10-100 times larger than typical yield strength of bulk Au, and is close to the theoretical shear strength of Au (4-5 GPa). This example is taken from a published paper by Volkert et al [54]. Other researchers also found the extremely high yield strength of np-Au in nano-indentation experiments both in bulk and film specimens [55-57].

With more and more researches in this field, questions arose regarding viability of the classic Gibson and Ashby's scaling equation. As mentioned earlier, Gibson and Ashby's scaling equation was derived for low density open cell foams ($\frac{\rho^*}{\rho_s} < 0.1$). However, the relative density of nanoporous metals usually falls into the range of 0.2-0.4 [17]. At low relative densities, the deformation of open-cell foams is primary due to cell-wall bending. However, as relative density increases, the contribution of cell-wall extension or compression becomes more significant [53]. Meanwhile, the classic scaling equation applies to porous structure in length scale larger than micrometer. It's not true for np metals neither. The typical ligaments size of nanoporous metals is 1-100 nm, where the dislocation nucleation and motion are subject to different constraints. Thus the size effect must be considered [55]. More discussion about size effect is in section 2.9. Therefore, Gibson and Ashby's scaling equation must be revised when applying to np-metals.

2.5 Stress in thin films

An as-deposited film is stressed even no external force is applied to it. The internal stress of thin film is generated in deposition process. Generally there are two sources for the internal stress. One is the lattice misfit. The other is the mismatch in thermal expansion coefficient [58]. For epitaxial films, lattice misfit, f, causes the major stress in films. However, it is not a concern for the sputtered films on Si wafers, due to an amorphous Si oxide/nitride layer on the surface. Instead, thermal effect makes the major contributions. In deposition, the film is slightly heated due to heat generated in sputtering. When the film is cooled to room temperature after sputtering, a thermal stress is created. For a bilayer film/substrate, usually the substrate is more rigid than film, and the film is constrained by the substrate, and therefor results in a tensile stress. The stress is given by

$$\boldsymbol{\sigma_f(T) = \frac{(\alpha_s - \alpha_f)\Delta T E_f}{1 - \nu_f}} \qquad \text{Equation 2.2}$$

where α_s and α_f are thermal expansion coefficients of substrate and film respectively. And ΔT is the temperature differential. E_f and ν_f are Young's modulus and Poisson's ratio of the film.

2.6 Elastic and plastic deformation in metals

This section is not directly related to nanoporous (np) metals. But it's essential to understand the mechanical behavior of np metals.

When a metal sample is subjected to a uniaxial tensile force, it will undergo deformation. At the beginning, the small amount of deformation is recoverable, i.e. the sample returns to its original shape when the force is removed. This type of deformation is called elastic deformation. When the metal sample is deformed further, unrecoverable

deformation happens, and this type of deformation is called plastic deformation. During plastic deformation the metal atoms undergo permanent displacement.

2.6.1 Stress and strain in metals

In the tensile test discussed above, a uniaxial force *F*, is applied to the metal sample. Assume the sample is in a cylinder shape, with length l_0, and diameter d_0, as shown in Figure 2.3. The engineering stress σ, is defined as the average force per unit area. In this case, $\sigma = \frac{F}{\frac{\pi}{4}{d_0}^2}$. The cylinder sample is elongated in the direction of tensile force, and the engineering strain ε, is defined as the ratio of the total deformation to the original dimension of the sample. In this case, $\varepsilon = \frac{l-l_0}{l_0}$. l is the length of the sample after deformation.

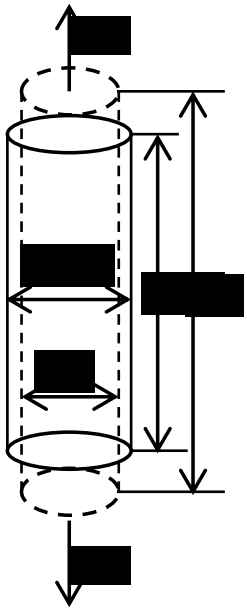

Figure 2.3. A sample of cylinder shape is under tensile force, *F*. The cylinder has a length of l_0 and diameter d_0 before applying the force, and after the tensile force it has a length of l and diameter of d.

In this tensile test, besides elongation, the metal sample also undergoes contraction in cross section. Poisson's ratio, *v*, is defined as the negative ratio of lateral strain to longitudinal strain. In this case, $\nu = -\frac{\varepsilon_{lateral}}{\varepsilon_{longitudinal}} = -\frac{\frac{d-d_0}{d_0}}{\frac{l-l_0}{l_0}}$. d is the diameter of the sample after deformation. It's worth noting that Poisson's ratio is only for elastic deformation. For most of materials, they have positive Poisson's ratios due to the opposite signs of $\varepsilon_{lateral}$ and $\varepsilon_{longitudinal}$. However it's not true always, and some materials have negative Poisson's ratios.

Additional to tension or compression test, a material can also be deformed by shear stress (see Figure 2.4). Shear stress, τ, is defined as the shear force per unit area, i.e. $\tau = \frac{F_S}{A}$. And shear strain, γ, is defined as the ratio of shear displacement to distance where shear stress acts, i.e. $\gamma = \frac{\Delta l}{l}$. Remember that shear stress is parallel to the face it's applied to, as shown in Figure 2.4, where tensile/compression stress is normal to the face it's applied to, as indicated in Figure 2.3.

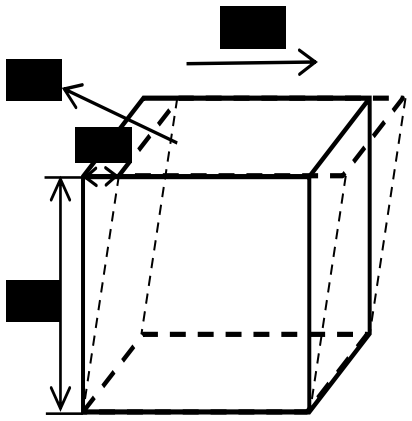

Figure 2.4. A sample in cubic shape is under shear force, F_s. The cubic has a length of l, and under shear force F_s, the upper face moved a distance of Δl.

In a tensile test, a tensile force is applied to a sample (usually in cylinder shape), and the engineering stress and strain are recorded and plotted out. A typical engineering stress and strain curve of a metal sample is shown in Figure 2.5. From this curve, some important mechanical properties of the sample are obtained.

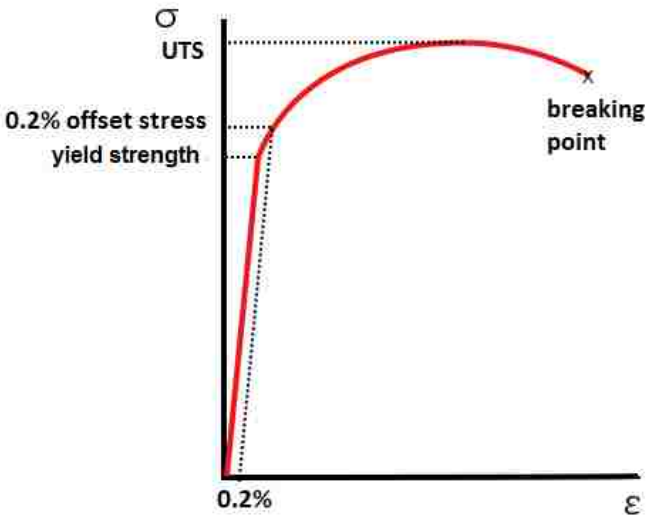

Figure 2.5. A classic engineering stress and strain curve of a metal sample. Yield strength, ultimate tensile strength (UTS) are indicated on the curve as well.

The first one is Young's modulus or elastic modulus. Young's modulus, *E*, is defined as the slope of the linear part, i.e. $E = \frac{\sigma}{\varepsilon}$. This linear part corresponds to elastic deformation in the sample. As discussed above, strain is recoverable in this region.

The second one is Yield strength. Yield strength corresponds to the transition stress from elastic deformation to plastic deformation. It's the beginning point of plastic deformation. However, sometimes transition point is ambiguous to determine the yield strength. In these cases, the yield strength is determined by the 0.2% offset stress, where 0.2% plastic strain takes place, as indicated in Figure 2.5.

The third one is ultimate tensile strength (UTS). The UTS is the maximum stress in engineering stress strain curve, as shown in Figure 2.5. After the yield point, the stress increases due to strain hardening until it reaches UTS. Beyond this point the sample starts necking until fracture. Notice that the UTS is an engineering stress. Actually beyond UTS, the true stress, i.e. force divided by actual cross section area, is still increasing, because the sample cross section area is decreasing dramatically after necking.

All of the properties above can be used to evaluate strength of a material. The ductility can be assessed by the elongation percentage in engineering stress and strain curve. Elongation is not the only way and sometimes is not sufficient to evaluate the ductility either. It's also noteworthy that Young's modulus is the only property all engineering stress and strain curves have. For brittle materials, they usually rupture before the stress reaches yield strength, and therefore yield strength and UTS are not available in their engineering stress and strain curves.

2.6.2 Dislocation

To early 20 century, researchers have realized that the plastic deformation of metals is primarily caused by atomic slip and twining. No matter which mode the materials deform with, the atomic planes slip over each other is the major process. For a perfect crystal, the theoretical shear strength for two atomic planes slip over each other is given approximately by,

$$\tau_{theoretical} = \frac{G}{2\pi} \qquad \text{Equation 2.3}$$

where G is the shear modulus of the crystal. However, the calculated theoretical shear strength is several orders larger than the shear stress obtained in practical experiments. This

puzzle remained unclear until 1930's when Orowan, Polanyi and Taylor introduced the concept of dislocation to explain plastic deformation.

Dislocation is one type of crystallographic defects, specifically line defect. There are two major types of dislocations. One is edge dislocation, and the other is screw dislocation. Edge dislocation can be imagined as a half plane of atoms introduced through middle of a crystal, as shown in Figure 2.6a [59]. While screw dislocation can be imagined as cutting a crystal along a plane and then slipping one half plane across the other by one atomic row distance, as shown in Figure 2.6b [59]. There are also mixed dislocations. As the name implied, they are mixture of edge and screw dislocations. One important character of dislocations is Burger's vector, $\vec{b}$. Burger's vector is to describe the magnitude and direction of the displacement a dislocation can cause in a crystal. As indicated in Figure 2.6, the Burger's vector of an edge dislocation is perpendicular to the dislocation line, and for a screw dislocation it's parallel to the dislocation line.

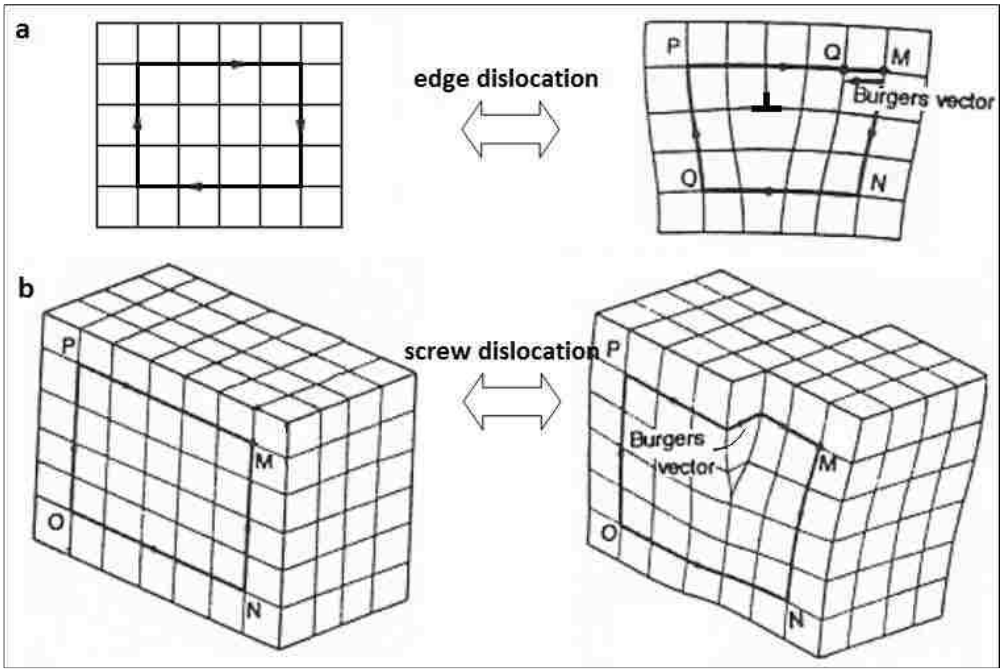

Figure 2.6. A schematic illustration of edge dislocation (a), and screw dislocation (b). The Burger's vectors of two kinds of dislocations are also shown in the drawing.

The presence of dislocations explained a lot of phenomena in plastic deformation. First, it explained why the practical yield strength is way lower than the theoretical shear strength. Due to dislocation, it doesn't have to break the entire atomic bonds of two planes to make them slip over each other. The plane can be moved by breaking one line of bonds each time, which causes the dislocation line move one Burger's vector forward. The energy required to move a dislocation line one Burger's vector is way less than that to break all bonds of two planes. Secondly, dislocation in a crystal is essential for strain hardening. For example, in tensile test, some dislocations escape from the surface and leaves plastic deformation in the crystal. At the meantime, new dislocations generate due to multiplication. For polycrystalline metals, the dislocations may pile up in grain boundary. It increases the resistance to further dislocation motion, and causes the so called 'strain hardening' in plastic deformation.

2.7 Diffusion in metals

Atomic diffusion is a thermally activated process. In perfect single crystal, diffusion occurs by lattice diffusion (bulk diffusion). There are two types of lattice diffusion, i.e. interstitial diffusion and substitutional diffusion. For interstitial diffusion, small atoms diffuse between the lattices of larger atoms, e.g. carbon atoms diffusion in steel. For substitutional diffusion, atoms can only move by substitute position with the other ones. Self-diffusion is one type of substitutional diffusion. The minimum energy required for lattice diffusion (no matter interstitial or substitutional diffusion) is called activation energy. The rate of diffusion, *K*, can be evaluated by Arrhenius equation:

$$k = A \cdot exp(-\frac{E}{RT}) \qquad \text{Equation 2.4}$$

where *E* is the activation energy, *A* is a prefix constant depending on the reaction, and *R* is the gas constant, *T* is absolute temperature.

In perfect crystal, the activation energy is very high. Therefore the diffusion rate at room temperature is too low to be noticed. However, as dislocation played a big role in plastic deformation, crystal defects also affect diffusion in similar way. For example, vacancies, one type of point defect, decreases the activation energy for lattice diffusion significantly.

In addition to lattice diffusion, there are grain boundary (GB) diffusion, dislocation diffusion, surface diffusions, etc. These four kinds of diffusions are illustrated in Figure 2.7. As you may notice, GB, dislocation, and surface are also defects in crystal. GB and surface can be imagined as plane defects. Just as vacancies, they are preferred diffusion paths. The activation energy of GB, dislocation and surface diffusions is usually lower than that of lattice diffusion.

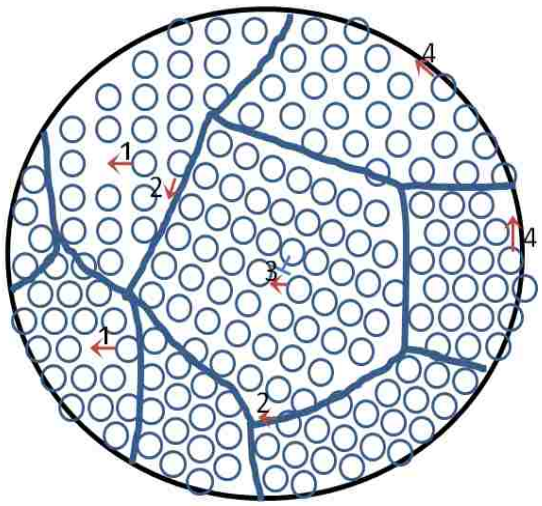

Figure 2.7. A schematic drawing of 4 types of diffusion: 1. lattice diffusion through vacancies; 2. grain boundary diffusion; 3. diffusion through dislocation; 4. surface diffusion.

The driving force of diffusion is usually considered as concentration gradient. According to it, atoms always diffuse to minimize the concentration differences. However, it's not true always. In 'up-hill' diffusion or 'spinodal decomposition', the atoms diffuse against concentration gradient. Instead, the driving force of diffusion in this case is chemical potential gradient. Dealloying is one example of taking advantage of 'up-hill' diffusion. In dealloying, the less noble elements are dissolved in the solution, and the noble metal atoms are driven, opposite of the concentration gradient, to form clusters of noble metal ligaments [60].

2.8 Relaxation behavior of thin films

Relaxation is a process by which a system returns to equilibrium. Relaxation significantly relies on atomic diffusion, and therefore it is also a thermodynamic process. As discussed in previous section, all diffusion-dependent reactions have activation energies, which will be talked shortly later.

Usually people use a Maxwell model to describe the relaxation behavior. In the model, the material is represented by a viscous damper and an elastic spring in series, i.e., the total strain $\varepsilon_{total}=\varepsilon_{damper}+\varepsilon_{spring}$. The derivation of stain to time gives $\dot{\varepsilon}_{total} = \dot{\varepsilon}_{damper} + \dot{\varepsilon}_{spring}$. According to the definition, a damper's behavior can be described as $\dot{\varepsilon}_{damper} = \frac{\sigma}{\eta}$, and a spring behaves following $\dot{\varepsilon}_{spring} = E\dot{\sigma}$, where η, E and σ are viscosity of the damper, elastic modulus of the spring and total stress applied to the series. Thus the total strain rate $\dot{\varepsilon}_{\text{total}}$ is,

$$\frac{d\varepsilon_{total}}{dt} = \frac{\sigma}{\eta} + \frac{1}{E}\frac{d\sigma}{dt} \qquad \text{Equation 2.5}$$

Considering the boundary condition and initial condition in the relaxation, i.e. the strain is constant in relaxation, i.e. $\frac{d\varepsilon_{total}}{dt} = 0$, and at $t=0$, $\sigma(t)=\sigma_0$ (σ_0 is the initial stress in the films), an exponential decay equation can be obtained as the solution of the equation above:

$$\boldsymbol{\sigma(t) = \sigma_0\, exp(-\frac{t}{\tau})} \qquad \text{Equation 2.6}$$

where, τ in the equation is called relaxation time, the reciprocal of it can be interpreted as a qualitative measurement of rate, and is related to the relaxation temperature in Kelvins by an Arrhenius equation as [61],

$$\boldsymbol{\frac{1}{\tau} = C\, exp(-\frac{Q}{RT})} \qquad \text{Equation 2.7}$$

$$\boldsymbol{ln\left(\frac{1}{\tau}\right) = -\frac{Q}{R}\cdot T + C_1} \qquad \text{Equation 2.8}$$

where C is a constant independent of temperature, R is molar gas constant, and Q is the activation energy for the process.

2.9 Size effect of nanoscale mechanical behavior

'Smaller is stronger'.

Size effect on the mechanical behavior of materials has been a hot topic of studies. Due to the extremely small dimensions, nano-scale materials (nano thin film, nanocrystalline materials, nanoporous materials) have displayed some extraordinary behavior, e.g., the especially high strength in nanocrystalline metals [62]. The enhancement of strength in nanocrystalline materials is due to the grain boundary strengthening. Reducing in grain size (micro-nano) causes a large volume fraction of atoms are located in grain boundaries, which impede the dislocation movement. The relationship of the yield strength and the grain size is described by the Hall-Petch equation:

$$\boldsymbol{\sigma_y = \sigma_0 + \frac{k_y}{\sqrt{d}}} \qquad \text{Equation 2.9}$$

where σ_y is the yield strength, σ_0 is a materials constant, which is related to the starting stress for dislocation movement, k_y is the strengthening coefficient, and d is grain size. The equation is named after its inventor E. O. Hall and N. J. Petch (their work were independent).

The size effect can be applied to not only grain size but also other critical size which confines a material, i.e. thickness of thin films, diameter of nano-rods, and ligament size of nanoporous materials. For example, Hodge et al. studied the yield strength of np-Au by nano-indentation and micro-compression, and found that the relationship of ligaments yield strength and ligaments size followed a Hall-Petch type relation [63].

However, controversy arguments exist about the limit of size effect, i.e. can size effect be applied to any small size features without an exception. Some researcher found so called reverse/inverse Hall-Petch effect. The basic idea is decreasing the feature size

beyond 10 nm will weaken a material instead of further increasing its strength. Researchers found the inverse Hall-Petch relation in nanocrystalline metals and nanoporous metals as well [55, 64, 65]. Many mechanisms have been proposed for this effect, e.g., the lack of dislocation source, GB sliding model [64, 66], Coble creep. Some researchers argued it's actually due to the poor quality of the samples, i.e. the increased voids or pores in nanocrystalline metals [67]. No matter this inverse Hall-Petch effect is a fact or not, these arguments can only be solved with further understanding the mechanism of plastic deformation in nanoscale.

3 Experimental

This chapter introduces experimental methods in a more fundamental level since detailed information will be further presented in next a few chapters. In general, experiments in this study includes thin film fabrication techniques, dealloying, characterization, and mechanical behavior test. General information about dealloying has been introduced in previous chapter, and therefore won't be presented here.

3.1 Thin film technique

3.1.1 Sputtering deposition of thin films

As one of the physical vapor deposition (PVD), sputtering deposition is the major technique used to prepare thin film samples in this work. Different from other PVD methods, specifically evaporation, sputtering is more accurate in controlling film stoichiometry, and therefore it was used as the primary tool to prepare alloy thin film samples.

Sputtering is a process generating physical vapor by using ions (mostly Ar^+) to bombard a solid target surface. The process can arise both plasma and ion beams. Plasma is described as weakly ionized gases consisting of a collection of electrons, ions, and neutral atomic and molecular species. Note that plasma is neutral overall.

Sputtering process can be categorized to DC, RF (AC) and magnetron, according to the method to generate plasma or ions. Nowadays, magnetron sputtering is the most widely used one due to a very straight forward reason, i.e., higher deposition rate. Magnetron sputtering is practiced in DC and RF power supplies, but is a significant different category. In the study, a HV (high vacuum) magnetron sputtering system from

AJA Inc. was utilized to deposit films. Both DC and RF power supply was provided by the system to perform sputtering. Another thing noteworthy is even sputtering is a PVD method, it can be operated in the presence of a reactive gas (sometimes called reactive sputtering), e.g., O_2 to produce oxides, N_2 to produce nitrides.

3.1.2 Wafer curvature

The stress of the thin film can be measured by wafer curvature system (Toho, FLX-2320-S). Just as the name implies, wafer curvature system determines thin film stress by measuring curvature of a wafer. The film has to be deposited on a wafer. The curvature difference of the wafer before and after deposition is used to calculate the stress in the film by Stoney equation [58]:

$$\boldsymbol{\sigma_f = \frac{Y_s d_s^2}{6(1-v_s)d_f}\left(\frac{1}{R_2} - \frac{1}{R_1}\right)} \qquad \text{Equation 3.1}$$

where Y_s and v_s are Young's modulus and Poisson's ratio of the substrate, d_s and d_f are the thickness of the substrate and the film, as shown in Figure 3.1. R_1 and R_2 are the radii of the wafer before and after deposition of the film.

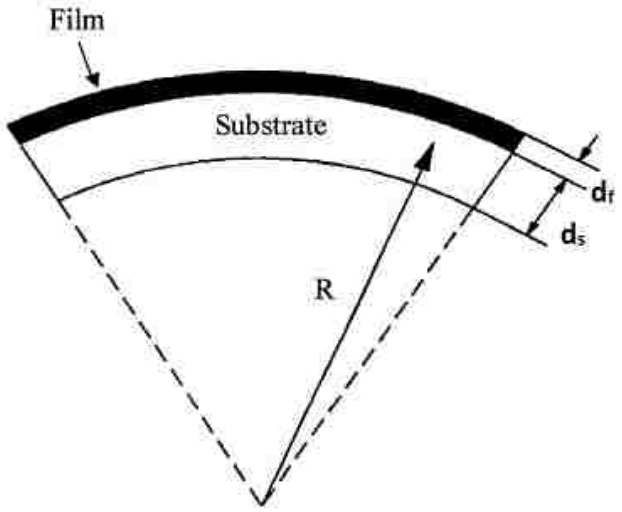

Figure 3.1. A schematic drawing of the curvature of wafer with a negative radius (corresponding to a compressive stress in film).

Stoney equation is widely applied in determining the stress of thin films. In most of the cases, the properties of the substrate, i.e. Y_s, v_s, *and* d_s are known or easy to obtain. For a thin film with known thickness, d_f, the curvature, $1/R_1$ and $1/R_2$ can be measured by wafer curvature. Therefore, the film stress is obtained according to Equation 3.1. It's noteworthy that the Stoney equation only applies to thin films which have thickness way smaller than that of the substrates, i.e., $d_f << d_s$.

When measuring film stress, wafer (3 inch wafers were used in the study) curvature is obtained with a 15° or 45° interval, and 12 (0°-165°) or 4 (0°-135°) measurements have to make to determine a stress mapping over the entire wafer or an average film stress. The Toho wafer curvature system allows heating or cooling sample in a temperature range from -75℃ to 500℃ while simultaneously measuring film stress. Therefore, wafer curvature was used for thermal cycling or thermal relaxation of thin film samples, to evaluate themomechanical behavior of thin films.

3.2 Characterization

3.2.1 Profilometer

The film thickness is measured by a stylus profilometer (Dektak, Bruker). Different from optical measuring of film thickness, profilometer is destructive. It works by scanning a needle over a film-substrate step, the film thickness is directly read out as the height of the step. The step can be created by masking or etching during or after deposition. The system resolution is a few angstroms (~ 5Å), but in practice the measurement of films with thickness under 50 nm is not precise, due to substrate roughness or vibration of the equipment.

3.2.2 SEM

Scanning electron microscopy (SEM) is the most widely employed tool to perform characterization for thin films. It utilizes an electron probe scanning over the sample to produce various signals, including secondary electrons (SE), backscattering electrons (BSE), Auger electrons, X-rays and so on. These signals are collected by different detectors to perform structure and analytical measurement. The SEM used in this study included a Hitachi S900 FEG (cold cathode filed emission gun) SEM and a Hitachi S3200 (tungsten hairpin filament).

SEM is primarily worked in SE mode to resolve surface morphology of specimens. The resolution of each SEM differs from 1 nm to a couple nanometers. S900 has the highest one, 1 nm, among all the SEMs. Additionally, energy dispersive X-ray spectroscopy (EDS) was performed in S3200, which is attached with an Evex detector, to measure the chemical composition of thin films.

The requirements for traditional SEM samples are conductive and dry. Samples have to be mounted on sample holder through a conductive path, such as carbon tape or carbon paint. If sample itself is not conductive, a layer, e.g., Au or carbon coating, is coated on sample surface to create a conductive surface. Dryness may not be a necessity for SEM samples anymore, due to the emergence of environmental SEM, by which wet samples, e.g., biological specimen, can be observed in relative low vacuum.

3.2.3 XRD

X-ray diffractometer (XRD) was used in the study to determining the crystallographic structure of a sample. It utilizes a beam of X-ray (Cu Kα usually) to generate diffraction in specific directions. By measuring the angle of deflected beams, the lattice parameter and crystal structure can be obtained by the well-known Bragg's law:

$$2d \sin\theta = n\lambda \qquad \text{Equation 3.2}$$

where θ is the incident beam angle, λ is the wavelength of incident beam, n is any integer, and d is the spacing between diffraction planes.

X-ray can penetrate into a few to a couple hundred micrometers depending on incident beam and medium. Thin film sample may not be suitable for this technique, due to a huge amount of signal from substrate. However, useful spectra can be obtained by optimizing scanning parameters, such as scan speed, steps, and beam slot size.

3.2.4 TEM

Transmission electron microscopy (TEM) works with electron beam transmitted through a thin enough sample. Since it also utilizes electron beam, TEM also generates secondary electrons, backscattering electrons, auger electrons, X-rays, but particularly and

most importantly transmission electrons. TEM can work in imaging mode, and also analytical mode by electron diffraction, EDS, electron energy loss spectrum (EELS).

The major advantage of TEM over SEM is the higher resolution, which is one order higher than SEM. Specially, scanning transmission electron microscopy (STEM), working by focusing the electron beam into a very small spot size, down to 1Å, can achieve resolution in sub nanometer lever. This feature benefits a lot of techniques, such as annual dark field imaging (ADF), EDS, and EELS. Note that EDS (and EELS) in SEM can never achieve an analytical resolution of several nanometer, which is due to the pear-shape (tapping toward the top) interaction volume. Even the probe size can be down to a few nanometer, the interaction volume has diameter up to tens or even hundreds nanometers.

With these advantage, TEM would be employed more widely than SEM. However, a major disadvantage of TEM is sample preparation. TEM sample has to be prepared thin enough to make it electron transmittable. One may think thin film is therefore ideal for this technique, but removing films from their substrates is even more troublesome. One method to prepare a thin film sample will be presented later in chapter 6.

3.2.5 XPS

X-ray photoelectron spectroscopy (XPS) is a spectroscopic technique to perform chemical analysis, by utilizing X-rays as incident beam to generate photoelectrons. Similar to X-rays, photoelectrons are also characteristic. XPS spectra provide information of element composition, and also chemical state and electronic state. Therefore, XPS is usually used as an assistant tool to EDS. Another unique feature of XPS is surface sensitivity. It measures photoelectrons escaped from the top several nanometers (1-10 nm) of the sample.

3.3 Mechanical test of nanoporous metals

Mechanical test of nanoporous metals were studied by thermal cycling for films, and nanoindentation for bulk samples.

3.3.1 Thermal cycling

Thermal cycling was performed in the wafer curvature system, as talked in section 3.1.2. When a thin film subjected to heating or cooling, thermal expansion or contraction is induced in the film, and so is the substrate. Due to the disparity in thermal coefficients, film and substrate are subjected to different degree of expansion or contraction. Assuming substrate is more thermally rigid ($\alpha_s<\alpha_f$), and then film stress would decrease as temperature going up (due to a negative $\Delta\sigma_f(T)/\Delta T$ according to Equation 3.3), and vice versa. A cooling curve of metal thin film is very similar to a stress-strain curve. As temperature decreasing, the film undergoes thermoelasticity and thermoplasticity. The thermoelastic slope is related to the film's biaxial modulus, M_f, by the following equation, Equation 3.3 [58]. According to it, the biaxial modulus of the thin film can be determined.

$$\frac{\Delta\sigma_f(T)}{\Delta T} = (\alpha_s - \alpha_f) \cdot M_f \qquad \text{Equation 3.3}$$

where α_s and α_f are thermal expansion coefficients for substrate and film respectively. $\Delta\sigma_f(T)/\Delta T$ is the slope of the thermal elastic curve.

Another mechanical property can be determined from thermal cycling is yield strength, σ_y. As in classic stress-strain curve, yield point is measured as the transition point from thermoelasticity to thermoplasticity. However, if the temperature applied on the film is not beyond the thermal elasticity range, transition point won't display in the thermal cycling curve.

3.3.2 Nanoindentation

Nanoindentation is a technique applying indentation hardness measurement to small volume. Due to the especially small indenter tip, and small load applied, the indenter print size may be a few micrometers or even nanometers. Nanoindentation on thin film must be carefully designed, due to influence of the substrate. As a rule of thumb, when the depth of the indentation exceeds 10-25% of the film thickness, substrate effects must be considered.

A typical indentation curve is displayed in Figure 3.2, from which the hardness, *H*, can be determined. It is defined as the maximum load, P_{max}, divided by the residual indentation area, A_r, as in Equation 3.4. Note that A_r is the print area after indenter being removed from sample.

$$H = \frac{P_{max}}{A_r} \qquad \text{Equation 3.4}$$

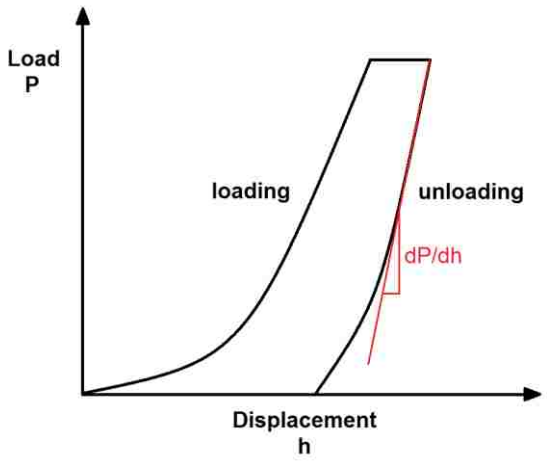

Figure 3.2. A typical loading and unloading curve in indentation. Reduced younth modulus can be calculated by the linear unloading slope, i.e. *dP/dh*.

In addition to hardness, the linear part of the unloading curve can be used to calculate Young's modulus, *E*. Note that the slope, *dP/dh*, is not Young's modulus itself,

instead is reduced Young's modulus, E_r, but it is related with Young's modulus by a relationship.

In this study, a nanoindenter (NanoTest Vantage, Micro Materials) was used to measure the hardness of nanoporous films. It utilizes a Berkovich diamond indenter (3-sided pyramid shape). The load range of the system is from 0.1 mN to 500 mN.

4 Thin film np-Ni fabrication and thermomechanical behavior study

4.1 Introduction

This project is sponsored by KSEF (Kentucky Science and Engineering Foundation). One objective is to fabricate np-Ni as an alternative to Raney nickel (RN). RN is a commercial catalyst in oil hydrogenation. It's made by leaching Al or Si from NiAl or NiSi precursor alloy in a hot alkali solution (KOH). Raney nickel exists in fine powder form and exhibits ligament diameter as small as 5 nm [68]. In the process there are significant amount of hydrogen adsorbed within the pores. Additionally due to its activated form, RN is highly pyrophoric and must be protected from air exposure. For example, it's prepared in a water-based slurry to prevent ignition of the hydrogen gas contained in porous structure. Another method is removing the hydrogen in RN by mild heating in an air/oxygen mixture or a diluted H_2O_2 solution [69]. This step also produces a thin oxide layer in RN, which enhances its hydrogen adsorption ability and improves its catalytic ability. However, these series of processing can be cumbersome for industrial production. One objective of this project is to fabricate nanoporous nickel (np-Ni) in stable form with a relatively easy approach.

Electrochemical dealloying can prevent the pyrophoric problem by separating the cathode and anode reaction, producing H_2 at the cathode and dealloying Ni at the anode. Therefore H_2 gas won't be trapped in porous structure. Searson's group [70] has produced np-Ni from Ni-Cu by electrochemical dealloying, and the ligaments in the np-Ni are 100-200 nm, one order larger than that of Raney Ni (5-10 nm). Hakamada and Mabuchi also produced np-Ni (and np-NiCu) from NiMn with electrolytic dealloying, and the dealloyed materials have ligaments of 10-15 nm [38]. However, applying voltage made these

methods costly and troublesome. In this study, thin film np-Ni was produced by free corrosion. Multiple precursor alloys, i.e. NiCu, NiAl, NiFe and NiMg were selected to fabricate np-Ni.

In addition to fabrication of thin film np-Ni as an alternative of RN, another goal of this project is to study the mechanical behavior of np-Ni. As mentioned in chapter 1, most current studies have focused on np-Au, due to the noble chemical behavior of Au and ease of fabrication of np-Au. Different from Au, Ni is a non-noble metal, and has a relatively high yield strength, which means Ni is 'tougher' than Au under stress. Meanwhile Nickel is prone to be oxidized. Even the nature oxide layer on Ni surface is only 1 nm [71], but considering the nanometer-length-ligaments and the high surface area in np-Ni, the mechanical behavior would be strongly affected by the oxide layer on surface Ni.

4.2 Challenges and methodology

Challenges in this work are generally listed in the following:

1. Different from typical np-metals, Ni is relatively active compared with Au. Sacrificial elements in the precursor system and the dealloying solution must be carefully selected. The sacrificial element in precursor alloy must provide sufficient potential difference to make it be dissolved but reserve Ni.
2. The commercial Raney nickel is made by leaching Al from Ni-Al alloy. To be an alternative of Raney nickel, the proposed dealloying method has to be simple as well. And the new method should be able to avoid the pyrophoric problem in np-Ni.

3. The dealloyed np-Ni should possess a comparable fine structure to Raney nickel (less than 10 nm pore size).
4. Due to its ferromagnetic nature, characterization of Ni in electron microscope may be troublesome.
5. Due to its active nature, heating of Ni would cause oxide layer on sample surface. Therefore, heat treatment must be performed in reduced gas atmosphere, such as forming gas (mixture of N_2 and H_2 gas).

With the accessible equipment and previous experience in studying np-Au, free corrosion were utilized to synthesize np-Ni. Compared with other fabrication methods, free corrosion is straight forward and inexpensive, which is more favored by industry. Multiple precursor alloys were selected, including Ni-Cu, Ni-Al, Ni-Fe and Ni-Mg. These alloy systems displayed big diversity in terms of phase. Ni-Cu was selected because they formed a miscible solid solution over the entire range of composition in phase diagram. Therefore, it provides a one-phase precursor system, which matches the requirement of precursor alloy (see more discussions about it in Chapter 2 section 2.2). But one problem with Ni-Cu was that Cu is actually more noble than Ni. Therefore Ni is more vulnerable than Cu in most of the etchant (acid). A special commercial copper etchant was used in dealloying Ni-Cu with the purpose to reserve Ni while etching Cu. In other alloy systems, the sacrificial elements, i.e., Al in Ni-Al, Fe in Ni-Fe, and Mg in Ni-Mg, were selected because they are less noble than Ni and part away from Ni in electrode potential.

To address the pyrophoric problem, etchant for each alloy was selected to minimize the production of hydrogen gas in dealloying. In dealloying of NiAl, a mixture

of NH_4OH and H_2O_2 was used to etch Al. The existence of H_2O_2 acted as a strong oxider to avoid generating H_2.

The np-Ni was characterized by X-ray diffraction (XRD), scanning electron microscope (SEM), energy dispersive X-ray spectroscopy (EDX) and X-ray photoelectron spectroscopy (XPS). As talked in previous section, due to it ferromagnetic nature, np-Ni sample did cause difficulty in taking SEM micrographs. However, by proper preparation and optimizing the working condition, high magnification images were taken for both plan-view surfaces and cross-sections. XPS was used in analyzing surface chemical information of np-Ni.

The mechanical properties of np-Ni thin films were studied by thermal cycling and relaxation in wafer curvature system. To prevent Ni being oxidized in heating, the experiments were performed in forming gas (4 vol.% H_2) atmosphere.

Detailed information about experiments and results are presented in the following sections.

4.3 Experimental details

4.3.1 HV magnetron sputtering

Three-inch diameter (100)-oriented silicon wafers (coated with 50 nm amorphous Si_xN_y, CrysTec GmbH, Germany), with thickness of 180 μm or 380 μm, were used as substrates for deposition of the precursor alloy films. Magnetron sputtering was performed with an AJA ORION high vacuum deposition system (base pressure of 1.3-6.5 $\times 10^{-6}$ Pa, or 1.0-5.0 $\times 10^{-8}$ torr), using high-purity Ni (99.99%) and Cu (99.999%) or Al (99.999%) or Fe (99.95%) or Mg (99.95%) targets for source materials. Thin films were co-deposited

or sequentially deposited (as multilayers) by flowing Ar gas at 2.5 mtorr, with total thicknesses of 100-500 nm.

For the multilayer films, layer thicknesses of 1.5-2 nm and 5.5-6 nm were chosen for Ni and Al layers, respectively. These values of thickness were selected, and therefore each nickel layer is thick enough to distribute over the entire substrate/film surface. If the nickel layer was too thin, it would form islands on the surface, instead of a continuous layer. Meanwhile, layer of each sacrificial element (e.g. Al) had to be sufficiently thin to avoid delamination.

To enhance the adhesion of the films on the substrate, a 10 nm Ta layer and a 10 nm Ni layer were deposited sequentially as interlayers for co-deposited films. Only a 10 nm Ta was used as interlayer for multilayer films. To rule out contribution of the interlayer in film stress measurement, interlayers were deposited on both side of the Si wafer, and therefore the stress induced by interlayer was cancelled out.

The precursor alloy composition is critical to morphologies of dealloyed films. In order to determine the optimal composition, a composition gradient sample was prepared by fixing the substrate during deposition, as shown in Figure 4.1. In this configuration, the deposited film is Ni-rich on left side and sacrificial elements-rich on right side. The compositional gradient sample was then cut into small pieces with each piece having different composition, and then was dealloyed in desired solution.

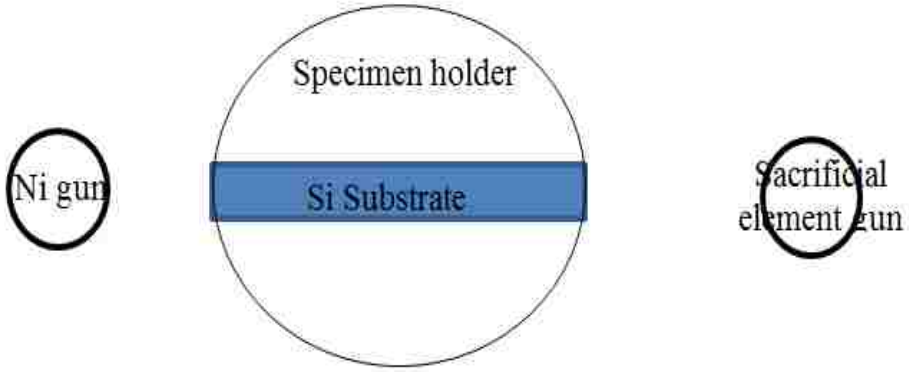

Figure 4.1. A schematic illustration of the deposition of a composition gradient precursor sample. Ni and sacrificial element were deposited at the same time. With this configuration, the film was Ni-rich on the left, and sacrificial element was rich on the right.

4.3.2 Dealloying

Dealloying was performed by using free corrosion. A commercial copper etchant (#49-1, from Transene Co.) was used as the etchant for NiCu with the purpose to dissolve Cu but reserve Ni. For NiAl precursor films, a mixture of $1NH_4OH(30\%)$: $1H_2O_2(30\%)$ was chosen. The strong oxidizer H_2O_2 in the solution was there to avoid generation of hydrogen gas, and thus prevents np-Ni from sharing Raney Ni's problem of pyrophoric. For NiFe and NiMg precursor films, phosphoric acid and diluted acetic acid, respectively, were used as dealloying etchants. Morphology of the dealloyed films is strongly affected by dealloying conditions, e.g. concentration of the solution, dealloying temperature and time, agitation of etchant, etc. [72] Various conditions were tested, and the optimal dealloying conditions were determined after evaluation of the np-Ni surface morphology and purity.

The as-dealloyed films usually lost the metallic luster with a dark color. They were cleaned with ethanol and then ultra-pure water. To protect them from being oxidized

or contaminated, sometimes the dealloyed films were stored in ethanol until further experiments were performed.

4.3.3 Characterization

4.3.3.1 XRD

X-ray diffraction (XRD) patterns were collected by Siemens D500 X-ray diffractometer and Bruker-AXS D8 Discover diffractometer. Both diffractometers used Cu targets. Measurements were made to determine the preferred orientation (texture) in precursor films and also np-Ni films.

XRD scan can be used to track dealloying as well. By tracking the sacrificial element or the precursor alloy peak at continuous dealloying step, the peak intensity can tell if dealloying finished or not. However, this method is reliable only if the same sample was used in the whole process. And since the position of sample in the XRD can affect the peak intensity as well, it has to be careful in mounting the sample to make sure it's the same area that exposed to X-ray in each scan.

4.3.3.2 SEM

In order to observe the nanoporous structure of the dealloyed films, a microscope with high resolution was needed. The Hitachi S900 scanning electron microscope (SEM), with a maximum resolution of 1.0 nm, was the primary tool used to obtain SEM micrographs.

The SEM samples are prepared by mounting a small piece of sample on a Cu holder with carbon or silver paint. Due to the dimension of sample holder, samples with limited size, i.e. maximum 7 mm in length, 4 mm in width, and 2 mm in height, can be

positioned on the holder. In order to obtain cross-section images of thin films, a special hold was made by cutting a groove on the holder along the long edge. When preparing a sample for cross-section imaging, the sample was cut into a piece with narrow width, and mounted by standing in the groove, perpendicular to the holder, to make cross-section of the film faced electron beams when putting the sample in SEM.

The S900 was operated at 3kV or 6kV to obtain secondary electron images. And 6kV is recommended for np-metal thin films with ligament less than 10 nm.

4.3.3.3 EDS

The Hitachi S3200 SEM was used to perform EDS analysis, for determination of thin film composition. S3200 has a tungsten hairpin filament, and can be operated from 3kV to 30kV. 20kV was used for most of the samples in the measurement.

The S3200 has an Evex EDS detector with a chemical resolution of approximate 1 at.%. The reliability of results was improved by taking the average of at least 3 measurement from different locations of one sample. Note that the working voltage used in the measurement allowed the electron beam penetrate into several to tens of micrometer depth of the sample. As a result, the interlayers, including Ni and Ta, was also included in the measurement. Therefore, the measurement from EDS results had been corrected by subtracting Ni content in the interlayer.

S3200 has a larger sample stage than S900, especially in thickness dimension. Its sample holder, i.e. Al stub (15 mm or 30 mm diameter, Ted Pella), is different from that of S900 either. Thin films on Si substrate were cut into proper size, and then mounted on the sample holders.

4.3.3.4 XPS

A Kratos XSAM-800 x-ray photoelectron spectroscopy (XPS) was used as an additional tool for further chemical analysis of dealloyed films. Specifically, since Nickel is oxidized once exposure to air, XPS was used to determine the oxide layer. The measurement was operated at 14kV, with Al Kα X-rays as incident beam. The sample mounting is similar to that of S3200.

4.3.4 Film thickness measurement

As talked in previous chapter, precursor film thickness measurement was performed in a stylus profilometer. To create a sharp step from films to substrates, a straight line was drawn with a Sharpie marker on the substrate before film deposition. After deposition finished, the sample was soaked in acetone for a few hours until the sharpie line was dissolved, and the film above sharpie paste was peeled off. The thickness of the film was measured across the drawing line. An average thickness was determined after 10 or more measurements were obtained. To have an accurate measurement, the film should have a thickness of at least 50nm, and thicker is better.

4.3.5 Cyclic Voltammetry

Electrochemical measurement was performed by cyclic voltammetry (CV) scans with a potentiostat (eDAQ). The set-up was a standard three-electrode glass cell in a 1M *KOH* solution, using a Ag/AgCl electrode as reference electrode and a Pt wire as counter electrode. In the experiments, CV scans were performed over the potential range of 0-0.6V with scan rates of 5 mV/s, 10 mV/s, and 20 mV/s.

4.3.6 Stress evolution during dealloying

Film stress was measured by a wafer curvature (Toho FLX-2320-S) as discussed in Chapter 3, Section 3.1.2. The curvature of a bare Si wafer was measured by the system before a film was deposited on it. After deposition, the curvature was re-measured. The system calculated the curvature of the original bare Si wafer was subtracted to calculate the net curvature due to stress in film. Film stress was eventually determined by using the Stoney equation [58]. Detailed description of film stress measurement is in Section 2.5.

It is worth noting that the interlayers introduced additional stresses and can therefore influence the overall stress measurement. To account for the stress due to interlayers, the same interlayers were deposited on both the front and the back side of the Si wafer, before final deposition of the precursor film. Therefore, the stresses caused by the interlayers were present on both sides of the substrate and cancelled each other.

Stress evolution during dealloying was measured by forcing the dealloying process stop at regular time intervals. At each time interval, the sample was removed from the etching solution, and cleaned with distilled water and ethanol. The stress in the film is then measured by wafer curvature. Based on previous experience, it was known that stress would change most dramatically at the beginning of dealloying, and thus a short time intervals were chosen at the beginning and increased gradually with dealloying going.

4.3.7 Thermal cycling and relaxation of thin films

Thermal cycling was also performed in the wafer curvature system (Toho FLX-2320-S). The dealloyed films were heated and cooled in a forming gas (4 vol.% H_2) atmosphere in order to avoid oxidation of the np-Ni films. The temperature ranged from

40 ℃ to 250 ℃, with heating and cooling rate of 5 ℃/min. The stress in the films was measured simultaneously and recorded per one minute.

Stress relaxation was performed in between a heating and cooling cycle. The sample was first heated to 250 ℃, and during the cooling segment, it was interrupted by remaining the temperature at certain value for a desired time (8 h - 20 h). The stress was recorded at 5 ℃ interval during relaxation in these experiments.

4.4 Results and discussion

4.4.1 Optimized dealloying conditions

The optimal dealloying conditions from multiple precursors are listed in Table 4.1. The composition of the dealloyed films was determined by EDS measurements. Additional XPS scans were recorded for co-deposited NiAl films because the dealloyed films exhibited an abnormal microstructure which was suspected to be nickel oxidation (as shown in next section of this chapter).

The major problem of dealloying NiCu, NiAl and NiFe films was that dealloyed film retained a significant amount of the respective sacrificial elements. Indeed, the NiCu precursor did not even result in Ni-rich np-Ni. However, NiMg films yield np-Ni with 100% Ni after reasonably short dealloying times. Dealloyed multilayer NiAl films also resulted in a high Ni content, but Ni and Al elements were not evenly distributed throughout the film. To improve the uniformity of multilayer NiAl samples, they were annealed in 200 ℃. The annealed samples were then dealloyed and examined with X-Ray diffractometer (XRD) and EDS. However, the uniformity didn’t get improved.

Table 4.1. List of the optimal fabrication and dealloying conditions for synthesizing np-Ni from co-deposited NiCu, co-deposited NiAl, multilayer NiAl, co-deposited NiFe and co-deposited NiMg thin films.

Film deposition mode	Precursor composition (at.%)	Dealloyed film composition (at.%)	Etchant	Dealloying condition	Dealloying time
Co-deposition	$Ni_{33}Cu_{67}$	$Ni_{37}Cu_{63}$	Transene Cu Etchant 42-1 (diluted 1:1 with H_2O)	40˚C	6 hours
Co-deposition	$Ni_{25\text{-}35}Al_{65\text{-}75}$	$NiO_{45}Al_{55}$	1 NH_4OH (30%) : 1 H_2O_2 (30%) mixture (diluted 1:9 with H_2O)	Room temp (RT)	30 min
Multilayer	$Ni_{23\text{-}28}Al_{72\text{-}77}$	$Ni_{67}Al_{33}$ (avg.); Ni content varied from 30 at% to 100 at%	1 NH_4OH (30%) : 1 H_2O_2 (30%) mixture (diluted 1:9 with H_2O)	RT	22 min
Co-deposition	$Ni_{30}Fe_{70}$	$Ni_{60}Fe_{40}$	H_3PO_4 (85%) acid	RT with vibration	8 min
Co-deposition	$Ni_{33}Mg_{67}$	100% Ni	HAc(100%) acid (diluted 1:79 with H_2O)	RT	10 min

4.4.2 Surface morphology of dealloyed films

The SEM micrographs in Figure 4.2 display surface morphologies of as-dealloyed NiCu films. Image (a) and (b) represent films dealloyed in non-diluted and diluted etchants (1:1), respectively. Based on the ligament and pore size measurements, the film dealloyed in diluted Cu etchant exhibited a finer structure, with ligament width and pore size of ~8 nm, which is ~1 nm smaller (on average) than that dealloyed in non-diluted etchant. Although the dilute etchant needed a longer dealloying time, this route was successful in refining the nanoporous structure. Beside etchant concentration, the porous size can also be adjusted by changing dealloying time, temperature, utilizing agitation of the etchant. For example, extended dealloying times could result in significant ligament coarsening. As

seen in Figure 4.2c and d, the film in 4.2d was dealloyed in the same etchant, but with longer dealloying time. The ligament width in this film is around twice of the ones in 4.2b or 4.2c.

Surface morphology of dealloyed co-deposited and multilayer NiAl precursor films were displayed in Figure 4.3. Image (a) was obtained from np-Ni by dealloying a co-deposited NiAl film. It reveals a honeycomb-like structure, which is similar to that of porous alumina by anodizing aluminum membrane (it actually has more ordered pores than dealloyed NiAl films). The ligaments had an average width of ~4 nm and an average aspect ratio of 2.3, which is the finest structure obtained from any of the precursor films. The structure of np-Ni generated by dealloying multilayer NiAl is completely different, as shown in Figure 4.3b. This np structure contained shorter and more randomly oriented ligaments, and was comparable to the typical structure of np-Au. It exhibits ligaments of ~5 nm and an aspect ratio of 1.5.

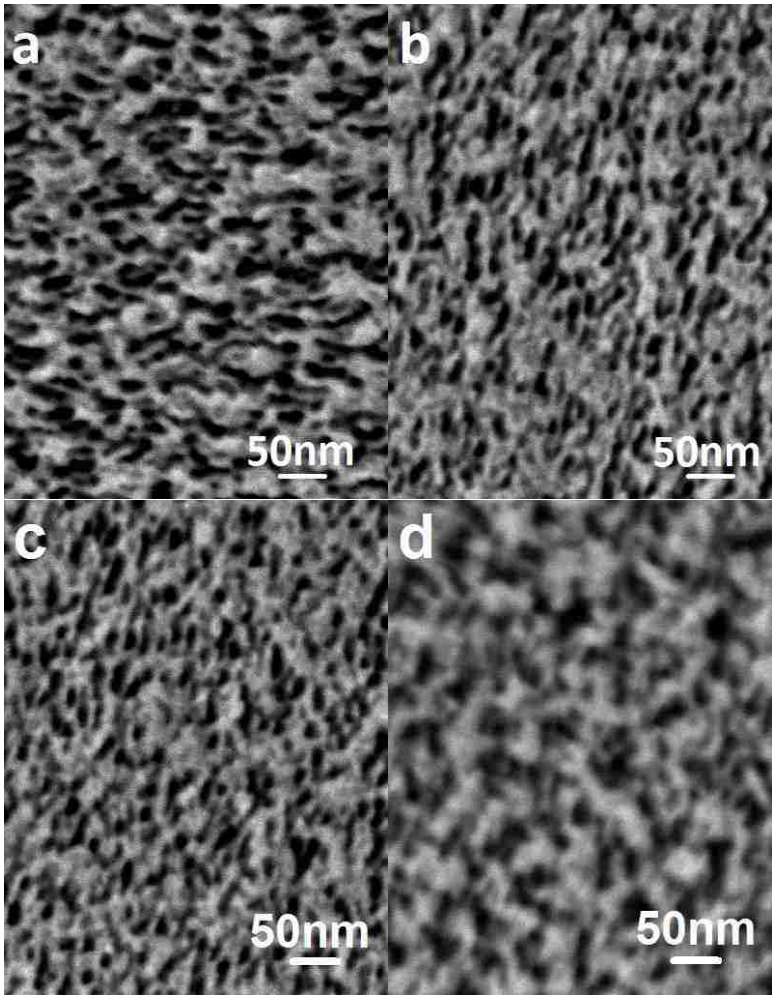

Figure 4.2. (a) Surface morphology of dealloyed 100 nm $Ni_{33}Cu_{67}$ film. The film was dealloyed by Cu etchant (Transene 42-1). Both the pore and ligament sizes were 9 ± 3 nm. (b) A same precursor film was dealloyed using 1:1 diluted Cu etchant. The pore and ligament sizes were 8 ± 2 and 8 ± 3 nm, respectively. (c) A same film as the one in image (b). (d) A same precursor film was dealloyed also in 1:1 diluted etchant, but experienced longer dealloying time (9 hours for this sample, but the samples in (b) and (c) were dealloyed for 6 hours. The ligaments were significantly coarsened with longer dealloying time.

To further characterize the np-Ni created by dealloying of co-deposited NiAl, the dealloyed film was examined by XPS. This analysis indicated that the ligaments has been oxidized, with a composition of 45 at.% NiO and 55 at.% Al. This may explain why the dealloyed co-deposited NiAl films have a similar structure as AAO membrane. Note that even the ligament geometry is mainly evaluated by aspect ratios here, the curvature of ligaments might better represent nanoporous structure and ligament geometry.

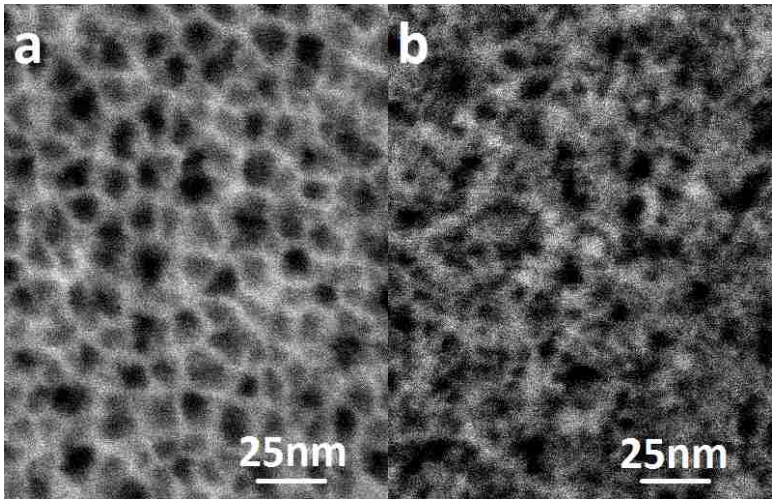

Figure 4.3. (a) Surface morphology of the dealloyed 100 nm co-deposited $Ni_{33}Al_{67}$ film. Resultant nanoporous material is NiO, not metallic Ni. The ligaments were 4 ± 1 nm wide, with an aspect ratio of 2.3. (b) Surface morphology of the as-dealloyed 100 nm multilayer $Ni_{28}Al_{72}$ film. The ligaments were 5 ± 1 nm, with an aspect ratio of 1.5.

The plan-view SEM images of dealloyed NiFe films are shown in Figure 4.4. Figure 4.4a displays surface morphology of np-Ni without agitation of the etchant. The nanoporous structure exhibited an average ligament width of 32 ± 4 nm. Figure 4.4b shows the surface micrograph obtained by dealloying the same NiFe film in the same etchant for the same time, but with agitation during etching. This resulted in much finer nanoporous structure with ligament width of 12 ± 3 nm. These indicated agitation during dealloying can refine the ligaments by more than a factor of two. Additionally, np-Ni alloy created in the agitated etchant had a higher Ni content (60 at.% Ni) than in the non-agitated etchant (36 at.% Ni). Since dealloying involves competing and simultaneous processes of sacrificial element dissolution and remaining element surface diffusion, a flowing etchant could shift the balance of these processes and, e.g., increase the rate of Fe removal, thereby increasing the relative number of Ni atoms at the dealloyed surface. This could increase the nucleation rate of ligaments and decrease their final spacing in the np structure.

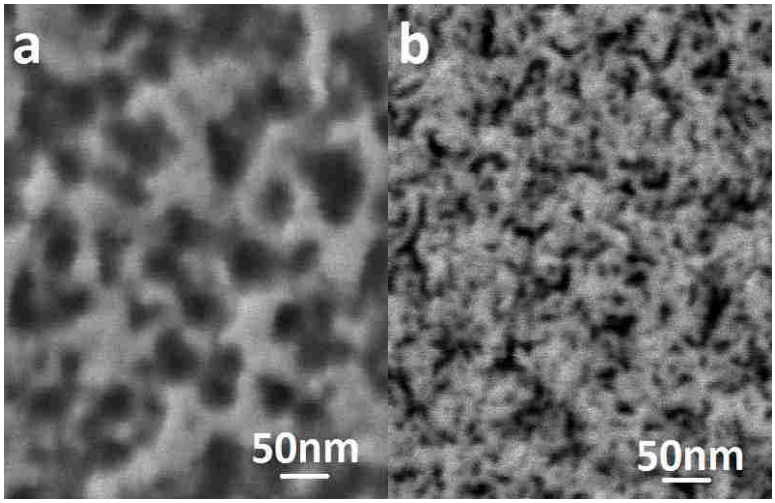

Figure 4.4. (a) Morphology of as-dealloyed 100 nm $Ni_{30}Fe_{70}$ film. The film was dealloyed in 85% H_3PO_4 for 8 min without sample vibration. The average ligament width was 32 ±4 nm. (b) Nanostructure of as-dealloyed 100 nm $Ni_{30}Fe_{70}$ film. This film was dealloyed in 85% H_3PO_4, with sample vibration, for the same time. The resulting ligament width was 12 ±3 nm.

Figure 4.5a displays SEM images of np-Ni created by dealloying a 100 nm NiMg film. The average ligament size was determined to be 7 nm, representing one of the finest structures among all the dealloyed films. Cross-section image in Figure 4.5b, was taken from np-Ni film of an original thickness of 500 nm. The film experienced a huge volume contraction due to dealloying. The dealloyed film had a thickness of only ~160 nm, about 1/3 of the original thickness. The huge volume contraction resulted in np-Ni films with high relative densities. In the case of the 500 nm NiMg film, it has a 33 at% Ni and 67 at% Mg in the precursor alloy, corresponding to ~19 vol.% Ni and 81 vol.% Mg. If there was no contraction during dealloying, the dealloyed film should have a relative density of 0.19, i.e. the volume fraction of Ni in the precursor alloy. However, due to the contraction, the relative density became 0.59. It's very high compared with other nanoporous metals.

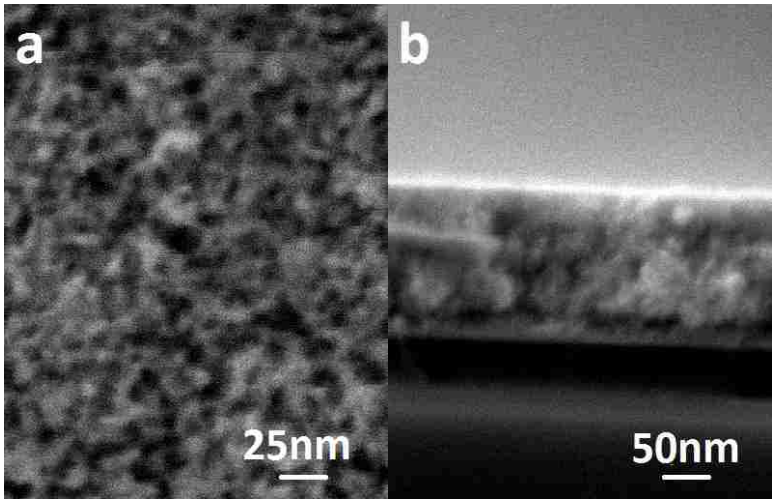

Figure 4.5. (a) Morphology of an as-dealloyed 100 nm $Ni_{33}Mg_{67}$ film, with a ligament size of 7±2 nm. (b) Cross-sectional SEM image of an as-dealloyed 500 nm $Ni_{33}Mg_{67}$ film.

Note that all precursor alloy systems yielded nanoporous structure without cracking, with the optimal dealloying condition. Even there was a significant amount of volume contraction during dealloying, dealloyed NiMg didn't display cracks either.

Considering the morphologies of dealloyed np-Ni films as well as the purity of Ni content after dealloying, the NiMg precursor system is a promising candidate for fabricating np-Ni. The final nanoporous material consistently exhibited high purity (100% Ni, with no residual Mg detected by EDS) and fine porosity (ligament size of 7 nm). This form of np-Ni was chosen for further study of mechanical behavior during the rest of the project.

4.4.3 XRD scan

As discussed previously, XRD scan of the thin film deliver important information about crystal orientation or texture. The NiCu phase diagram displayed a complete solid solution over the entire composition range. Indeed, there was only one peak appearing in XRD scan of NiCu precursor film, except the Si peaks. This single peak was indexed to be

NiCu (111). The position of the alloy (111) peak laid between Ni (111) and Cu (111) or Fe (111). The peak position can be used to calculate the alloy composition. Here an example is presented to describe this method.

For example, a NiCu film has a <111> peak at 43.7 °. The incident beam Cu Kα has a wavelength, λ, of 1.54 Å. With Bragg law, the corresponding plane spacing at 2θ angle of 43.7 °is calculated as, $d_{NiCu} = \frac{\lambda}{2sin\theta} = \frac{1.54\dot{A}}{2\cdot\sin(\frac{43.7^\circ}{2})} = 2.068\ \dot{A}$.

On the other hand, the (111) plane spacing of pure Ni and pure Cu are,

$$d_{Cu} = \frac{a_{Cu}}{\sqrt{l^2 + k^2 + h^2}} = \frac{3.6148\dot{A}}{\sqrt{3}} = 2.087\ \dot{A}$$

$$d_{Ni} = \frac{a_{Ni}}{\sqrt{l^2 + k^2 + h^2}} = \frac{3.5239\dot{A}}{\sqrt{3}} = 2.0345\ \dot{A}$$

where a_{Cu}, and a_{Ni} are lattice parameters of Cu and Ni respectively, i.e. 3.6148$\dot{A}$, and 3.5239 $\dot{A}$ [73]; l, k, h are miller index of the planes, i.e. 1, 1, 1.

Considering the nature of solid solution, the *d* spacing of NiCu alloy relates to the d spacing of pure Ni and Cu by the composition of the alloy. Assume the Ni content of the sample is *x* in at.% (then the Cu content is 1-*x*), the relationship of d_{NiCu} and d_{Ni}, d_{Cu} can be written by a scaling equation (sometime also called lever rule), as shown in Equation 4.1.

$$d_{NiCu} = d_{Ni} \cdot x + d_{Cu} \cdot (1 - x) \qquad \text{Equation 4.1}$$

d_{NiCu} and d_{Ni}, d_{Cu} are calculated as 2.068 Å, 2.0345 Å, and 2.087 Å, respectively. With Equation 4.1, the Ni content of the film is calculated as,

$$x = \frac{d_{NiCu} - d_{Cu}}{d_{Ni} - d_{Cu}} = \frac{2.068\dot{A} - 2.087\dot{A}}{2.0345\dot{A} - 2.087\dot{A}} = 0.362 = 36.2\%$$

This method can be used to verify the measurement from EDS. However, it's worth noting that the calculation by this method is strongly affected by the accuracy of

peak position. An error in percentile may cause a couple percentage differences for the composition.

It's more complex for NiFe, NiAl and NiMg films. Intermetallic compounds or intermediate phases displays in their phase diagrams. The optimal composition used for each precursor alloy lies in between two phases or right on an intermetallic line (Ni_1Mg_2 used in NiMg precursor). The XRD scans of these films were not conclusive. Incidentally, NiFe and NiAl scans displayed only one peak at around 44-45 °(higher 44 °for NiFe, lower 44 °NiAl), which is very close to Ni (111) peak (44.5 °). If interpreting this peak as Ni (111), there should be another peak indicating one phase which containing the sacrificial elements, i.e., Fe and Al. But it's not the case. Therefore, this interpretation is not convincing. The scans in NiMg film didn't be able to obtain any peak except peaks from Si substrate. It is suspected to be an amorphous structure. Note that to evaluate the XRD scans of a thin sample, a control scan from the same Si substrate must be obtained to rule out the diffraction peaks from those of the substrate.

No matter what kind of crystallographic structure the precursor alloys have, they all yielded nanoporous structures, as shown in previous section. Therefore, it is not necessary true that only one phase precursor alloy can yield nanoporous structure. Indeed, other groups had also synthesized np metals from various precursor alloys, e.g. producing np-Pt from amorphous Pt-Si [11], producing np-Au from intermetallic Au_1Al_2 [74], and fabricating np-Cu [75] and np-Ag [76] by multiple phases intermetallics.

In addition to using the XRD to determine the precursor alloy composition, it can also be used to track dealloying. Figure 4.6 displays a series of XRD scans during dealloying a NiCu film. With dealloying going, the intensity of the alloy peaks gradually

decreased. In addition to intensity decreasing, the peak position shifted during dealloying as well. The (111) peaks of pure Ni and Cu are at 43.32 °and 44.50 °respectively. The (111) peak of NiCu alloy was shifting left toward Ni (111) during dealloying. It makes sense since the sample became more and more Ni richer as dealloying going. This method also worked for NiFe, NiAl alloys even their XRD scans were not indexed.

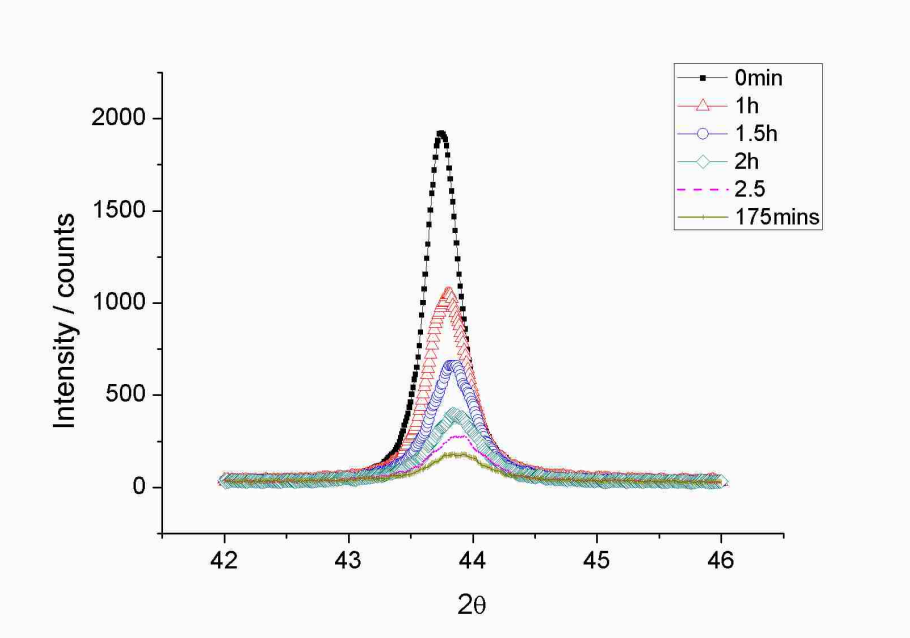

Figure 4.6. A series of X-Ray scans in small range of 42° to 46° during dealloying of a Ni-Cu film. The plot shows the X-Ray peak decreased and also shifted during dealloying.

One strange thing observed in all the XRD scans is that the dealloyed films displayed no peaks or a very broad short peak (as shown in Figure 4.6, the curve at 175 minutes) if ruling out the peaks from Si substrate. The same phenomenon was noticed for np-Pd and np-Ir thin film as well. It's not clear why np-metals films were invisible in XRD. It may be caused by size effect of ligaments. As learned from Cullity and Stock's book [73], decreasing grain size or film thickness can cause peak broadening. It's likely that the fine ligaments (<10 nm) in the dealloyed film broadened the XRD peak so that it's not

distinguished in scans. In a previous study by Sun Ye in the author's group, he observed Au (111) peak in np-Au by dealloying of AuAg films. One distinctive difference of np-Au from np-Ni, np-Pd and np-Ir is that np-Au had ligaments between 10 nm-30 nm, larger than those of np-Ni, Pd and Ir, which had ligaments less than 10 nm.

4.4.4 XPS measurement

XPS was used to evaluate the dealloyed co-deposited NiAl film, and indicated oxide ligaments in dealloyed film, as discussed in previous section. XPS was also performed on np-Ni generated by dealloying NiMg precursor to determine whether the Ni was metallic or oxidized.

Figure 4.7 displays a series of individual scans (in the vicinity of the Ni 2p peak) for various Ni samples. The purple open squire and red open circle curves are scans of np-Ni films respectively before and after thermal cycling. The peaks matched well with Ni_2P peaks upon oxidation according to handbook of x-ray photoelectron spectroscopy [77]. For comparison the same scan was performed on a thicker, fully dense Ni foil. This generated a scan which matched with oxidized Ni 2p peaks, solid green diamond curve in Figure 4.7. It makes sense considering Ni is easily oxidized once upon in air. To remove the oxide layer from this dense Ni foil, it was ion milled for 10 minutes, and then measured again. This scan, as the blue cross curve in Figure 4.7, was different from all other scans, and agreed well with standard scans for pure Ni [77]. All of these results suggested that np-Ni was oxidized, both in as-dealloyed and thermally cycled forms.

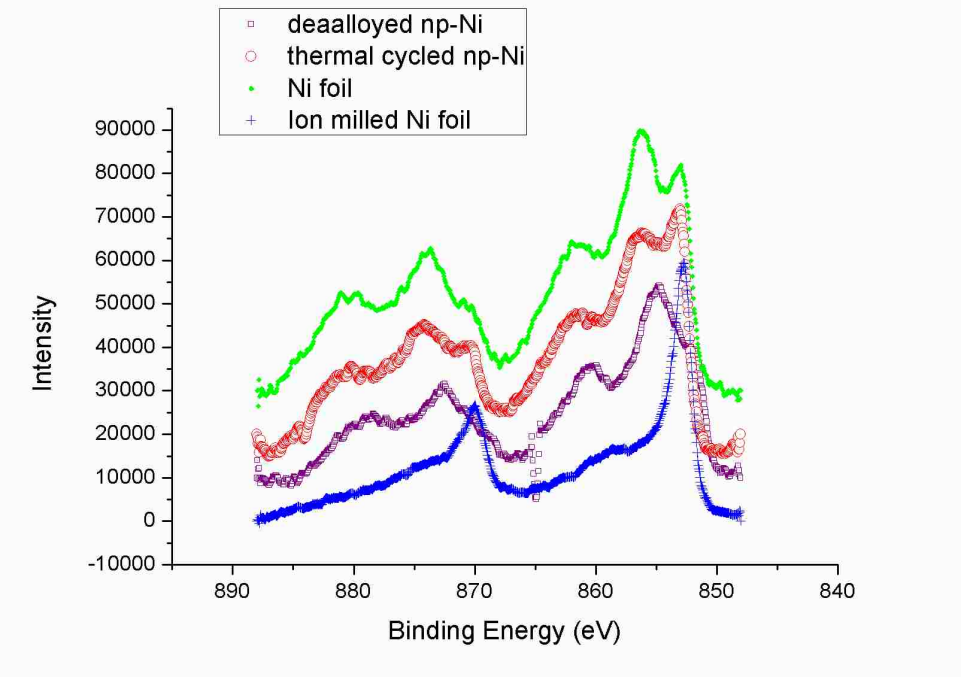

Figure 4.7. XPS scans of various nickel samples, in the range of the Ni_2p energy window, to determine the extent of oxidation in np-Ni. For reference, a thick foil of pure Ni was analyzed before (purple line) and after (green line) ion milling of its surface, to obtain spectra for oxidized and metallic Ni, respectively. Both the as-dealloyed (blue line) and thermally cycled/annealed (red line) NiMg films generated scans that suggested the Ni had been oxidized.

4.4.5 Cyclic Voltammetry (CV)

Initially, CV scans were planned to assess the electrochemical performance of np-Ni thin films. Kong et al. demonstrated that porous films consisting of NiO or $Ni(OH)_2$ performed as good energy storage materials [78]. The same set-up were used in our experiment. However, the dealloyed np-Ni films didn't display high current density as in their experiments. The measured CV curves, which are shown in Figure 4.8, agreed well with the CV scan of a porous metallic Ni film, which were also obtained by Kong, et al. According to their study, nickel oxide or nickel hydroxide would exhibit ways higher peak

density at different peak position. The CV test results indicated that the dealloyed np-Ni films consisted of metallic Ni, not np-NiO.

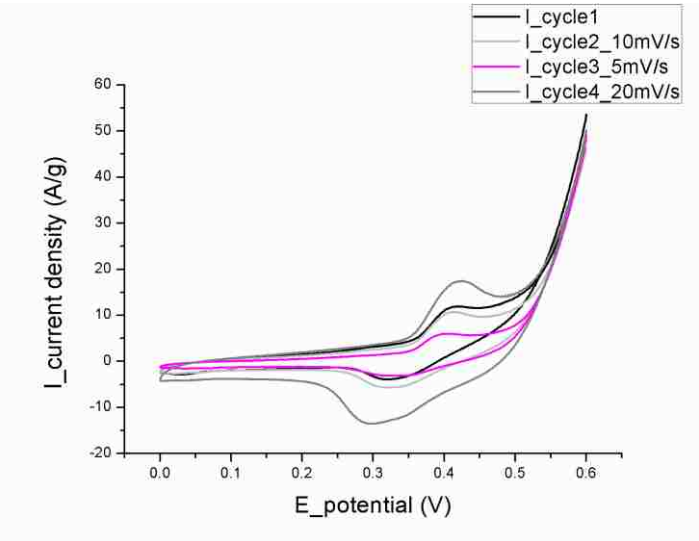

Figure 4.8. CV scans for a dealloyed 100 nm np-Ni film after thermal cycling. The first CV scan was performed at a rate of 10 mV/s, while the second to the fourth scans were run at 10 mV/s, 5 mV/s, and 20 mV/s, respectively.

The CV scans therefore delivered results that might seem to contradict the XPS results. However, considering that XPS analyzes surface regions ≤ 2 nm thick, and the thickness of native oxides on Ni is typically less than 1 nm [71]. One explanation of these results is that np-Ni was only oxidized at a 1-2 nm surface layer, the oxidized layer resulted in the Ni 2P peaks exhibited Nickel oxide character. However, in CV test, the metallic Ni core in ligaments overweighed the relatively small amount of Ni oxide on surface, therefore it performed the behavior should be observed in metallic Ni. This hypothesis would be verified by ion milling of the np-Ni film. However, due to failure of XPS, it was not tested. Nonetheless, the analysis of these results suggests that np-Ni ligaments may form a core-shell structure with pure Ni core covered by a thin layer of native oxide. In the CV tests, this Ni oxide layer was not sufficiently thick to dominate the performance, and the material still behaved like metallic nickel.

4.4.6 Stress evolution during dealloying

The measurements in the following sections are all based on np-Ni created by dealloying NiMg films.

The stress measured in a thin film NiMg during dealloying was plotted, as shown in Figure 4.9. In the plot, the film stress was almost neutral at the beginning, but once upon dealloying, it increased quickly and settled at ~120 MPa (tensile). Further dealloying, resulted in stress decreased slightly, to ~100 MPa. The tensile stress caused in dealloying is in agreement with the previous study on AuAg dealloying. The peak in stress, which occurred at very first a couple section, likely corresponds to the point at which most Mg has been removed from the sample. Further dealloying (to hundreds of seconds) caused slightly decreasing of film stress, which probably is due to ligament coarsening and minor microstructural changes.

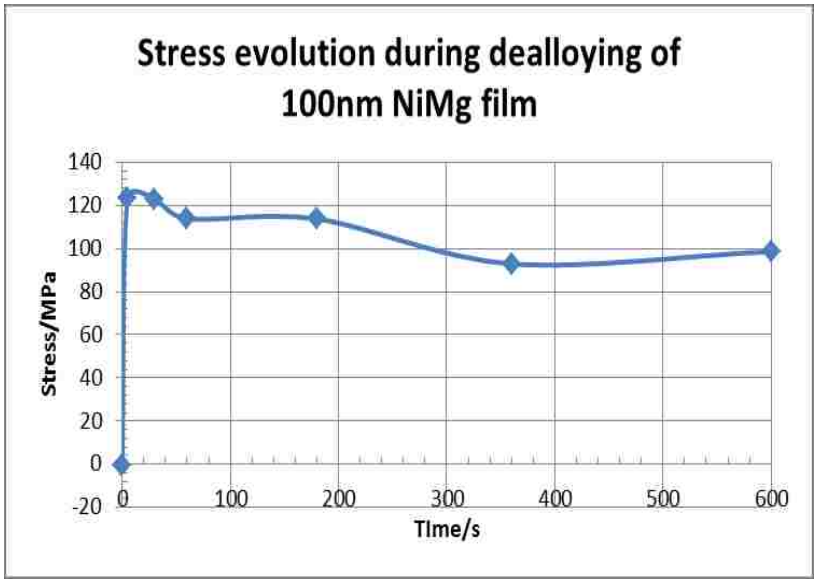

Figure 4.9. Stress evolution during dealloying of 100 nm NiMg film, measured using a wafer curvature apparatus. Stress in the precursor alloy film is approximately zero, but rapidly enters the tensile state upon dealloying.

4.4.7 Thermal cycling behavior

Thermal cycling experiments were performed on thin film np-Ni samples in the wafer curvature system, to determine the thermomechanical behavior of np-Ni. Typically, cooling a thin film from high temperature would cause the stress increased linearly. If a knee point occurs in cooling, where the linear increasing of the stress is interrupted and stress is still increased but not lined up with stress below. As in classic stress-strain curves, this knee point is a transition from thermoelasticity to thermoplasticity. Therefore, it gives information about the yield point. However, in the temperature range studied (room temperature to ~250˚C) here, the stress only displayed some arbitrary properties, which can't belong to either elasticity or plasticity, as shown in Figure 4.10.

The thermal cycling experiments revealed two interesting types of behavior in the np-Ni films, as shown in Figure 4.10. First, during initial heating (red curve), the film stress experienced a sudden drop at ~110˚C and then increased rapidly to an even higher stress level. This stress drop and rapid recovery was followed by an increase in stress from the compressive regime to the tensile regime. This phenomenon was consistently observed during most of the thermal cycling experiments for np-Ni in forming gas (a mixture of hydrogen and nitrogen, which establishes a reducing environment and hinders oxidation of the np-Ni). It is not clear why the films behaved this way during their first heating segments. One possible explanation is that the stress drop is due to a change in the passive oxide film on the Ni ligament surfaces, perhaps resulting from the adsorption/absorption of hydrogen on/into the np-Ni [79]. The rapid increase in stress following this drop is likely the result of reduction of the nickel oxide to metallic Ni on the np-Ni ligament surfaces. Typically,

oxidation of metal films induces compressive stress, and reduction of an oxide film induces tensile stress.

The second distinctive feature of np-Ni thermal cycling was the opposite stress trend in heating and cooling. After entering the tensile regime, stress increased with temperature going up (and vice-versa during cooling). As discussed earlier in section 3.3.1, stress should decrease while heating to higher temperature (and vice versa in cooling), for most of the metallic films. This is due to the higher thermal expansion coefficient of metal (Ni in this case) versus silicon (the substrate material). However, in curves shown in Figure 4.10, stress exhibited no obvious increasing or decreasing trend. Relating this observation to the feature discussed in the previous paragraph, a possible explanation is that hydrogen absorbed into the np-Ni metallic lattice (and did so readily once the oxide was reduced by the forming gas), but with temperature increasing, less hydrogen was contained within the Ni lattice and gradually desorbed from the np-Ni. The hydrogen desorption process would lead to a volume expansion of the Ni ligaments, which would manifest itself as a shift toward tensile stress. It is noted that a similarly thermal slope was measured for np-Pd during thermal cycling in forming gas as well. Palladium is extremely effective hydrogen absorber, and the nanoporous structure causes np-Pd to absorb and desorb hydrogen much more rapidly than dense Pd. Therefore, this phenomenon may be typical for np-metals which are good hydrogen absorbers.

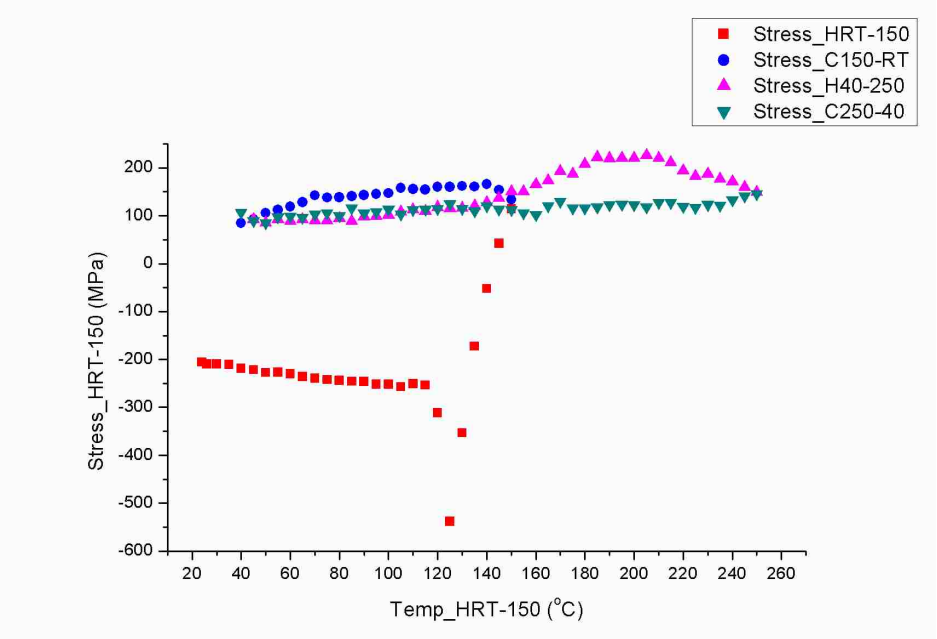

Figure 4.10. Stress-temperature plot from repeated thermal cycling of an 80 nm np-Ni film in forming gas (flows rate of 5 cfh for N_2 and 0.17-0.2 cfh for H_2). During the first heating segment, stress decreased suddenly at ~110˚C and then increased rapidly into the tensile regime, where it stayed for the remainder of two thermal cycles.

4.4.8 Thin film stress relaxation experiments

In addition to thermal cycling in the wafer curvature system, thin films were subjected to stress relaxation experiments at constant elevated temperatures in order to determine the diffusion mechanism(s) that operate in np-Ni in the vicinity of ~200˚C.

The relaxation behavior in materials can be described by a Maxwell model. And an exponential decay equation can be used to describe it, as shown in Equation 4.2.

$$\sigma(t) = \sigma_0 \, exp(-\frac{t}{\tau}) \qquad \text{Equation 4.2}$$

The detailed information about how to get this equation above is in chapter 2, section 2.8. The parameter τ in the equation is called relaxation time. The reciprocal of τ can be interpreted as a qualitative measurement of relaxation rate, and is related to the relaxation temperature in Kelvin by an Arrhenius-type rate equation as [61],

$$\frac{1}{\tau} = C\ exp(-\frac{Q}{RT}) \qquad \text{Equation 4.3}$$

$$ln\left(\frac{1}{\tau}\right) = -\frac{Q}{R}\cdot\frac{1}{T} + C_1 \qquad \text{Equation 4.4}$$

where C is a constant independent of temperature, R is the universal gas constant, and Q is the activation energy for the diffusion process.

From the relaxation curves, i.e. stress vs. time, the relaxation time can be determined by fitting the curves with exponential decay curves. Several stress vs. time curves were obtained at different relaxation temperatures for the same sample or samples prepared the same way by dealloying. And then the reciprocal relaxation time, $1/\tau$, was plotted out in the nature logarithm form versus the reciprocal of relaxation temperature, *1/T*. Multiple data points were fitted by a linear line, and slope of the line is *–Q/R*, according to Equation 4.4. Therefore, the activation energy, *Q*, is obtained. As discussed in the previous chapter, the mechanism of relaxation is diffusion. The diffusion mechanism (surface diffusion, grain boundary diffusion or bulk diffusion) can be determined by comparing the obtained activation energy with literature values.

Figure 4.11 presents the stress relaxation curves for an 80 nm np-Ni thin film at relaxation temperatures of 180˚C and 200˚C (hold time was 8 hours in each case). In the plots, the raw data are shown as gray points, the smoothed curve is shown as a gray line, and the fitted curves as colored lines. The data were fitted with exponential decay curves (ExpDec1 in origin software).

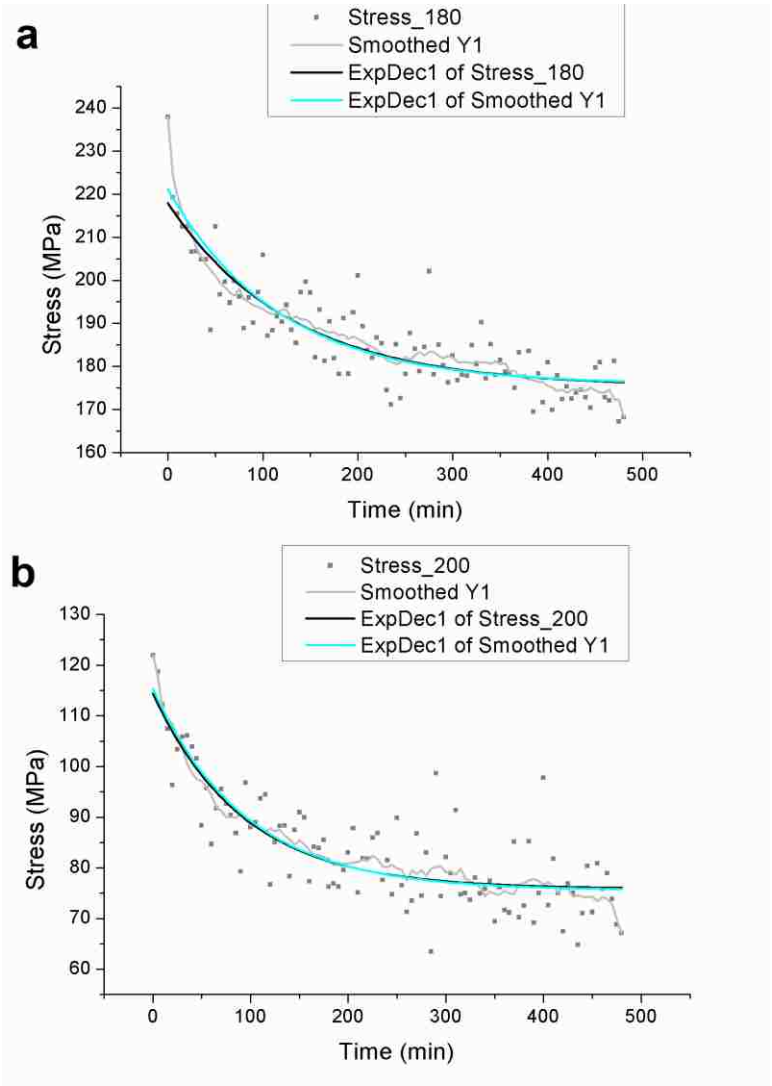

Figure 4.11. Stress relaxation curves for 80 nm np-Ni thin films relaxed at 180˚C (a) and 200˚C (b) for 8 hours in forming gas. The gray dots are raw data points, the light gray curve is smoothed curve based on the raw data points, black curve is fitting curve based on the raw data, and light blue curve is fitting curve based on smoothed data.

From the exponential decay fitting, the relaxation time τ was determined, as shown in Table 4.2. The relaxation times are an indicator of the validity of the stress relaxation. At higher temperatures, stress relaxation due to diffusion should proceed more rapidly, and therefore the relaxation time should be shorter. As shown in Table 4.2, τ does indeed decrease with increasing temperature and the fitted results are therefore physically plausible. Finally, the activation energy is calculated from plots of $ln(1/\tau)$ vs. $1/T$, as

illustrated in Figure 4.12. The calculation was performed for both smoothed data and raw data, as shown in Table 4.2 and Figure 4.12. The smoothed data yielded an activation energy of 0.20 eV (19.5 kJ/mol), while the raw data yielded an activation energy of 0.31 eV (29.4 kJ/mol).

Table 4.2. Summary of exponential fitting results for relaxation curves presented in Figure 4.11.

T/ ℃	T/K	1/T	τ	1/τ	ln(1/τ)	
180	453.15	0.002207	117	0.00854701	-4.76217	τ obtained from
200	473.15	0.002113	94	0.0106383	-4.54329	smoothed data
180	453.15	0.002207	128	0.0078125	-4.85203	τ obtained from raw
200	473.15	0.002113	92	0.01086957	-4.52179	data

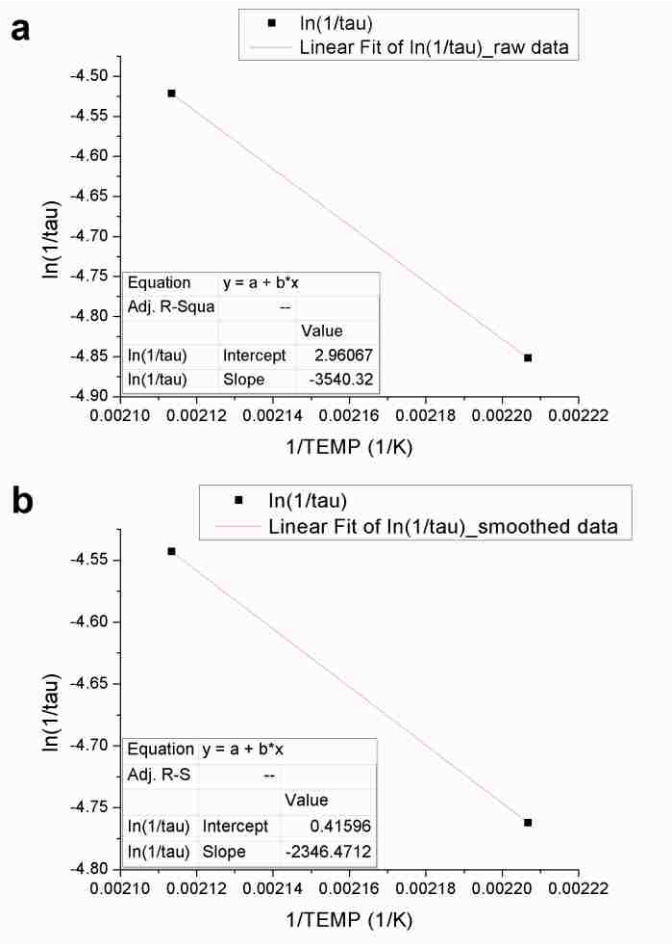

Figure 4.12. Arrhenius fitting of ln(1/τ) vs. I/T for the stress relaxation results in Table 4.2. (a) is the fitting curve based raw data, and (b) is the fitting curve based on smoothed data. The slope of the linear curve is *–Q/R*.

The range of experimentally determined activation energy (0.20 to .31 eV) is lower than most literature values for the surface self-diffusion of Ni (~0.7 eV) [80-83], and also lower than that for H_2 absorption into Ni (0.4 eV) [79]. Ultimately, given the limited amount of data (only two data points) and the consequent limited validity of this analysis, it was not possible to draw a conclusion regarding the active diffusion mechanism in np-Ni at these temperatures.

Nonetheless, based on the work in this project, it is proposed that elevated temperature stress relaxation of np-Ni may involve multiple mechanisms operating, including diffusion of Ni atoms on the surfaces of np-Ni ligaments, H_2 adsorption onto and diffusion into np-Ni ligaments, and oxidation or reduction of Ni ligament surfaces. These mechanisms may operate simultaneously, and if this were the case, would explain the difficulties in isolating and measuring the governing diffusion mechanism. One suggestion for mitigating some of the difficulties experienced in this study is, for metals such as Ni that are susceptible to oxidation or gas absorption, a vacuum environment could be established for cleaner thermal cycling and stress relaxation experiments.

4.5 Conclusions and future work

The goal of this project was the development of np-Ni as an alternative to Raney Nickel. This project was successful in establishing that thin film np-Ni can be produced using straightforward chemical processing that avoids the problems of Raney Nickel, namely its pyrophoricity and structural instability that limits it to powder form. Thin film np-Ni, as studied here, is crack-free and could be produced as a conformal coating for non-planar devices intended to operate in a catalytic or sensing application. Although we were not able to determine some details of the mechanical behavior of np-Ni, we demonstrated

that it is has thermal stability over a moderate temperature range, provided the operating environment is appropriate. In summary, the following was established during the course of this project:

1) Nanoporous nickel (np-Ni) can be synthesized from a variety of precursor alloys, including Ni-Cu, Ni-Al, Ni-Fe and Ni-Mg. The relatively straightforward process of dealloying produces a crack-free nanoporous structure with ligaments and pores on a length scale of 5-10 nm or larger (tens of nm).

2) Ni-Mg alloy films (with a composition of approximately $NiMg_2$) are the best precursors for producing np-Ni that is highly pure in Ni content, free of cracks, and exhibits the smallest ligaments and pores of any material investigated here.

3) Np-Ni ligaments have a native oxide coating but a metallic Ni core. This is a consequence of Ni's tendency to form a thin, protective native oxide, and does not hamper its ability as a catalyst.

4) Dealloying of Ni-Mg to produce np-Ni results in the extremely rapid removal of Mg, with a concomitant increase in film stress to ~100 MPa. The crack-free structure of np-Ni allows this tensile stress to be maintained during extended dealloying.

5) Np-Ni performed an anti-thermoelasticity tend over the temperature range of room temperature to 250 ℃, provided a reducing environment is maintained to prevent oxidation of the Ni surfaces. Np-Ni appears to absorb hydrogen, which affects the film stress.

Np-Ni reacted with forming gas somehow, which makes the determination of activation energy from relaxation of np-Ni in elevated temperature inaccurate. To carry out

thermal cycling or thermal relaxation to np-Ni, a vacuum environment is probably necessary to avoid chemical or physical reactions. Nonetheless, the thermal cycling or relaxation can be applied to nanoporous noble metals, which are not as vulnerable as Ni to O_2.

To understand the mechanism of atomic diffusion in np-metals, the effect of surface area has to be considered. To assess the effect of surface layer, a quantitative measurement of specific surface area of np-metals, for example by BEY, is necessary. Besides this, if a precise control of ligament size can be achieved, it would be very helpful to explore the effect of ligament size or geometry to specific surface. Another method to examine the mechanism of diffusion in np-metals is to utilize in-situ environmental TEM, (Dr. Guiton's group has an in-situ heating TEM holder, which can be heated up to 1000 ℃) to visualize atom movement in heating or relaxation.

Besides studying thermal mechanical behavior of np-Ni, the application of np-Ni should be considered in the future. The fine porous structure in np-Ni is promising to be used as a 3D frame in Li-ion battery. By coating Si or other anode material on it, it should work as a good anode material since it provides conductive network and also sufficient space for Li-ion intercalation and deintercalation.

5 Multilayer fabrication of np-Ir and np-Au thin films

5.1 Introduction

Due to the high surface-area-to-volume ratios, np materials are candidates for applications including catalysis [3], sensing [4, 40], actuation [5], etc. Multiple techniques have been developed to produce np materials, e.g., anodizing Al/Si to obtain porous alumina/Si [24, 84, 85], and, most commonly, using an inorganic sacrificial mold, assisted with a porous template, to produce another porous material [25]. The template-assisted method offers precise control of porous geometry, including pore size and ligament orientation. Recently, dealloying has become a common approach to fabricate np materials, especially np metals [10, 60]. Compared with the template-assisted method, dealloying is more straightforward and is effective at creating porous structure.

However, conventional dealloying does not allow precise control of pore size. Researchers have found that precursor alloy composition and dealloying conditions (etchant concentration, dealloying temperature, dealloying time, agitation of etchant) can significantly affect morphology of the dealloyed structure [27]. Average ligament size can be modified by adjusting these conditions, but dealloying typically produces a lognormal distribution of feature sizes. Other methods to alter ligament size include thermal coarsening [86] or using surfactants during dealloying [87]. However, quantitative control and predictable design of ligament geometry cannot typically be achieved by dealloying.

This chapter presents a multilayer fabrication method and demonstrates its success in creating nanoporous structures with controlled ligament size and orientation. This multilayer fabrication idea was inspired by Wayne Li, a former member in the author's group, from his study of ultrathin np-AuPd films [88]. Two precursor alloy systems, Ir-Ni

and Au-Ag, are considered, and this method should be applicable to fabrication of structured np metals in general. Films with various layer thickness were studied and the length scale of dealloyed np metals (np-Ir and np-Au) was tuned by the initial layer thicknesses, as revealed by both plan-view and cross-section micrographs.

5.2 Experimental

Fabrication of multilayer np films also includes deposition and dealloying, as the methods used in fabricating np-Ni thin films. Most of the experimental details were reduplicate of those in previous chapter. Only information different from them are presented here.

Note that, even multilayer deposition was studied in fabrication of np-Ni from Ni-Al precursor films, different from it, the multilayer IrNi/AuAg films are composed of pure Ir/Au layers and Ir-Ni/Au-Ag alloy layers. Multilayer films were deposited in the ORION sputtering system as well, by programming the gun shutters to open and close in a timed sequence. Four multilayer sequences were investigated here: (1) 5 layers of 10 nm Ir-Ni alloy, each separated by a 1 nm pure Ir layer; (2) 10 layers of 5 nm Ir-Ni alloy, separated by 0.5 nm pure Ir layers; (3) 3 layers of 20 nm Au-Ag alloy, separated by 2 nm pure Au layers; and (4) 10 layers of 10 nm Au-Ag alloy, separated by 1 nm pure Au layers.

Ir-Ni precursor alloy films were dealloyed using a two-step process. First, these films underwent free corrosion in diluted nitric acid (1 part stock 68% HNO_3 : 1 part distilled H_2O), with the solution maintained at 50˚C. Second, electrochemical dealloying was performed in diluted nitric acid (1 HNO_3 : 9 H_2O), with constant DC voltage of 1.35 V. Third, voltage was increased to 1.4 V for the final stage of dealloying. For the precursor film with 10 nm Ir-Ni alloy layers, the times for each step were 1 hour, 7 hours and 21

hours. Times for the film with 5 nm Ir-Ni alloy layers were 17 hours, 4.25 hours and 7.25 hours. The second dealloying step was stopped when current flow from the sample settled to a plateau value near zero.

Multilayer Au-Ag films were also dealloyed in nitric acid. However, dealloying was performed completely by free corrosion, using concentrated nitric acid. The precursor film with 20 nm Au-Ag layers was dealloyed for 10 min. The film with 10 nm Au-Ag layers was used to investigate microstructural evolution during dealloying, by stopping the dealloying process at intermediate times, before dealloying was complete. Individual film samples were removed from the etchant at various times (1 min, 3 min, 5 min, 8 min) and rinsed to prevent further dealloying.

Characterization for dealloyed films were performed in the same SEM and EDS system (S900 and S3200, Hitachi) to investigate surface and internal morphology, and composition.

5.3 Results and discussion

5.3.1 Multilayer np-Ir films by dealloying of IrNi multilayer films

The SEM images of dealloyed IrNi films are shown in Figure 5.1. The layered structure exhibited in both 10 nm-layer and 5 nm-layer films, as shown in Figure 5.1a and 5.1b respectively (all the cross-section images were recorded with the Si substrate below the film). The layered structure went through the entire film thickness. Differences in layer thickness are apparent in the two types of films. Due to the sequence of deposition (pure dense Ir layer was deposited under Ir-Ni alloy for each layer), 4 dense pure Ir layers were identified in the 5-layer film, and 9 dense pure Ir layers were observed in 10-layer film. In

addition to cross-section images, plan-view micrographs are also presented in Figure 5.1c and 5.1d. The surface morphology differed significantly for films with 5 nm IrNi layers and 10 nm IrNi layers. Film with thicker alloy layers exhibited larger ligament size, with an average ligament width of 7 nm. Due to the extremely small ligament in 5 nm-thick-layer film, the ligament width is not determined, but a rough estimation is about 3-5 nm. The EDS measurement indicated that the dealloyed films have Ir contents of 90.3 at.% and 79 at.%, respectively for 10 nm-layer and 5 nm-layer films.

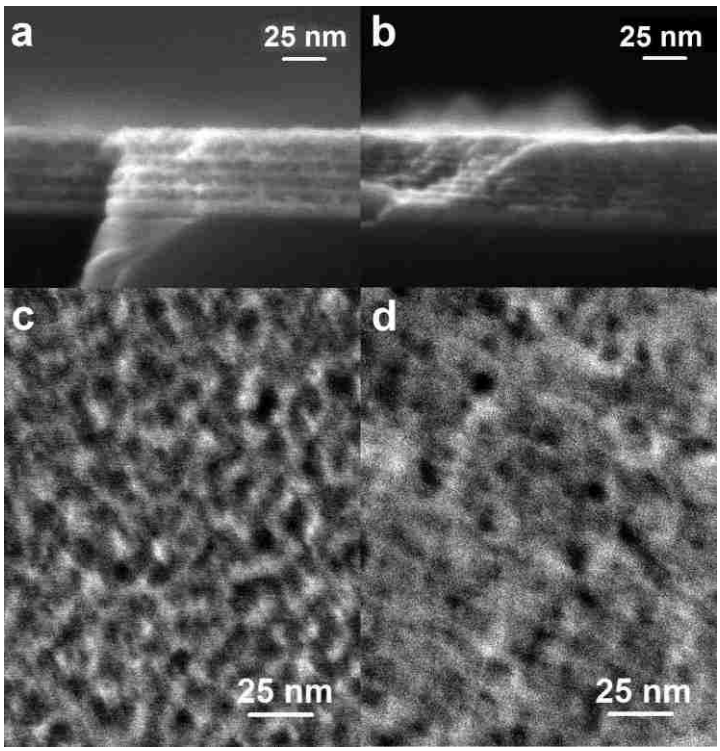

Figure 5.1. (a) Cross-section SEM image of np-Ir fabricated by dealloying an Ir-Ni multilayer film that originally consisted of 10 nm Ir-Ni alloy layers, each separated by a 1 nm pure Ir layer (5 sets of layers in the precursor film). Average spacing of each layer (porous layer + pure Ir layer) was 8.7 nm. The Si substrate is located below the film in each cross-section micrograph. (b) Cross-section SEM image of np-Ir created from precursor with 5 nm Ir-Ni alloy layers and 0.5 nm pure Ir layers (10 sets of layers in this precursor). Average spacing of each layer was 5.2 nm. (c) Plan-view SEM image showing nanoporous surface morphology of the film from image (a). (d) Plan-view SEM image of surface morphology for the film from image (b).

5.3.2 Multilayer np-Au films by dealloying of AuAg multilayer precursor film with 20 nm alloy layer

The SEM images in Figure 5.2 illustrate the dealloyed AuAg film with 20 nm-thick-AuAg-layer. Each individual layer clearly displayed in cross-section image, as in Figure 5.2a. The pure dense Au layers looks thicker than the expected thickness in deposition. It's probably due to the Au atom diffusion and agglomeration during dealloying. Between the dense Au layers, small short Au ligaments spanned over the layers, and oriented vertically to the pure Au layer. Surface morphology of the film is shown in Figure 5.2b. It revealed a different morphology than typical nanoporous metals. The top ligaments appeared to be shorter, more similar to nanoparticle. Comparing with the cross-section image in Figure 5.2a, the topmost ligaments stood perpendicular to the supporting layer, and therefore, the ligaments displayed on plan-view image are viewed along their length. Average ligament width was measured to be 23.3 nm and 24.5 nm, respectively from plan-view image and cross-section image. The EDS measurement indicated the dealloyed film has 100 at% pure Au.

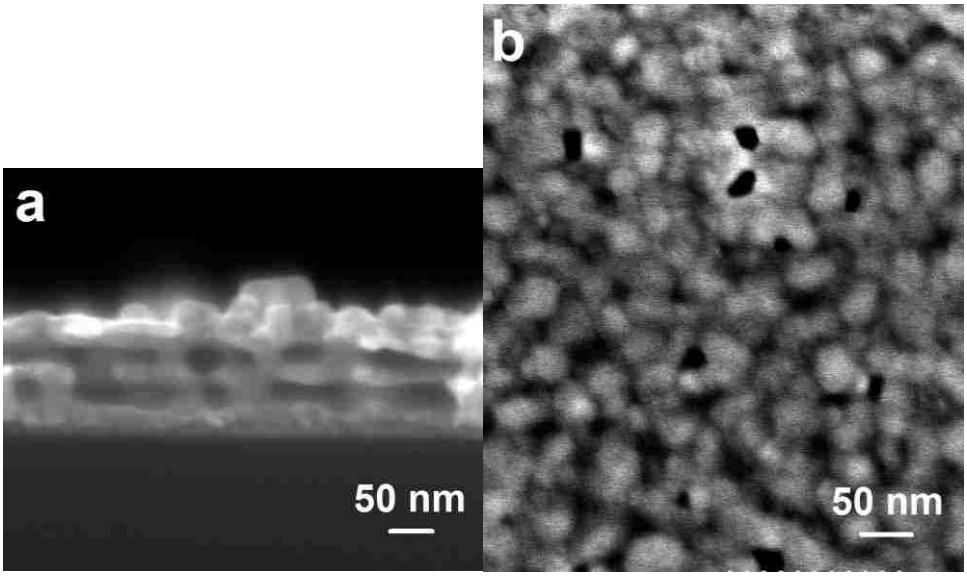

Figure 5.2. SEM micrographs of np-Au dealloyed from precursor multilayer with 20 nm Au-Ag alloy layers and 2 nm pure Au layers (3 sets of layers in the precursor). (a) Cross-section and (b) plan-view images of the same film, showing layered architecture through the film thickness and ligaments oriented perpendicular to the layers, including short ligaments protruding from the film surface. Average spacing between layers of ligaments was 20.9 nm.

5.3.3 Multilayer np-Au films by dealloying of AuAg multilayer precursor film with 10 nm alloy layer

The dealloying evolution in multilayer AuAg film was studied on a film with 10 nm thick Au-Au layer. Cross-section images of the film with dealloying times of 1 min, 3 min, 5 min and 8 min, are presented in Figure 5.3. Dealloying started from top film, as shown in Figure 5.3a. Only a few nanoporous layers were observed at the first minute. Dealloying went down quickly, and almost attacked the entire film thickness after 3 minutes, and about 8 layers were observed in Figure 5.3b. The layered structure went through the whole thickness after 5 min, as seen in Figure 5.3c, but some places (the right side of Figure 5.3c) started to appear randomly oriented ligaments. Further dealloying

resulted in disappearing of the layered structure, and the ligaments went to a random orientation, seen in Figure 5.3d, as those in typical non-layered np structure by dealloying of co-deposition film. Note that the dealloying front was not perfectly straight, due to initiation of dealloying at certain locations, and dealloyed structure was therefore not the same in every part of the film (e.g., Figures 5.3a and 5.3c). Similar to other multilayer structures with different layer spacing, bridging ligaments were oriented perpendicular to the bounding layers.

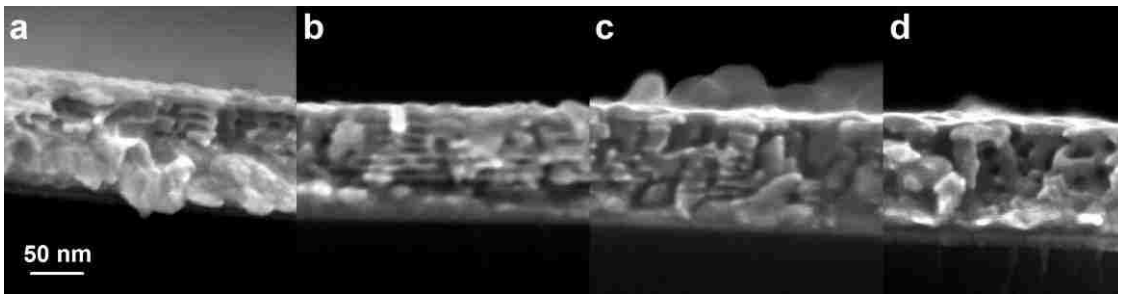

Figure 5.3. Cross-section SEM images of np-Au from multilayer with 10 nm Au-Ag alloy and 1 nm pure Au layers (10 sets of layers in this precursor). Individual samples were dealloyed for (a) 1 min, (b) 3 min, (c) 5 min and (d) 8 min. Average spacing between layers of ligaments was 10.8 nm, measured from image (b).

The corresponding plan-view SEM image of the film were also obtained, as shown Figure 5.4. The surface morphology experienced noticeable change as the dealloying going. The ligament size increased progressively, from 10.2 nm to 17.9 nm, as listed in Table 5.1. The most distinguishable ligament coarsening happened when the structure started to lose the layered structure. The composition in each dealloying step was also measured, and listed in Table 5.1. The Au content was 86.6 at.% after dealloying of 8 min, indicating the dealloying didn't complete yet.

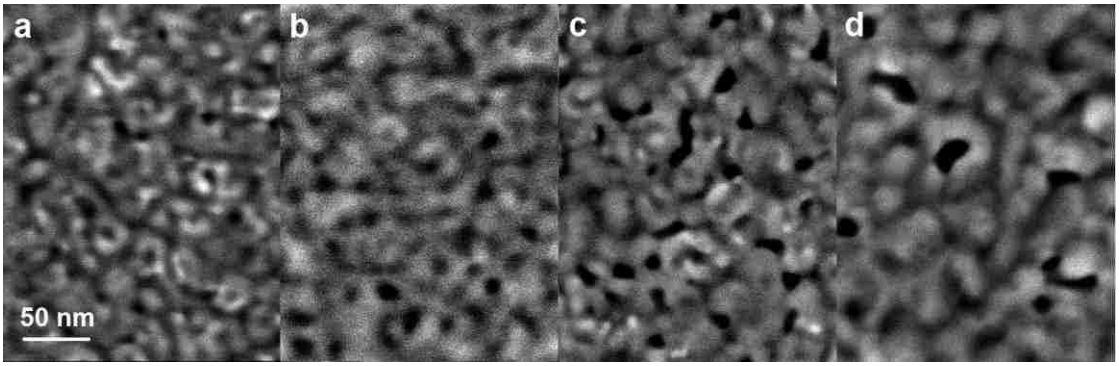

Figure 5.4. Plan-view SEM images of np-Au from multilayer Au-Ag, after dealloying times of (a) 1 min, (b) 3 min, (c) 5 min and (d) 8 min. Ligament width increased gradually with dealloying time, especially when the multilayer np structure evolved into randomly oriented ligaments.

Table 5.1. Summary of composition and ligament size in np-Au (created from multilayer with 10 nm Au-Ag alloy layers) at different dealloying times.

Dealloying time (min)	0	1	3	5	8
Composition (at.% Au)	46.8	57.6	69.6	80.5	86.6
Ligament size (nm)	n/a	10.2	13.5	14.5	17.9

5.3.4 Comparing dealloying of multilayer IrNi and AuAg films

Ease of dealloying and stability of multilayer np structure differ for each system. Dealloying involves competing processes of sacrificial element dissolution and surface diffusion of remaining elements to form ligaments. Compared with multilayer Ir/Ir-Ni films, dealloying multilayer Au/Au-Ag films was more readily and more quickly. However, due to the higher surface diffusivity of Au atoms [89], the layered np structure in the Au-Ag system is less stable and dealloying time must be carefully selected. As shown in Figure 5.3, dealloying for 3 min was insufficient, while the layered structure began to break down after 5 min dealloying. In contrast, surface diffusivity of Ir is three orders of magnitude lower than that of Au [89, 90], allowing the layered np structure to persist for hours in the

dealloying etchant. Moreover, np-Ir films retain this layered structure during thermal cycling to 500˚C [23]. Given the higher surface diffusivity of Au versus Ir, and based on the loss of multilayer structure during extended dealloying of np-Au (Figures 5.3c-d), thermal cycling of np-Au would likely erase the layered structure and produce a coarser nanoporous structure with randomly oriented ligaments.

5.3.5 Discussion of the multilayer fabrication approach

Dealloying of multilayer precursors creates multilayer np films with periodic cell size and ordered ligament layers through the film thickness. For Ir/Ir-Ni multilayers, 10 nm alloy layers resulted in average spacing of 8.7 nm between layers of ligaments (for 5 nm alloy layers, the corresponding spacing was 5.2 nm). For Au/Au-Ag multilayers, 10 nm alloy layers resulted in spacing of 10.8 nm (for 20 nm alloy layers, corresponding spacing was 20.9 nm).

In addition to periodic spacing of ligament layers (which are porous and consist of in-plane, randomly oriented ligaments), the ligaments that bridge these layers are oriented perpendicular to the bounding layers. This is in contrast to the randomly oriented ligaments observed in typical nanoporous metals and alloys, but is similar to results from a study of ultrathin np-AuPd films [88]. An underlying pure metal layer tends to orient adjacent ligaments perpendicular to this layer, as seen in Figures 2a and 3b. Taken together, these results indicate that bounding a nanoporous layer with two dense and/or oriented ligament layers causes ligaments to form a perpendicular bridge between these two layers.

It is hypothesized that pure, dense Ir or Au layers “seed” a layer of ligaments in the dealloyed np structure. This facilitates a degree of design control over geometry and periodicity of the dealloyed film. This approach works if the pure, dense layer is

sufficiently thin that it does not prevent the dealloying front from progressing to the underlying alloy layer. Control over final np geometry likely exists within a finite window, i.e., length scale of ligament width and spacing between ligament layers can only be modified within a certain range near the "natural" ligament/pore size that results from dealloying of homogeneous alloy films. For np-Au, the range is predicted to be 5 to 50 nm, and for np-Ir, the range should cover a smaller length scale region of 3 to 30 nm. This statement is based on the observations and measurements in the current study, as well as ligament and pore sizes measured in the authors' other work on thermally cycled np-Au and np-Ir.

This approach using multilayer precursor alloys should be generally applicable to the fabrication of other structured np metals as well. Metals with higher surface diffusivity, such as Au and Ag, should form np structures with larger ligament width and spacing, compared to metals with lower surface diffusivity such as Ir and Ni. The surface diffusivity thus represents a control parameter in the design of np length scale. However, the latitude for controlling ligament size and spacing appears to be a factor of 10, with the average magnitude (natural ligament size of the np metal) determined by surface diffusivity, etchant and thermal treatment. With proper design of the precursor film, a predictable length scale with multilayer architecture can be achieved.

5.4 Conclusions and future work

In conclusion, structured np-Ir and np-Au were successfully fabricated by dealloying Ir/Ir-Ni and Au/Au-Ag multilayer precursor films. By adjusting the alloy layer thickness, np-Ir and np-Au with a range of controlled ligament sizes were achieved.

Multilayer precursors led to nanoporous films with a layered architecture, including periodic spacing and preferred ligament orientation.

With proper selection of precursor alloy and dealloying, np-metals other than np-Au and np-Ir should also be generated in multilayer architecture with this multilayer fabrication method. With the experiences in making nonlayered np-Pd, np-Ni, np-Si in the author's group, these system can be investigated. And further work should focus on exploiting their applications. Possible applications of these np metals includes hydrogen sensor (np-Pd), catalyst (np-Ni), optical applications (porous Si) [85].

6 Fabrication and mechanical behavior study of thin film np-Ir

6.1 Introduction

This project is funded by NSF CAREER grant, and the full title is understanding nanoscale deformation by characterizing the mechanical behavior of nanoporous noble metals. As part of CAREER project, np-Ir was studied as one of np noble metals (np-Au, np-Pd, and np-Ir). Fabrication and mechanical behavior of np-Au had been studied a lot. Ir is the second densest element in the earth, and the most corrosion-resistant metal, which makes np-Ir should be relative easily fabricated by dealloying. However, unlike other fcc metals such as gold, Ir is reported to be very 'brittle' in bulk form. The study on np-Ir would extend our knowledge about np-metals, and nanoscale mechanical behavior.

One objective of this study is to synthesize np-Ir in thin film form, and study mechanical behavior of thin film np-Ir. Another objective is to study the classic scaling laws from Gibson and Ashby and make necessary modification. As discussed in Chapter 2.4, some issues appear when applying Gibson and Ashby's scaling laws to explain mechanical properties of np metals, due to mediate relative density range and nanoscale ligament size in np metals. The study is to answer the question: to what degree the scaling laws accurately describe the behavior of np metals. And with both experimental and modeling, modified scaling equations are proposed to reflect the scaling behavior of np metals and alloys.

6.2 Challenges and methodology

The following is potential challenges in this study:

1. One of the challenges is to fabricate np-Ir without volume contraction. In the previous study of Thomas Kong in the author's group, he was able to make np-Ir with high purity and fine ligaments. But the only problem is that the film contracted a lot in dealloying (the dealloyed film has only half of the original thickness). This technique has to be improved to avoid the huge volume change.
2. Iridium is brittle compared with other fcc metals. It may cause trouble in dealloying and handling, such as cracking and pulverization. However, previous experience in dealloying AuAg suggested that carefully selection and proper dealloying condition can prevent these problems.
3. Due to the very fine ligament size (< 3 nm), imaging individual ligament of np-Ir is not an easy job under SEM. As shown in later section of this chapter, the author has to go to TEM (STEM) to visualize the details of the porous structure. While preparing TEM samples are more time consuming than preparing SEM samples.

Fabrication of np-Ir had been studied by a previous student in the author's group [91]. Therefore, np-Ir was created following his study. Ir-Ni alloy was selected as the major precursor because Ir-Ni form a solid solution in phase diagram. And Ir is highly corrosion resisted, so it's easy to select etchant for dealloying. Diluted nitric acid was used as etchant. To give more control in the dealloying, electrochemical dealloying (by applying constant voltage) was also performed on the film.

Additionally, IrMg precursor alloy films were also studied to fabricate np-Ir. Due to the successful fabrication of np-Ni from NiMg precursor, IrMg was believed to be able to yield np-Ir as well. Therefore, IrMg thin films were dealloyed to testify the efficiency of this Mg precursor method.

In addition to the regular fabrication of np-Ir by dealloying of co-deposited IrNi precursor films, multilayer films with Ir sublayers and Ir-Ni alloy sublayers were also prepared. Multilayer IrNi films had the advantage of being able to control ligament size at ease, therefore providing np-Ir with predictable structure and ligament geometry.

The thermomechanical behavior of a 300 nm multilayer np-Ir film was studied by thermal cycling. Due to thickness contraction during successive thermal cycles, the np-Ir film had a different relative density during each cooling cycle, allowing modulus and strength to be measured as a function of density. The biaxial moduli measured from separate thermal cycles were used to determine the scaling behavior of elastic modulus with relative density.

Characterization of np-Ir films were performed with similar methods as for np-Ni films. SEM, EDS, TEM were the major tools used in this study as well.

6.3 Experimental

Most of the experimental methods were introduced in the previous chapter of np-Ni, e.g. characterization methods. Information which had been presented in previous chapter will not be presented in the following sections.

6.3.1 HV magnetron sputtering

Same as Ni alloy films, three-inch diameter (100)-oriented silicon wafers, with thickness of 180 μm or 380 μm, were used as substrates for deposition of the precursor alloy films. Ir (99.9%) and Ni (99.99%) or Mg (99.95%) were sputtered in the AJA ORION high vacuum deposition system by flowing Ar gas at 2.5 mtorr. Still, 10 nm Ta was

deposited as an interlayer before the alloy film. Thin films were co-deposited or sequentially deposited (as multilayers) with total thicknesses of 100-500 nm.

Multilayers IrNi films were deposited the same way as those multilayer film in Chapter 5. The Ir layers were deposited for 0.5 nm, thin enough to avoid impeding dealloying from going through the film. The Ni and Ir targets were controlled by programing the gun shutters to open and close in a timed sequence in deposition. The deposited film had 55 layers, each layer contained a 0.5 nm pure Ir layer and a 5 nm IrNi layer.

6.3.2 Dealloying

Dealloying IrMg precursor alloy was straight forward, and was carried out in highly diluted acetic acid (*1HAc : 99H_2O*) by free corrosion for 5 min.

IrNi precursor alloyed was dealloyed by both free corrosion and applying voltage. The free corrosion was performed in ½ diluted HNO_3. The HNO_3 solution was slightly heated to 50 ℃. A dealloying time of 20h was necessary for 100 nm IrNi film. Electro-dealloying was used to save dealloying time. The solution was further diluted to 1 HNO_3: 9 H_2O. To figure out the critical potential for dealloying IrNi film, a linear potential/voltage sweep (-0.6V-1.6V) was generated from potentiostat (eDAQ), and applied to the sample. By identifying the knee point in the current vs. voltage curve, the critical potential was then determined (the detailed description of this method is in Chapter 2.2. As a result, a constant voltage of 1.2V was applied to the sample. The set-up is shown in Figure 6.1.

Note that working electrode, i.e. samples, should be placed in the solution carefully to prevent side effects, such as corrosion from clamps. For films deposited on a Si wafer, a narrow and long piece of sample was inserted partially in the solution, and

therefore no other reactions happened on working electrode side. The dealloying time with applying voltage is not generally fixed, instead is determined by the time at which the current in dealloying reached a plateau value near zero.

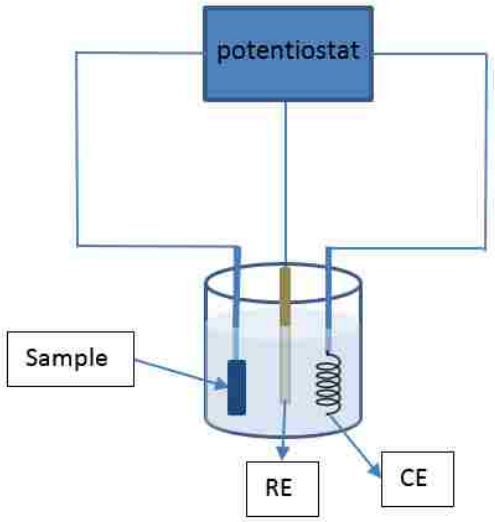

Figure 6.1. A schematic drawing of the three electrode dealloying setup. A Pt wire was used as counter electrode (CE), and a Ag/AgCl electrode was used as reference electrode (RE).

6.3.3 Characterization

Most of the characterization methods, i.e. SEM, EDS, XRD were operated the same way as those for np-Ni. However, transmission electron microscopy (TEM) was worked in both traditional and scanning transmission electron microscopy (STEM) modes to investigate the morphology and crystallography of np-Ir films.

6.3.3.1 TEM

Due to the extremely fine ligaments in np-Ir films, TEM (Jeol 2010f), specifically STEM, carried out by a high-angle annular dark field (HAADF) detector (Fischione), was

used as an assistant tool of SEM to characterize morphology. STEM was operated at 1 nm analytical probe size, and 25 cm camera length.

Before starting to prepare np metals TEM samples, very thin precursor films were deposited on Si substrate. Note that the Si substrate, used to prepare TEM samples, should have Si nitride and Si oxide finishing at least on one side. This Si nitride layer acted as a stopper in Si etching. And film thickness should be carefully selected to make sure the electron beam can go through the film. For np-Ir samples, a 50 nm precursor IrNi film was deposited on Si substrate.

Procedure to fabricate np-Ir TEM samples includes ultra-sonic cutting, grinding, dimpling, Si etching and finally dealloying. This procedure can be generally applied to other np metal thin film sample as well. Compared with sample preparation in other characterization methods, e.g. XRD and SEM, it's time consuming to make a TEM sample. Detailed steps to prepare a TEM sample are presented in the following.

First, undealloyed IrNi film (deposited on Si substrate) was first cut into discs of 3mm diameter by ultrasonic cutting (ultrasonic disc cutter, Gatan, model 601). Second, the small disc sample was mounted upside down, film side down, on a glass cylinder with crystal bond, and then grinded down to 80 μm (the starting thickness of the sample is about 190 μm, and 380 μm Si substrate would require more works in this step). Third, further grinding and polishing (also called 'dimpling') was performed on the sample with a dimple grinder (Gatan, model 656). After dimpling, a bowl-shape concave surface formed on the backside of the Si substrate, and the center of sample was about 10 μm, which can be identified by the color reflected from the center (10 μm Si exhibited an orange color). Finally, the remaining Si in the center was removed by etching in a mixture solution of

$2HNO_3$: 1HF: 1HAc. In this step, only the center part, which was dimpled in the previous step, underwent etching. The rest of the sample was protected by masking with micro-shield (SPI). The sample was then removed from the glass cylinder by dissolving the crystal bond in acetone. The sample was dealloyed before observing in TEM. A lot of cautions have to be used in each step. Following the steps above, a free standing np-Ir film (above 50 nm SiN) should be in the middle of sample, and TEM will be performed in this area. The procedure to prepare a TEM sample is illustrated in Figure 6.2.

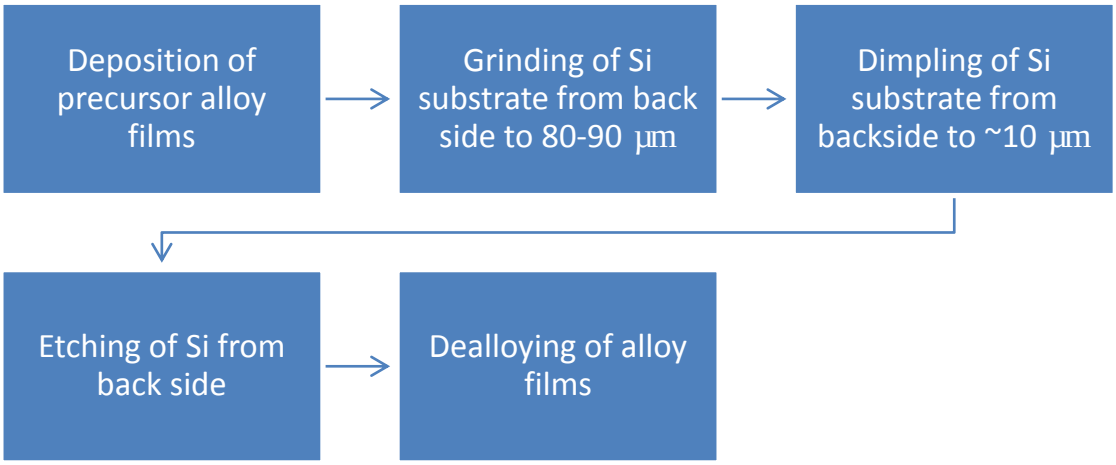

Figure 6.2. Procedure of preparing np-Ir thin film TEM samples.

Further imaging or analysis were conducted in TEM (Joel 2010f). Images were taken in both bright field mode and STEM high angle dark field mode. Additionally, diffraction patterns were obtained to characterize the crystal orientation of np-Ir.

6.3.4 Thermal cycling of np-Ir thin films

Same as the np-Ni films, thermal cycling was conducted to a 300 nm multilayer np-Ir film in the wafer curvature system (Toho FLX-2320-S). Np-Ir film underwent 5

cycles from room temperature to an elevated temperature. Different from thermal cycles of np-Ni thin films, a heating rate of 1 ℃/min and a cooling rate of -5 ℃/min were used for each cycle. The heating was kept at such a low rate so that it provided enough time for np-Ir underwent structure changes, e.g., ligament coarsening and thickness contraction. In thermal cycles, N_2 gas, instead of forming gas for np-Ni films, was flowed into the wafer curvature system to protect the film from being oxidized. The stress of the np-Ir film was measured and recorded every 5 minutes, and thus a stress vs. temperature curve was generated after each cycle. Witness samples were placed beside the wafer and sequentially removed after each cycle in order to determine film structure by SEM after each cycling segment.

6.4 Results and discussion

6.4.1 Linear sweep

Figure 6.3a is the current vs. voltage curve directly obtained from the linear sweep of a 100 nm IrNi in 1:9 diluted nitric acid. And Figure 6.3b is the absolute current density vs. voltage (i-E) curve in log-log scale.

Different from i-E curve in Figure 2.2, curve in Figure 6.3b exhibited some characters which were not seen in typical linear sweep of np-metals. This i-E curve displayed two branches, i.e. cathodic branch on the left, and anodic branch on the right, separated by free corrosion voltage (around -0.25V). Typical linear sweep, as in Figure 2.2, only includes segment in anodic branch. One feature in the anodic branch is the sample got passivated at about -0.1V. The passivation region and transpassive region are labelled as

in Figure 6.3b. The critical voltage was therefore determined from transpassive region, for a current at 10 mA, the corresponding voltage is around 1.2V.

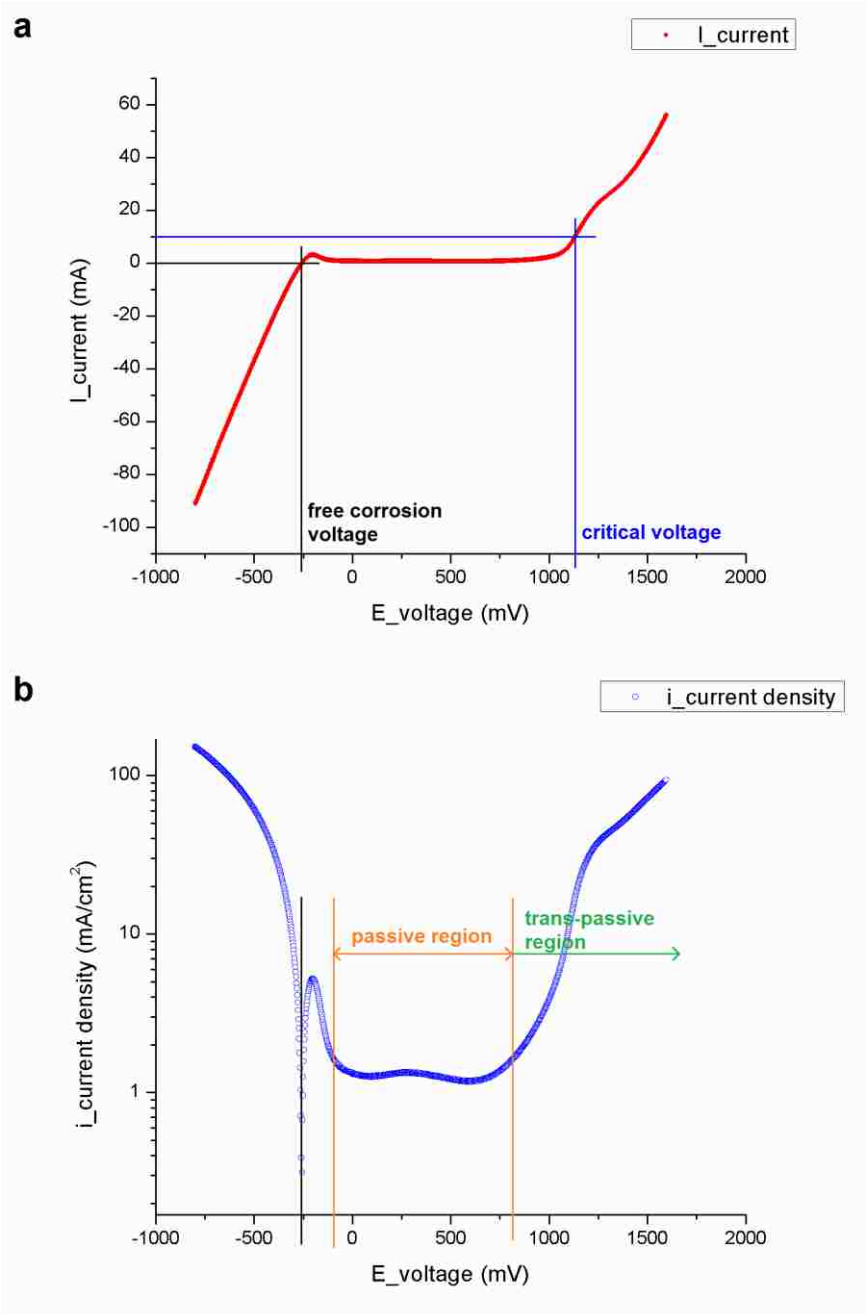

Figure 6.3. A linear sweep of 100 nm IrNi film in 1/10 diluted HNO_3. (a) Plot current vs. voltage; (b) Log-log plot of current density vs. voltage.

6.4.2 Optimal dealloying condition

Dealloying IrMg was quick and straight forward, i.e. it can be finished in highly diluted (1/100) HAc for a few minutes. However, it's not the primary method to prepare np-Ir films due to a huge volume contraction in dealloying IrMg, as that in dealloying NiMg. Instead, IrNi was used as the main precursor.

Dealloying IrNi precursor films took longer time. The optimal dealloying condition is listed in Table. 6.1. 20 hours was necessary to free corrode a co-deposited film. Whereas applying voltage can save quite amount of time, as seen in Table 6.1. The purity of the electrochemically dealloyed sample was higher than that by free corrosion.

Table 6.1. The optimal dealloying conditions for co-deposited thin film IrMg and IrNi precursors.

Precursor film condition	100 nm co-dep IrMg film	100 nm co-dep IrNi film	100 nm co-dep IrNi film
Etchant	1 HAc : 99 H_2O	1 HNO_3 : 1 H_2O	1 HNO_3 : 9 H_2O
Voltage applied	Non	Non	1.2V
Dealloying time	5 min	20h	Finished when the dealloying current from the sample settles to a plateau value near zero (typically 0.5-1h)
Heating	Non	50 ℃	Non
Agitation	Non	Non	Non

Multilayer IrNi film was dealloyed involving both free corrosion and electro-dealloying. First, the film underwent free corrosion in 1:1 diluted nitric acid for 17.5 hours,

with slightly heating at 50 ℃. Second, the film was electrochemically dealloyed in 1:9 diluted nitric acid by applying a constant DC voltage of 1.2 V to the sample for 5.5 hours.

6.4.3 Morphology of dealloyed films

Figure 6.4a displays the surface morphologies of np-Ir by free corrosion of IrMg precursor films. The ligaments are as small as 6 nm. However, one big problem in dealloying of IrMg is the huge volume contraction. An 86 nm thick precursor film had a thickness of only 47 nm after dealloying (as shown in Figure 6.4b Figure 6.4c), based on average measurement from more than 3 cross-section images.

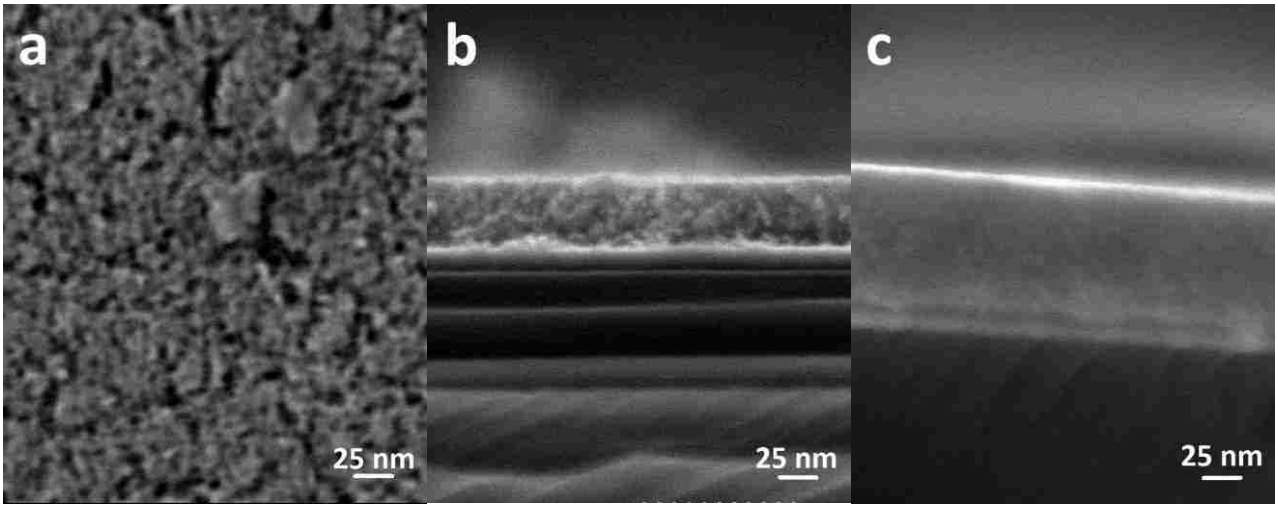

Figure 6.4. (a) Plan view and (b) cross-section SEM micrographs of np-Ir by free corrosion of IrMg thin film. (c) cross-section view of the film before dealloying. The film underwent huge volume contraction (up to half of its original thickness) during dealloying.

Figure 6.5 shows the plain view SEM images of np-Ir made by free corrosion and electro-dealloying of a co-deposited IrNi film. From the surface morphologies, no significant differences in the porous structure were observed, and both of them have fine structures with ligaments less than 10 nm (around 6-7 nm).

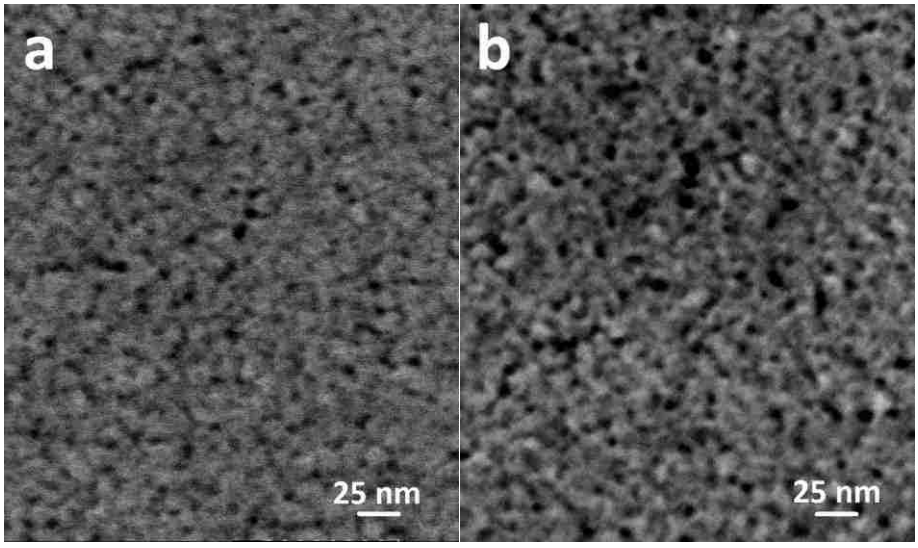

Figure 6.5. (a) Surface morphology of np-Ir by free corrosion of a 100 nm IrNi film. (b) surface morphology of the same film created by electrodealloying. They exhibite similar nanoporous strucutres. The ligaments were around 6-7 nm wide.

Figure 6.6 shows SEM plan-view and cross-section images of a multilayer film. The dealloyed film exhibited a layered nanoporous structure. Each porous layer was separated by a horizontal pure Ir layers. Most layers can be clearly distinguished, as shown in Figure 6.6b and 6.6c. One distinct feature of np-Ir is the perpendicular orientation of ligaments spanning over the pure Ir layers, as shown in Figure 6.6c. The ligaments width was very difficult to measure from plan-view image, as in Figure 6.6d. Indeed, the bottom layers were more easily identified than the top layers, as in Figure 6.6b. This difference in structure may be caused by a different extent of dealloying in the near-surface region versus that in the region near the film/substrate interface. Therefore, the ligament width was measured in cross-section image, which was determined as 3-4 nm.

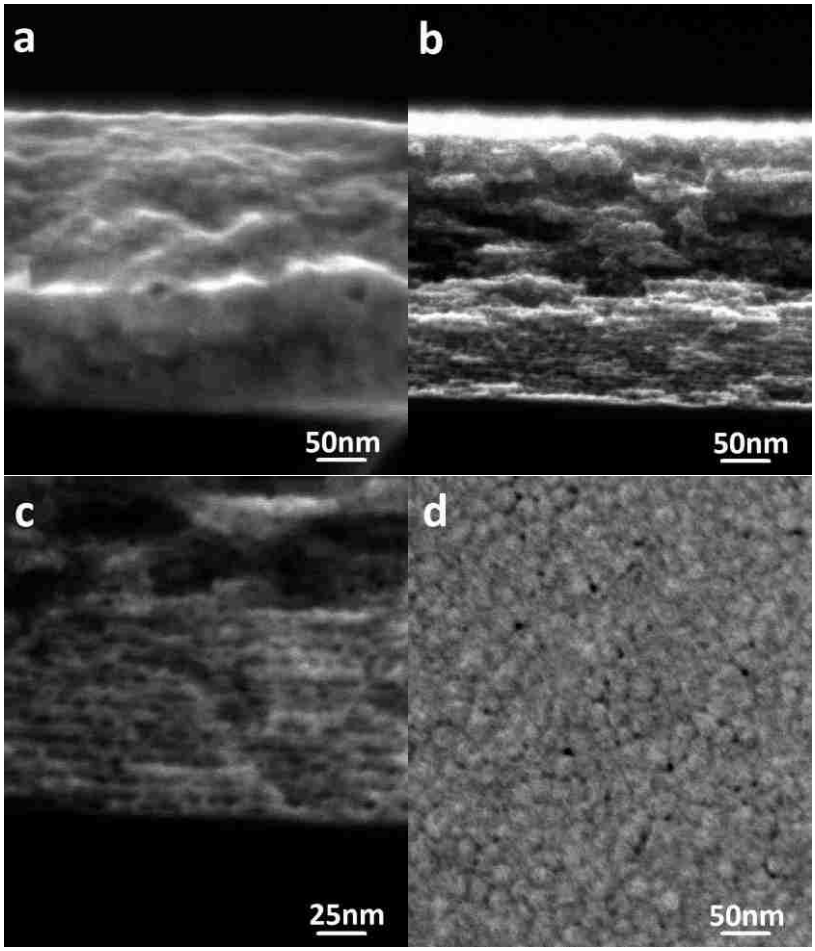

Figure 6.6. (a). Cross section SEM image of the as-deposited 300 nm Ni-Ir thin film; (b). Cross section SEM image the film after dealloying; (c). Partial cross section of the same dealloyed film; d. Surface morphology of the same film**.**

As discussed in previous section, TEM images were also obtained. Figure 6.7 shows TEM bright field image and STEM dark field image of a non-layered 35 nm np-Ir. Unsurprisingly, TEM images revealed a lot features which were not seen in SEM images. As shown in Figure 6.7b, the STEM dark field image indicated dealloyed film exhibited ligament width of less than 3 nm, which were measured to be 2.6 nm. Recalling surface morphology in SEM images, as in Figure 6.5, it exhibited porosity with ligaments of 6-7 nm. It's possible that the ligaments displayed in SEM images were actually made of even smaller sub-ligaments of 2-3 nm.

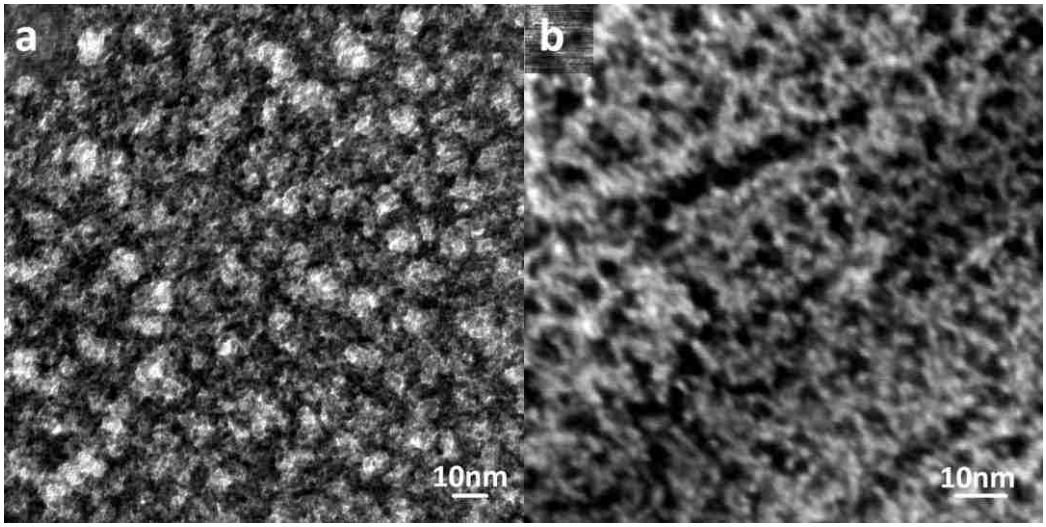

Figure 6.7. TEM images of a 35 nm uniform np-Ir film. Image (a) is a standard bright field TEM image; (b) is a dark field STEM image, it revealed a lot of details which can't be seen in SEM and bright field TEM**.**

6.4.4 Crystallography of dealloyed films

XRD scans were obtained for the dealloyed film to determine its crystal information. Similar to the NiCu precursor film, as discussed in previous chapter, the IrNi precursor film also displayed one <111> alloy peak, indicating that the precursor film was <111> oriented. After dealloying the alloy peak was gone, but none peak was showing up, same as that for np-Ni.

Due to the limited information from XRD scans, the dealloyed film was characterized in TEM by diffraction pattern as well, as shown in Figure 6.8. It's from the same np-Ir film in Figure 6.7. The diffraction pattern indicated that np-Ir film had a crystal structure with no preferred orientation. And the rings can be indexed, as shown in Figure 6.8b.

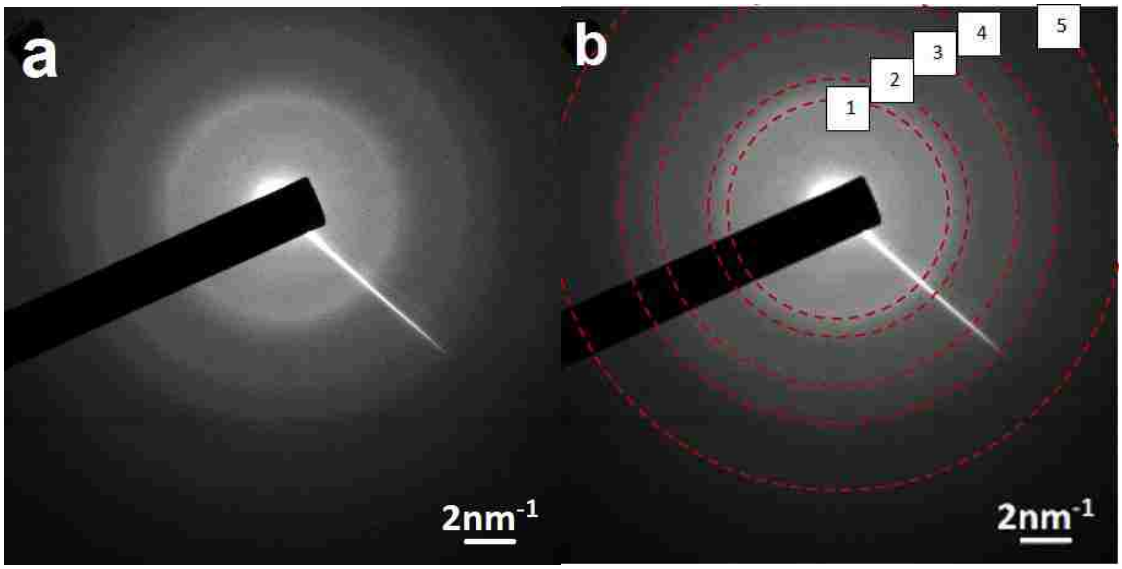

Figure 6.8. Selective area diffraction pattern of np-Ir thin film (the same film in Figure 5.7). Indexing the diffraction rings indicated the film has an isotropic fcc structure.

The method to index the diffraction pattern is presented in the following. First, 5 rings were detected in the image, as labelled 1-5 in Figure 6.8. And then the diameters of the rings were measured in Digital Micrograph (image software, Gatan, Inc.), i.e. 9.55, 11.35, 15.76, 18.66, and 23.98 nm^{-1}. In TEM,

$$Rd = \lambda L \qquad \text{Equation 6.1}$$

where R is the Radius of the diffraction spot/ring, d is the corresponding atomic spacing, λ is the electron wave length, and L is camera length. $\lambda \cdot L$ is a camera constant. Recall that d is related with lattice parameter, a, by the equation below:

$$d = \frac{a}{\sqrt{h^2+k^2+l^2}} \qquad \text{Equation 6.2}$$

h, k, l are miller indices (atomic plane indices). Thus, a relationship between R, d and $h^2 + k^2 + l^2$ can be written as,

$$\left(\frac{R_i}{R_1}\right)^2 = \left(\frac{d_1}{d_i}\right)^2 = \frac{h_i^2+k_i^2+l_i^2}{h_1^2+k_1^2+l_1^2} \qquad \text{Equation 6.3}$$

The subscript, i, is to distinguish different planes/diffraction rings. With this relationship, one can come up with the indices of the rings, as shown in Table 6.2. Considering the structure factor, the indexed planes implied a fcc crystal structure with no texture even there are some planes missing, e.g. <222>, <400>.

Table 6.2. Indices of electron diffraction pattern in Figure 6.8. The indexed planes implied a fcc crystal structure with no preferred crystal orientation.

i	D_i	R_i	$\frac{R_i}{R_1}$	$\left(\frac{R_i}{R_1}\right)^2$	$\frac{h_i^2+k_i^2+l_i^2}{h_1^2+k_1^2+l_1^2}$	$h_i^2+k_i^2+l_i^2$	<hkl>
1	9.55	4.78	1	1	$1=\frac{3}{3}$	3	<111>
2	11.35	5.68	1.19	1.41	$1.41\cong\frac{4}{3}$	4	<200>
3	15.76	7.88	1.65	2.72	$2.72\cong\frac{8}{3}$	8	<220>
4	18.66	9.33	1.95	3.82	$3.82\cong\frac{11}{3}$	11	<311>
5	23.98	11.99	2.51	6.31	$6.31\cong\frac{19}{3}$	19	<331>

6.4.5 Thermal cycling of np-Ir films

The thermal cycling curves of a 300 nm np-Ir multilayer film are displayed in Figure 6.9. Only the cooling curves are presented here. Dealloyed film experienced structure evolution during heating, complicating the correlation of stress-temperature heating segments. The cooling curves represented typical thermoplastic and elastic behavior. As the film cooled from the maximum temperature in a given cycle, it exhibited thermoelasticity, and stress increased linearly until plastic deformation begins, in the temperature range 170-220 ℃. The yield strength were taken at the transition points in each cooling cycle, as listed in Table 6.3, and they fall into a range of 337 MPa-395 MPa. The stress was affected by both the relative density and also the ligaments size effect. These

two mechanisms worked on stress in opposite ways. Increased relative density led to an increasing in film stress. While the ligaments coarsening resulted in a decreasing in film stress. As result presented shortly later, during thermal cycling, the relative density of the film was indeed increased. However, the ligaments coarsening was not evident in the SEM images. These made the discussion of yield strength become complicated. Additionally, the absolute value of stress in the np-Ir thin film is sensitive to slight shifts in wafer position, which potentially changed at the beginning of thermal cycle, due to sample replacement in the wafer curvature system. In this study, only the thermal elastic slopes were used to investigate the thermoelastic behavior of np-Ir because the errors in absolute stress do not affect the measurement of elastic slope.

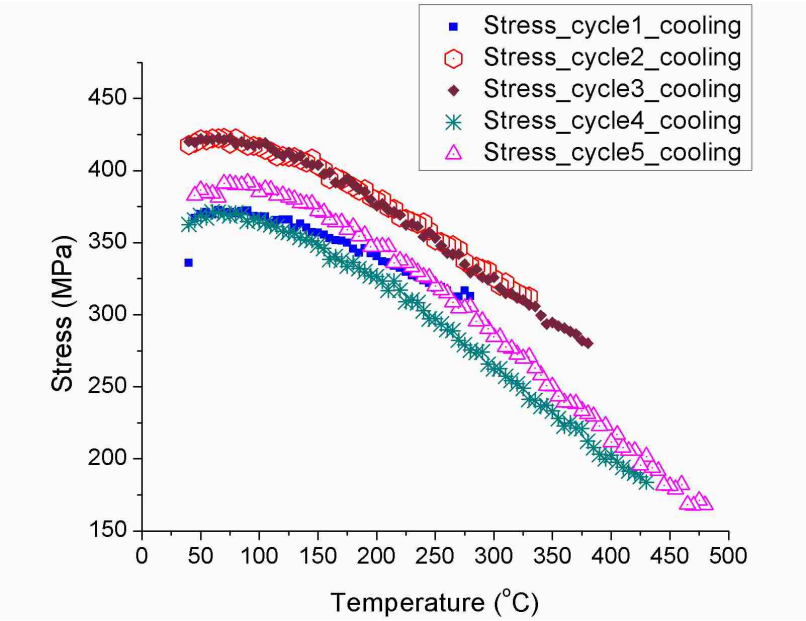

Figure 6.9. Stress vs. temperature curves of the thermal cycles. 300 nm np-Ir film went through 5 thermal cycles in a wafer curvature system. The film exhibited thermal elastic and plastic behavior at elevated temperature, and a transition from elasticity to plasticity happened during 100 ℃-200 ℃ in each cooling segment. Information about the thermal elastic slope and transition points can be found in Table 6.3.

The film thickness after each cycle can be measured from witness samples, using the cross-section images, as shown in Figure 6.10. The film underwent contraction during

thermal cycling. A summary of the thickness of the film, before and after dealloying and after each cycle, is listed in Table 6.3. The ligaments did not display obvious coarsening according to the plan view images in Figure 6.11, but it is not conclusive since the ligaments are too small to be observed in the SEM images. However, some cracks were formed in the last two cycles. Because the crack size was not significantly large, it is believed the ligaments were still connected into a 3D network.

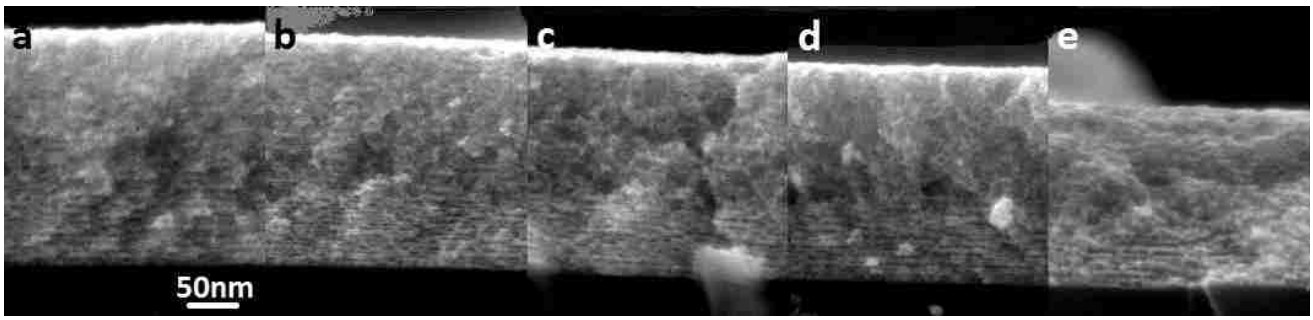

Figure 6.10. The SEM images of cross-section of the np-Ir after thermal cycles. (a), (b), (c), (d) and (e) correspond to the one after cycle 1 (from RT to 300 ℃), cycle 2 (from RT to 350 ℃), cycle 3 (from RT to 400 ℃), cycle 4 (from RT to 450 ℃) and cycle 5 (from RT to 500 ℃), respectively.

The contraction of the film indicated relative density of the np-Ir increased during/after each thermal cycle. For a np-Ir film fabricated by dealloying, its relative density is equal to the volume percentage of Ir in the precursor film. This statement is true with the assumptions that the dealloyed film kept the original thickness of the precursor film (IrNi film), and the sacrificial element, Ni, was removed completely. The thickness remained during dealloying. However, thermal cycling caused considerable thickness contraction. The purity of dealloyed films was not 100% either. The EDS measurement indicated that the dealloyed film still had 25 at.% Ni. In this study the precursor film composition is 22 at.% Ir, or 26.7 vol.% Ir. Considering the residue Ni and thickness

contraction in the film, the relative densities were calculated to 0.351 for as-dealloyed np-Ir film, gradually increased to 0.492 after 5 thermal cycles, as shown in Table 6.3.

Table 6.3. Summary of thermomechanical behavior exhibited by np-Ir during repeated thermal cycling. The biaxial elastic modulus M_s of fully dense, thin film Ir was calculated from the bulk isotropic elastic constants for Ir: E_s = 528 GPa, and ν_s = 0.26. Relative biaxial modulus was calculated as the ratio of M^*/M_s.

Sample processing history	Temp range (℃)	Yield strength (MPa)	Thermo-elastic slope (MPa/K)	M_f or M^* (MPa)	Relative biaxial modulus M^*/M_s	Thickness (nm)	Relative density ρ^*/ρ_s
as-deposited	-	-	-	-	-	310	-
as-dealloyed	-	-	-	-	-	303	0.351
Cycle 1	265-170	351	-0.394	119	0.167	263.5	0.403
Cycle 2	325-180	389	-0.539	163	0.228	253	0.420
Cycle 3	375-175	395	-0.557	169	0.236	245	0.434
Cycle 4	425-180	336	-0.628	190	0.266	233.5	0.455
Cycle 5	475-220	337	-0.687	208	0.291	216	0.492

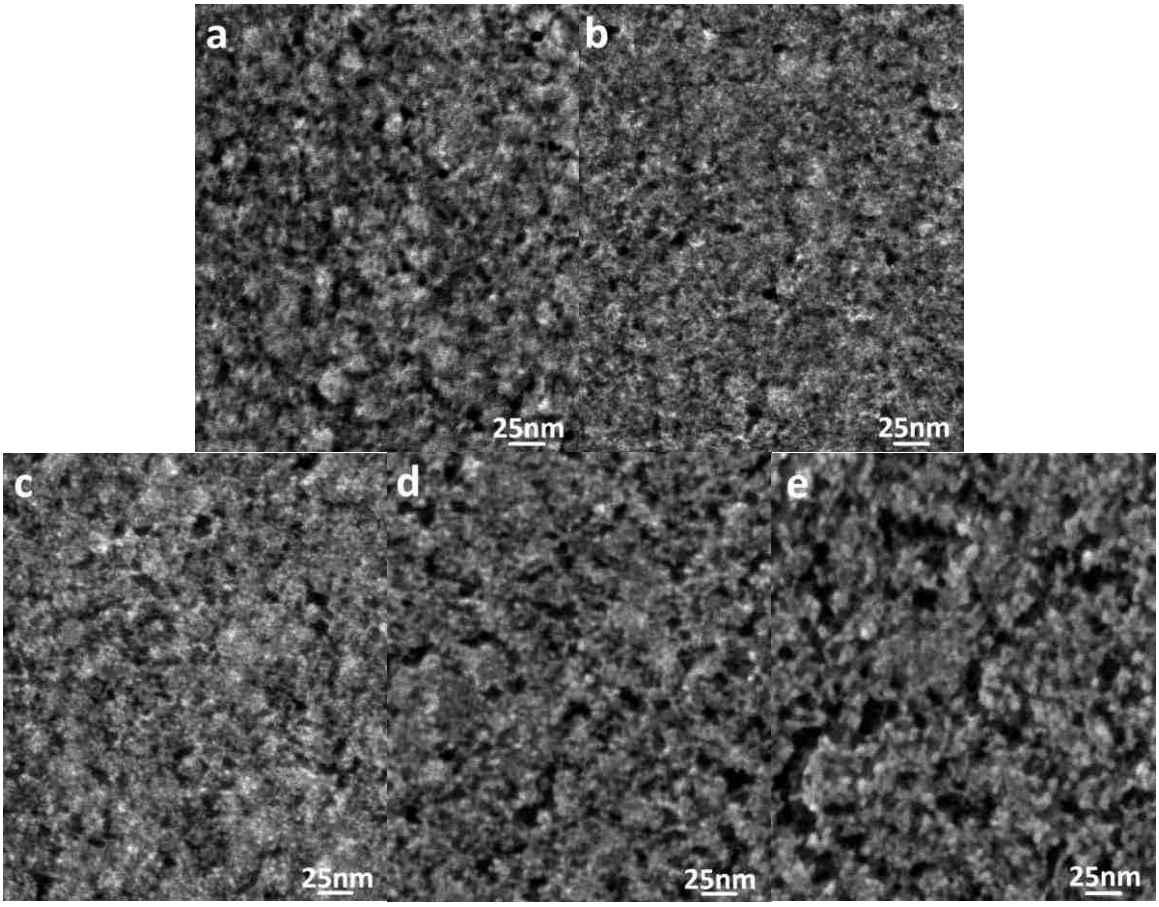

Figure 6.11. Surface morphology SEM images of the np-Ir after thermal cycles. (a), (b), (c), (d) and (e) correspond to the one after cycle 1 (from RT to 300 ℃), cycle 2 (from RT to 350 ℃), cycle 3 (from RT to 400 ℃), cycle 4 (from RT to 450 ℃) and cycle 5 (from RT to 500 ℃), respectively.

The thermoelastic slopes were measured from each cooling segment, as listed in Table 6.3. The thermoelastic slope is related to the film's biaxial modulus by the following equation, Equation 6.4 [58], which is same as Equation 3.3,

$$\frac{\Delta\sigma_f(T)}{\Delta T} = (\alpha_s - \alpha_f) \cdot M_f \qquad \text{Equation 6.4}$$

Where α_s and α_f are thermal expansion coefficients for substrate, Si, and film, Ir, respectively, with α_s =3.5e-6 K^{-1} [92] and α_f =6.8e-6 /K^{-1} [93, 94]. $\Delta\sigma_f(T)/\Delta T$ is the slope of the thermal elastic curve. The calculated biaxial moduli of the np-Ir film, M_f (or M^* in Equation 6.7), during each cooling cycle are also listed in Table 6.3.

6.4.6 Experimentally determined scaling behavior of elastic modulus

As discussed in Chapter 2.4, according to Gibson and Ashby's scaling law, the ratio of Young's moduli of porous material to that of the ligaments material is related to its relative density by a power-law equation, as shown in Equation 6.5 [53].

$$\frac{E^*}{E_s} = C_1\left(\frac{\rho^*}{\rho_s}\right)^n \qquad \text{Equation 6.5}$$

where E^* and E_s are Young's moduli of the porous material, and its corresponding cell wall material, respectively, and E^*/E_s is also called relative Young's modulus. ρ^*/ρ_s is the relative density of the porous material. C_1 and n are empirical constants. For low relative density (ρ^*/ρ_s<0.1), open cell foams, n=2, and C_1 is highly related to the geometry of porosity. The empirical data show that C_1=1 [53].

For an isotropic material, the biaxial modulus is related to its Young's modulus by the reciprocal of $(1-\nu)$, ν is Poisson's ratio, as show in Equation 6.6.

$$M = \frac{E}{1-\nu} \qquad \text{Equation 6.6}$$

Apply Equation 6.6 to Equation 6.5, a similar relationship can be written for relative biaxial modulus, as shown in in Equation 6.7.

$$\frac{M^*}{M_s} = C_2\left(\frac{\rho^*}{\rho_s}\right)^n \qquad \text{Equation 6.7}$$

where M^* and M_s are biaxial moduli of the porous material, i.e. np-Ir film (same as M_f in Equation 6.4), and its corresponding ligaments materials, i.e. dense Ir. M_s is taken as 714 GPa, which is for isotropic Ir. The TEM diffraction pattern indicated that the dealloyed Ir films did not have preferred orientation, as shown in Figure 6.8. A natural logarithm form of Equation 6.7 is written as,

$$ln\frac{M^*}{M_s} = n \cdot ln\left(\frac{\rho^*}{\rho_s}\right) + lnC_2 \qquad \text{Equation 6.8}$$

The relationship of the coefficients, C_2 and C_1, can also be by obtained by applying Equation 6.6 to Equation 6.5, and it gives,

$$C_2 = C_1 \frac{1-\upsilon_s}{1-\upsilon^*} \qquad \text{Equation 6.9}$$

where v^* and v_s are Poisson's ratios of porous materials and the ligaments materials, respectively. For Ir, v_s=0.26 [95]. Gibson and Ashby determined C_1=1 based on empirical data. Therefore, the Poisson's ratio of np-Ir, ν^*, can be calculated after obtaining C_2.

The thermal cycling of np-Ir film generated film of multiple relative densities. The corresponding biaxial modulus at each particular relative density was also available from the cooling curves. Thus the exponent, n, and coefficient, C_2, in Equation 6.7 can be determined by linear fitting relative biaxial moduli and relative densities in a nature log scale. As a result, the fitting line is shown in Figure 6.12. It's seen that n=1.60, and C_2=0.92.

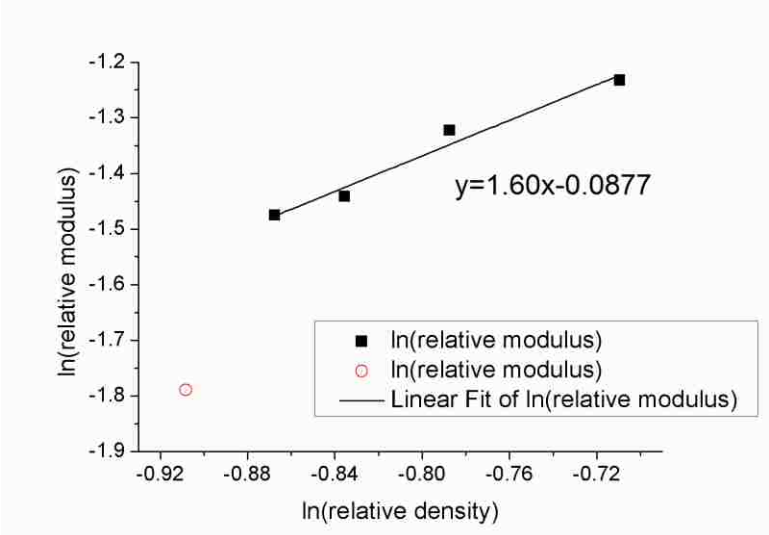

Figure 6.12. Plot of the relative biaxial moduli and relative densities in log-log scale. The red circle data point is from cycle 1, and it's not included in the fitting due to a big deviation from other points.

6.4.7 Derivation of scaling equation for nanoporous metals

Gibson and Ashby determined the exponent of the power equation to be 2, according to their cubic unit cell model [53]. Their model was built for low relative density ($\rho^*/\rho_s<0.1$) cellular materials. It is not the case for most of the nanoporous metal fabricated from dealloying. The relative density of the np-Ir in the experiments is in the range of 0.3-0.5, and most of the nanoporous gold have relative density of 0.2-0.4 [17], which are much larger than 0.1. To further understand the meaning of the exponent in the scaling equation, the Gibson and Ashby's cubic model is reviewed.

The original model used in Gibson and Ashby's calculation, consisted of beams of length l and square cross-section of side t was applied to simulate nanoporous metal as well. The model was slightly modified, containing 24 beams as in Figure 6.13, instead of 12 beams in the original one. For convenience, the beam length, l, is taken from the midpoints of the nodes, where two beams adjoined. It is the same way measuring the ligament length of np-metals.

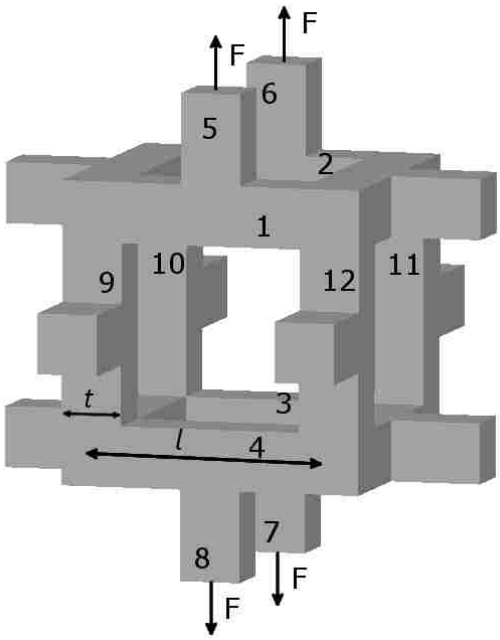

Figure 6.13. Cubic unit cell model for nanoporous metals. The unit cell is made of 24 beams: 12 long beams and 12 short beams. The beam length, l, is taken from midpoints of corresponding nodes. And each beam has a square cross-section of width *t*.

The relative density, ρ^*/ρ_s can be calculated by ratio of beam volume to unit cell volume. The volume of all the beams is a sum of each one. First, the short beams extended from the middle of cubic edges are considered. There are 12 of those beams, and each of them has a length of $(l-t)/2$. Thus their volume is $12 * t^2 * (l-t)/2 = 6(l-t)t^2$. Then considering the beams that form the cubic region that in the center of the unit cell. For these beams, three of them share one node at the vertices. We calculate their volume by two parts. First, 8 nodes at the corners, and each of them has a volume of t^3. Second, the remaining part contains 12 beams with length of $(l-t)$, and each has a volume of $(l-t)t^2$. By adding all the beams and nodes, the volume of beams is $V_{beams} = 6(l-t)t^2 + 12(l-t)t^2 + 8t^3 = 18lt^2 - 10t^3$.

Volume of the unit cell is straightforward to calculate, i.e. a cubic with edge of $2l$ long. Therefore, $V_{unit\ cell} = 8l^3$. As a result, the relative density of a unit cell is written as,

$$\frac{\boldsymbol{\rho^*}}{\boldsymbol{\rho_s}} = \frac{V_{beams}}{V_{unit\ cell}} = \frac{\mathbf{18}\boldsymbol{lt^2}-\mathbf{10}\boldsymbol{t^3}}{\mathbf{8}\boldsymbol{l^3}} \qquad \text{Equation 6.10}$$

When $t \ll l$, i.e. low relative density, indicated as the red sold circles in Figure 6.14, the relative density is proportional to t^2/l^2 according to Equation 6.10, as determined by Gibson and Ashby. However, this square relationship is no long applicable to higher relative density porous materials. The relative density ρ^*/ρ_s is plotted out versus t/l, as shown in Figure 6.14.

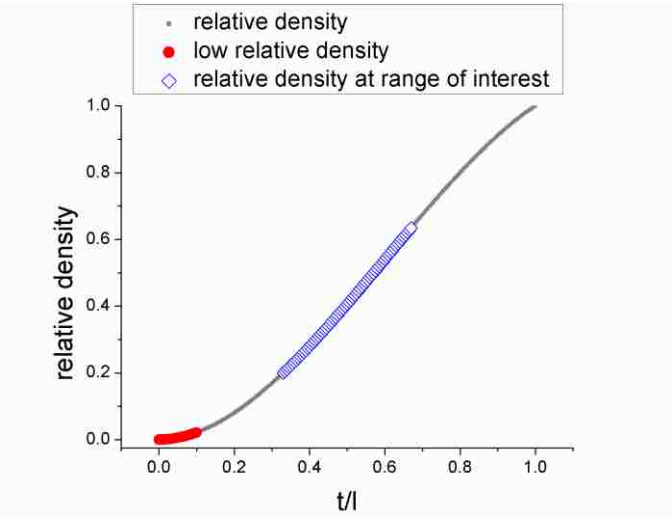

Figure 6.14. Plot of relative density versus the ratio of ligament width to length, t/l. The solid red circles correspond to points in the low-density (less than 0.02) range. The blue diamonds represent the relevant range of t/l ratio for nanoporous metals, where $0.33 < t/l < 0.67$ and aspect ratio ranges from 1.5 to 3.

Note that t/l is actually reciprocal of ligament aspect ratio, i.e. the ratio of ligaments length to width. Based on the previous study of np metals, np-metals usually have aspect ratios of 1.5-3, corresponding to t/l in the range of 0.33-0.67, i.e. the region of blue open diamond in Figure 6.14. In this range, the curve didn't display the same power of '2' trend as those in the beginning. ρ^*/ρ_s can be fitted into a power-law equation to t/l as well, but the exponent is 1.60, as shown in Equation 6.11.

$$\frac{\boldsymbol{\rho^*}}{\boldsymbol{\rho_s}} = \boldsymbol{C_3}\left(\frac{\boldsymbol{t}}{\boldsymbol{l}}\right)^{\mathbf{1.60}} \qquad \text{Equation 6.11}$$

Relative modulus was also reviewed with the unit cell shown in Figure 6.13. In Gibson and Ashby's original cubic model, they neglected the beam extension or compression and only considered beam bending induced foam deformation. It has been widely accepted that the linear elastic deformation is primarily caused by cell-wall bending for low density open-cell foams. However, as relative density increases (ρ^*/ρ_s>0.1), the contribution of extension or compression becomes more significant. Here Deformation in a tensile test was considered. Beam bending and extension as well were calculated for the unit cell shown in Figure 6.13. The unit cell is subjected to four tensile forces, *F*, in vertical direction, and beams 1-4 are therefore bent convexly. Besides that, beams 5-8 and 9-12 are accordingly be stretched. In the following, we will discussion the deformation of them in vertical direction individually.

Beam 5-8, having length of $(l - t)/2$, experience uniaxial tensile stress of F/t^2, and the strain on each of them is,

$$\boldsymbol{\varepsilon_{5,6,7,8}} = \frac{\boldsymbol{F}}{\boldsymbol{E_s t^2}} \qquad \text{Equation 6.12}$$

where E_s is the young's modulus of the beam material (ligament material).

Beam 9-12, having length of $(l + t)$, experience a tensile stress of $F/2t^2$. There are also some bending caused by the tensile force, but the bending deflection is negligible. The tensile strain on each of them is,

$$\boldsymbol{\varepsilon_{9,10,11,12}} = \frac{\boldsymbol{F}}{\boldsymbol{2E_s t^2}} \qquad \text{Equation 6.13}$$

Beam 1-4, having length of $(l - t)$, experience bending induced by a midpoint load. Since we neglected the bending of beam 9-12, beam 1-4 are considered as fixed ended. The bending deflection due to a midpoint load F is,

$$\boldsymbol{\delta_{1,2,3,4}} = \frac{\boldsymbol{F(l-t)^3}}{\boldsymbol{192E_sI}} \qquad \text{Equation 6.14}$$

where I is the moment of inertia. For a square cross section beam, $I = 1/12 * t^4$. Therefore,

$$\boldsymbol{\delta_{1,2,3,4}} = \frac{\boldsymbol{F(l-t)^3}}{\boldsymbol{16E_st^4}} \qquad \text{Equation 6.15}$$

The other beams in the unit cell contribute little to overall deformation. And the deformation of the unit cell is calculated by adding all the deformation in vertical direction, i.e. bending of beam 1- 4 and tension of beam 5-12, as written in Equation 6.16,

$$\Delta = \boldsymbol{2\varepsilon_{5,6,7,8}} \cdot \frac{\boldsymbol{(l-t)}}{\boldsymbol{2}} + \boldsymbol{\varepsilon_{9,10,11,12}} \cdot \boldsymbol{(l+t)} + \boldsymbol{2\delta_{1,2,3,4}} \qquad \text{Equation 6.16}$$

Substitute Equations 6.13, 6.14, 6.15 into Equation 6.16, the deformation of the unit cell is,

$$\Delta = \frac{\boldsymbol{F}}{\boldsymbol{E_s}}\left[\frac{\boldsymbol{(l-t)^3}}{\boldsymbol{8t^4}} + \frac{\boldsymbol{3l-t}}{\boldsymbol{2t^2}}\right] \qquad \text{Equation 6.17}$$

The unit cell is under a stress σ^* of $2F/(2l)^2$, and the corresponding strain ε^* is $\Delta/2l$. Therefore the Young's modulus of the unit cell can be calculated, as shown in Equation 6.18.

$$\boldsymbol{E^*} = \frac{\boldsymbol{\sigma^*}}{\boldsymbol{\varepsilon^*}} = \frac{\boldsymbol{F}}{\boldsymbol{l \cdot \Delta}} \qquad \text{Equation 6.18}$$

Substitute Equation 6.17 into the equation above, and it yields the relative Young's modulus, E^*/E_s, as written in Equation 6.19.

$$\frac{\boldsymbol{E^*}}{\boldsymbol{E_s}} = \frac{\boldsymbol{8t^4}}{\boldsymbol{l(l^3-3l^2t+15lt^2-5t^3)}} \qquad \text{Equation 6.19}$$

As what we did for the relative density, E^*/E_s is also plotted out to t/l, as shown in Figure 6.15.

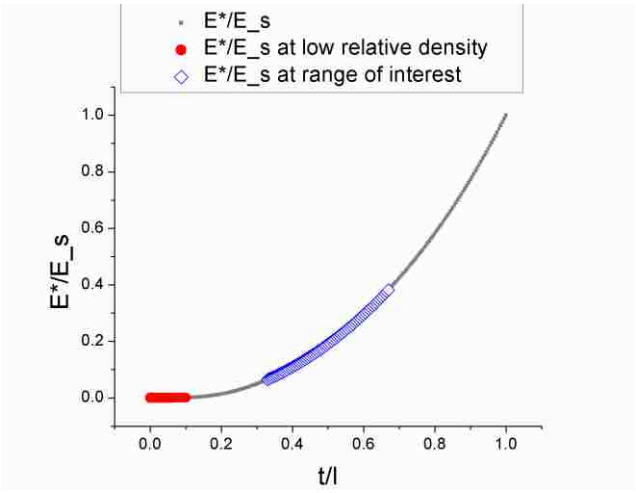

Figure 6.15. Plot of relative modulus, E^*/E_s, versus the ratio of ligament width to length, t/l. The red circles and blue diamonds represent the same t/l ranges as in Figure 6.14.

The curve is evaluated by fitting with power equations as well. Note that in the entire range 0< t/l <1, E^*/E_s varied also from 0 to 1. For t/l=0, it represents a unit cell made of vacuum, and apparently E^* is 0; and for t/l=1, it represents a unit cell filled with ligament materials, and E^* is identical to E_s in this case. In the entire relative density range, the power equation fitting is,

$$\frac{E^*}{E_s} = \left(\frac{t}{l}\right)^{2.4} \qquad \text{Equation 6.20}$$

This fitting has a coefficient of determination, R^2, of 0.996. It indicates the data is fitted well. However, for the range for nanoporous metals, i.e. 0.33<t/l<0.67, it comes up with slightly different coefficients,

$$\frac{E^*}{E_s} = 1.01\left(\frac{t}{l}\right)^{2.43} \qquad \text{Equation 6.21}$$

Apply Equation 6.11 to Equation 6.21, one can get a relationship of relative Young's modulus to relative density in 0.33<t/l<0.67,

$$\frac{E^*}{E_s} = C_4\left(\frac{\rho^*}{\rho_s}\right)^{1.52} \qquad \text{Equation 6.22}$$

As described in the previous chapter, the relationship of relative biaxial modulus to relative density has the same exponent as that of Young's modulus. Thus the power equation above is applicable for relative biaxial modulus except the prefix coefficient is different.

The discussion above is for t/l in the range of 0.33-0.67, corresponding to aspect ratios of 1.5-3. However, in study of np metals, it is not always easy to get the aspect ratio. Fujita and Chen took the 3-D morphology of np-gold in a high-angle TEM, and measured the aspect ratio as 2-3 [21]. For most of researchers, measuring from 2-D SEM or TEM micrographs was the only available access. The drawback of measuring from 2-D morphology is that it underestimates the ligaments length because the projection in 2D is usually shorter than the actually length. For example, in the previous study on np-gold we measured np-gold ligaments based on plan-view 2-D SEM micrographs, and got an aspect ratio of about 1.3 [96]. And for the np-Ir in this study, the ligaments measurement of dark field STEM images implied that the aspect ratio is about 1.9. On the other hand, sometimes the relative density is easier to measure than aspect ratio for np metals. For np metals fabricated by dealloying, the relative density is the volume fraction of the metal in the precursor alloy, e.g. the volume percentage of Ir in IrNi precursor alloy, and Au in AuAg precursor alloy. The above statement is true only if the sacrificial element is removed completely and also the volume of the sample stays the same during dealloying. The actual dealloying usually involved some volume contraction and the sacrificial elements may remain a little. However, with some correction the relative density can still be derived from the volume fraction relatively easily. Due to this, the scaling behavior of elastic modulus is also reported in term of relative density. The relative density of np-Au usually drops in

the range of 0.3-0.35. For np-Ir in this study, the as-dealloyed the film has a relative density close to 0.35, but due to volume contraction in thermal cycling the relative density increased gradually to 0.5. The scaling equations for relative density in the ranges of 0.28-035, 0.35-0.40, 0.40-0.45 and 0.45-0.50, are listed in Table 6.4.

Table 6.4. Calculated relationships between relative modulus, relative density and ligament aspect ratio for various ranges of relative density.

$\frac{\rho^*}{\rho_s}$	$\frac{\rho^*}{\rho_s}$ vs $\frac{t}{l}$	$\frac{E^*}{E_s}$ vs $\frac{t}{l}$	$\frac{E^*}{E_s}$ vs $\frac{\rho^*}{\rho_s}$
0.28-0.35	$\frac{\rho^*}{\rho_s} = 1.32\left(\frac{t}{l}\right)^{1.69}$	$\frac{E^*}{E_s} = 1.11\left(\frac{t}{l}\right)^{2.54}$	$\frac{E^*}{E_s} = 0.84\left(\frac{\rho^*}{\rho_s}\right)^{1.50}$
0.35-0.40	$\frac{\rho^*}{\rho_s} = 1.26\left(\frac{t}{l}\right)^{1.64}$	$\frac{E^*}{E_s} = 1.04\left(\frac{t}{l}\right)^{2.45}$	$\frac{E^*}{E_s} = 0.82\left(\frac{\rho^*}{\rho_s}\right)^{1.49}$
0.40-0.45	$\frac{\rho^*}{\rho_s} = 1.23\left(\frac{t}{l}\right)^{1.60}$	$\frac{E^*}{E_s} = 1.01\left(\frac{t}{l}\right)^{2.41}$	$\frac{E^*}{E_s} = 0.82\left(\frac{\rho^*}{\rho_s}\right)^{1.51}$
0.45-0.50	$\frac{\rho^*}{\rho_s} = 1.20\left(\frac{t}{l}\right)^{1.55}$	$\frac{E^*}{E_s} = 1.00\left(\frac{t}{l}\right)^{2.38}$	$\frac{E^*}{E_s} = 0.83\left(\frac{\rho^*}{\rho_s}\right)^{1.54}$

Using the same method, the scaling equation in the relative density range 0.42-0.49, corresponding to np-Ir film in previous thermal cycling experiment, can also be determined:

$$\frac{E^*}{E_s} = \mathbf{0.83}\left(\frac{\rho^*}{\rho_s}\right)^{\mathbf{1.52}} \qquad \text{Equation 6.23}$$

6.4.8 Modification of the modeling determined scaling equation by using a revised unit cell

One problem with the model presented here is the real ligaments commonly have non-uniform cross-section. As seen in Figure 6.4 and 6.5, the nodes where two or more

ligaments meet are thicker than middle of the ligaments. To address this problem, the unit cell is modified by add fillets at nodes.

The revised unit cell, based on Figure 6.13, was created by adding fillets at nodes of the np structure, as shown in Figure 6.16. Each fillet is represented by a prism with an isosceles right triangle cross section (fillet/prism length equal to ligament width). For this unit cell with fillets at nodes, the bending deflection and ligament extension in the axial direction must be recalculated.

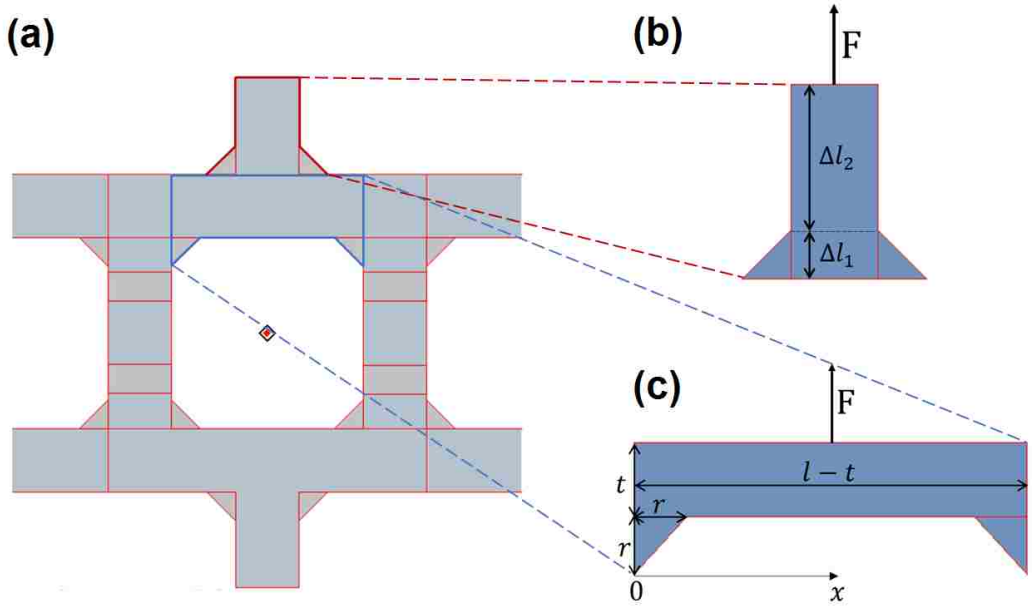

Figure 6.16. Schematic drawing of a revised unit cell with fillets added at nodes (modification of the original unit cell from Fig 5.13). (a) Front view of the unit cell with added fillets. (b) Enlarged view of beam 5 (numbering as in Fig. 5.13). (c) Enlarged view of beam 1, excluding the node.

The bending deflection δ is written as,

$$\boldsymbol{\delta = 2\int_0^{\frac{l-t}{2}} \frac{M(x)m(x)}{E_s I(x)}\, dx} \qquad \text{Equation 6.24}$$

where M(x) is the bending moment at position *x* due to the applied load. For beams 1-4 (beam labeling as in Fig. 5.13) with force F applied at the ligament midpoint, M(x) can be written as,

$$\boldsymbol{M(x) = \frac{F(4x-l+t)}{8}} \qquad \text{Equation 6.25}$$

Furthermore, m(x) is the bending moment at position *x* due to the applied unit load.

$$\boldsymbol{m(x) = \frac{4x-l+t}{8}} \qquad \text{Equation 6.26}$$

I(x) is the moment of inertia for each beam (1-4). Due to variation in the beam's cross-sectional area along the x-direction, as shown in Figure 6.16c, the integral must be solved by separation into two parts:

$$\boldsymbol{\delta_{1,2,3,4} = 2\int_0^r \frac{M(x)m(x)}{E_s I(x)}dx + 2\int_r^{\frac{l-t}{2}} \frac{M(x)m(x)}{E_s I(x)}dx} \qquad \text{Equation 6.27}$$

For $0 \leq x \leq r$, $I(x) = t \cdot (t + r - x)^3/12$, and for $r \leq x \leq (l - t)/2$, $I(x) = t^4/12$. Combining Equations 6.25 and 6.26 with Equation 6.27 above, the result of this integration is,

$$\boldsymbol{\delta_{1,2,3,4} = \frac{3F}{8E_s \cdot t}\left[16 \cdot ln\frac{t+r}{t} - \frac{32r+40t-8l}{t} + \frac{(l-5t-4r)^2}{2t^2} + \frac{40t+32r-8l}{r+t} - \frac{(l-5t-4r)^2}{2(r+t)^2} + \frac{(l-t)^3-(4r-l+t)^3}{12t^4}\right]} \qquad \text{Equation 6.28}$$

The elongation due to tensile load F on beams 5-8 must be recalculated as well, and is also considered in two parts, as shown in Figure 6.16b. First, for the ligament portion with varying cross section, the extension Δl_1 is calculated by integration:

$$\boldsymbol{\Delta l_1 = \int_0^r \frac{F}{E_s A(x)}dx} \qquad \text{Equation 6.29}$$

where *A(x)* is the cross-sectional area of the beam. For $0 \leq x \leq r$, $A(x) = t(t + 2x)$. The result of this integration is,

$$\Delta \boldsymbol{l_1} = \frac{\boldsymbol{F}}{\boldsymbol{2E_s t}} \boldsymbol{ln}\left(\frac{\boldsymbol{t+2r}}{\boldsymbol{t}}\right) \qquad \text{Equation 6.30}$$

Second, the extension of the remainder of the beam, Δl_2, is,

$$\Delta \boldsymbol{l_2} = \boldsymbol{\varepsilon_{5,6,7,8}} \cdot \left(\frac{\boldsymbol{l-t}}{\boldsymbol{2}} - \boldsymbol{r}\right) = \frac{\boldsymbol{F(l-t-2r)}}{\boldsymbol{2E_s t^2}} \qquad \text{Equation 6.31}$$

Therefore, the total extension of each beam (5-8), Δl, is,

$$\Delta \boldsymbol{l_{5,6,7,8}} = \Delta \boldsymbol{l_1} + \Delta \boldsymbol{l_2} = \frac{\boldsymbol{F}}{\boldsymbol{2E_s t}} \left(\boldsymbol{ln}\left(\frac{\boldsymbol{t+2r}}{\boldsymbol{t}}\right) + \frac{\boldsymbol{l-t-2r}}{\boldsymbol{t}}\right) \qquad \text{Equation 6.32}$$

For beams 9-12, the extension remains the same as for the original model depicted in Figure 6.13, and is written as,

$$\Delta \boldsymbol{l_{9,10,11,12}} = \boldsymbol{\varepsilon_{9,10,11,12}} \cdot (\boldsymbol{l} + \boldsymbol{t}) = \frac{\boldsymbol{F(l+t)}}{\boldsymbol{2E_s t^2}} \qquad \text{Equation 6.33}$$

As a result, the total deformation Δ of the unit cell consists of the midpoint deflection of beams 1-4, the tensile elongation of beams 5-8, and the tensile elongation of beams 9-12,

$$\Delta = \boldsymbol{2\delta_{1,2,3,4}} + \boldsymbol{2\Delta l_{5,6,7,8}} + \Delta \boldsymbol{l_{9,10,11,12}} \qquad \text{Equation 6.34}$$

Combining Equations 6.28, 6.32, and 6.33 with Equation 6.34 above, deformation Δ can be written as,

$$\Delta = \frac{\boldsymbol{F}}{\boldsymbol{E_s \cdot t}} \left[\boldsymbol{12\, ln}\frac{\boldsymbol{t+r}}{\boldsymbol{t}} + \boldsymbol{ln}\left(\frac{\boldsymbol{t+2r}}{\boldsymbol{t}}\right) + \frac{\boldsymbol{50l-52r-61t}}{\boldsymbol{2t}} + \frac{\boldsymbol{3(l-5t-4r)^2}}{\boldsymbol{8t^2}} + \frac{\boldsymbol{30t+24r-6l}}{\boldsymbol{r+t}} - \frac{\boldsymbol{3(l-5t-4r)^2}}{\boldsymbol{8(r+t)^2}} + \frac{\boldsymbol{(l-t)^3-(4r-l+t)^3}}{\boldsymbol{16t^3}}\right] \qquad \text{Equation 6.35}$$

The relative Young's modulus, E^*/E_s, is obtained by substituting Equation 6.35 into Equation 6.18,

$$\frac{E^*}{E_s} = \frac{1}{\frac{l}{t}\left[12\,ln\frac{t+r}{t} + ln\left(\frac{t+2r}{t}\right) + \frac{50l-52r-61t}{2t} + \frac{3(l-5t-4r)^2}{8t^2} + \frac{30t+24r-6l}{r+t} - \frac{3(l-5t-4r)^2}{8(r+t)^2} + \frac{(l-t)^3-(4r-l+t)^3}{16t^3}\right]}$$

Equation 6.36

To analyze and simplify Equation 6.36 above, *r*, *t* and l were evaluated to determine if a general fixed relationship exists between them. Due to the difficulty in determining ligament size of np-Ir from SEM or TEM images, fillet size and ligament width were measured for a typical np-Au structure, shown in Figure 6.17. It is assumed here that np-Ir ligaments have the same curvature as np-Au ligaments, which exhibit an average fillet-size-to-ligament-width ratio of $r = t/3$. Substituting this value into Equation 6.36 yields a simplified expression for relative modulus:

$$\frac{E^*}{E_s} = \frac{t^4}{0.125l^4 - 0.46l^3t + 2.13l^2t^2 - 0.98lt^3}$$

Equation 6.37

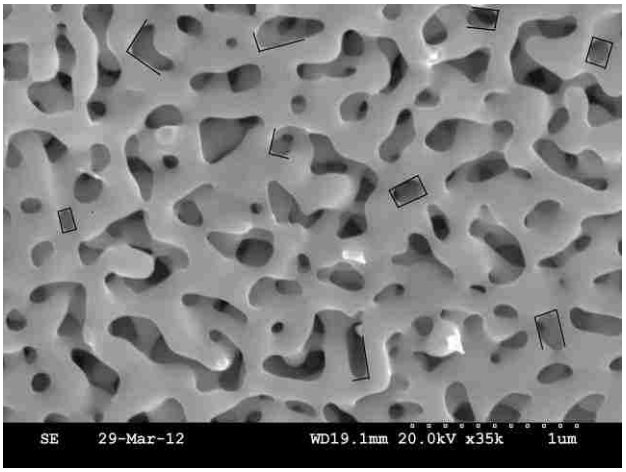

Figure 6.17. Plan view SEM image of np-Au fabricated by the author's group. Most ligaments exhibit thickening at the nodes, which are represented in the revised structural model by fillets with isosceles right triangle cross section. Some of the fillets/nodes analyzed in this np-Au structure are indicated by black lines superimposed on the micrograph. The average ligament width *t* and fillet size *r* are measured as 118 nm and 37 nm, respectively.

In addition, relative density ρ^*/ρ_s was recalculated after adding fillets at the nodes. Adding the volume of all fillets to V_{beam} in Equation 6.10, the revised relative density was

obtained. Each fillet has a volume of $r^2t/2$, and there are 48 fillets. Relative density thus becomes,

$$\frac{\rho^*}{\rho_s} = \frac{V_{beams}}{V_{unit\ cell}} = \frac{18lt^2 - 10t^3 + 24r^2t}{8l^3} \quad \text{Equation 6.38}$$

Similar to the evaluation of Equations 6.10 and 6.19 in previous section, the relationships between ρ^*/ρ_s, E^*/E_s and t/l represented by Equations 6.37 and 6.38 were plotted as well. Over the relative density range relevant for np metals, $0.42 < \rho^*/\rho_s < 0.49$, the following relationships were obtained:

$$\frac{\rho^*}{\rho_s} = \mathbf{1.50}\left(\frac{t}{l}\right)^{\mathbf{1.74}} \quad \text{Equation 6.39}$$

$$\frac{E^*}{E_s} = \mathbf{1.13}\left(\frac{t}{l}\right)^{\mathbf{2.46}} \quad \text{Equation 6.40}$$

Combining these two equations yields the revised scaling equation:

$$\frac{E^*}{E_s} = \mathbf{0.75}\left(\frac{\rho^*}{\rho_s}\right)^{\mathbf{1.42}} \quad \text{Equation 6.41}$$

The same set of calculations was also performed for different fillet sizes, resulting in the scaling equations summarized in Table 6.5. A smaller fillet size slightly changes the scaling exponent (this ranges from 1.45-1.49). Moreover, the scaling equation trends toward that for the original model (Equation 6.23) as fillet size decreases. This makes sense because, as fillet size r approaches zero, the filleted structure returns to the original unit cell model.

It is noted that the revised model, with fillets at nodes, loses physical meaning as t/l approaches unity. Equations 6.37 and 6.38 suggest values of relative density ρ^*/ρ_s and relative modulus E^*/E_s larger than 1 for t/l=1. This is, of course, physically impossible. When fillets are added at nodes, the relationship $l - t > 2r$ must be met, to ensure that filleted ligament regions fit between nodes, as seen in Figure 6.16. To satisfy this constraint,

t/l < 0.6 must hold for ligaments with r = t/3 (and t/l < 0.75 for r = t/6). Therefore, Equation 6.37 and 6.38 cannot be used to describe the scaling relationship between relative density and relative modulus for t/l ratios beyond this range.

Table 6.5. New scaling equations calculated for the revised unit cell with fillets at nodes. Different ratios of fillet size to ligament width were considered, for the same relative density range of 0.42-0.49.

$\frac{r}{t}$	$\frac{\rho^*}{\rho_s}$ vs $\frac{t}{l}$	$\frac{E^*}{E_s}$ vs $\frac{t}{l}$	$\frac{E^*}{E_s}$ vs $\frac{\rho^*}{\rho_s}$
1/3	$\frac{\rho^*}{\rho_s} = 1.50\left(\frac{t}{l}\right)^{1.74}$	$\frac{E^*}{E_s} = 1.13\left(\frac{t}{l}\right)^{2.47}$	$\frac{E^*}{E_s} = 0.75\left(\frac{\rho^*}{\rho_s}\right)^{1.42}$
1/4	$\frac{\rho^*}{\rho_s} = 1.38\left(\frac{t}{l}\right)^{1.64}$	$\frac{E^*}{E_s} = 1.08\left(\frac{t}{l}\right)^{2.45}$	$\frac{E^*}{E_s} = 0.78\left(\frac{\rho^*}{\rho_s}\right)^{1.45}$
1/5	$\frac{\rho^*}{\rho_s} = 1.31\left(\frac{t}{l}\right)^{1.64}$	$\frac{E^*}{E_s} = 1.05\left(\frac{t}{l}\right)^{2.42}$	$\frac{E^*}{E_s} = 0.80\left(\frac{\rho^*}{\rho_s}\right)^{1.48}$
1/6	$\frac{\rho^*}{\rho_s} = 1.28\left(\frac{t}{l}\right)^{1.62}$	$\frac{E^*}{E_s} = 1.00\left(\frac{t}{l}\right)^{2.41}$	$\frac{E^*}{E_s} = 0.81\left(\frac{\rho^*}{\rho_s}\right)^{1.49}$

6.4.9 Discussion of the modeling determined scaling equations

Now recall the scaling equation determined from thermal cycles. The exponent derived from the model, 1.52 (or 1.42 from the revised model), agreed well with the one obtained in thermal cycling experimental measurement, 1.60. Since the two methods are completely independent, these results confirmed the reliability of both measurement. Roberts and Garboczi also studied the scaling behavior by finite element method [97]. They simulated the elastic behavior of random open-cell porous metals using a node-bond model, and found that the scaling exponent ranged between 1.29-1.81. All of these indicated an exponent less than 2. Therefore, Gibson-Ashby framework must be reconsidered in order to properly describe the scaling behavior of nanoporous metals.

The structural model considered here could be further improved, but would require a significant modeling effort. One potential shortcoming of the unit cell in Figure 6.13 is the representation of ligaments as beams with square and non-varying cross section. Actual nanoporous structures have ligaments with circular cross section, and diameter can vary along the length of the ligament (in addition to thickening at nodes). It is, however, not clear that such modeling efforts would result in more accurate scaling equations. On the other hand, relatively simple models similar to that considered in this paper have been used by others to evaluate the scaling behavior of nanoporous materials. Feng et al. [98] employed the same model that is considered here and evaluated surface effects on elastic modulus of nanoporous materials. Antoniou et al. [99] used a rectangular unit cell, with cubic fillets added at nodes, to estimate the actual nanoporous structure of metal foams. However, their model did not predict a functional dependence of relative elastic modulus on relative density, nor did their composite plot of experimental data for nanoporous metals. This could be due to fitting their model over a wide range of relative densities, since scaling behavior itself appears to change when relative density is very low, very high, or intermediate (e.g. the range considered here for np metals).

The model described in the previous section 6.4.7, based on a unit cell without fillets (as shown in Figure 6.13), has two advantages over the traditional Gibson and Ashby model in regard to np metals. First, beam deformation due to tension/compression is considered in this model. Based on microstructural observations of np-Au samples that ruptured in bending or tension [100, 101], ligaments at the fracture surface experienced significant elongation and necking due to local tensile stress. This suggests that tensile/compressive deformation provides some contribution to overall deformation and

therefore should not be neglected. Second, the model used here allows evaluation of scaling behavior over the entire t/l range (0-1) without predicting physically impossible scenarios such as relative density greater than unity at high t/l ratio, a situation predicted by the models that include fillets at nodes. Equation 6.10 and Equation 6.19 can describe the relationships between ρ^*/ρ_s, E^*/E_s and t/l for porous materials of either low relative density or high relative density. Moreover, at the extreme ends of the t/l range (0 and 1), Equations 6.10 and 6.19 each predict relative density and relative modulus of 0 and 1, representing empty space and fully dense material, respectively, which are physically realistic scenarios.

6.5 Conclusions and future work

The following conclusions were made for this project:

1) Np-Ir thin films were fabricated by free corrosion of Ir-Mg and electrochemical dealloying of Ir-Ni precursors. Both precursor alloys yielded nanoporous structure with fine ligament as small as 5 nm and high purity.
2) In addition to the non-layered np-Ir, multilayer np-Ir was also fabricated by dealloying multilayer IrNi precursors. Dealloying multilayer IrNi film used a two-step procedure, including free corrosion and electrochemical dealloying.
3) The thermomechanical behavior of np-Ir was investigated by thermal cycling of multilayer np-Ir films. Biaxial elastic moduli for np-Ir with different values of relative density were obtained from sequential individual thermal cycles, and these were used to determine the elastic scaling behavior of np-Ir. An updated scaling equation, with an exponent of 1.60, was determined for this nanoporous system.

This result differed significantly from the standard Gibson-Ashby model for materials with macroscale porosity.

4) A power-law equation describing scaling behavior of elastic behavior was derived for relative density range of nanoporous metals (0.28-0.50), by revisiting Gibson and Ashby's unit cell model. An exponent of 1.52 was determined by modeling, which agreed very well with the experimental results.

In regard to further work, more efforts can be made in improving the model established here. As discussed in section 6.4.9, the ligaments in a real np metallic structure don't have square cross-section, and neither the cross-section is uniform. And also the nodes where ligaments meet are usually thicker than middle of the ligament. Even the author addressed this problem by adding fillets at nodes, real ligaments still exhibit more complicated geometry than that. In order to narrow the differences between modelling to real geometry, significant amount of computational work is required.

On the other hand, even though this present model predicted the scaling behavior of elastic modulus determined from thermal cycling of np-Ir thin films, it should be applied to other np metal systems as well, such as thermal cycling of np-Au or np-Pd.

Scaling behavior of strength should also be determined by using this current model. However, one distinct thing is that when evaluating elastic modulus both bending and uniaxial extension/compression were considered, since both them contribute to the total deformation of the unit cell (in Figure 6.13). But for strength, such as yield strength and fracture stress, the mechanism which plays the critical role is the only factor needs to be considered. For example, when a tensile force applied to the unit cell in Figure 5.13, the cell will deform. Some of the ligaments experience uniaxial tensile, while others undergo

bending deformation. The stress on each ligament is different in both type and magnitude. Once one ligament break, the whole unit cell will fail. The stress resulting in this failure can be caused by bending or tension. And therefore it has to be determined which mode causes the failure before trying to establish the scaling equation for strength.

7 Bulk np-Ir fabrication and study of mechanical behavior of bulk np-Ir

7.1 Introduction

Unlike other fcc metals, Ir is reported to be very 'brittle' in bulk form. Bulk Ir undergoes brittle cleavage after some plastic deformation in tensile test. Researchers have an argument on the origin of this brittleness. Some researchers contributed it to an extrinsic reason, mainly impurities in the grain boundary [102]. While others believed it is an intrinsic property of Ir [103-105].

Additionally, some brittle materials, like Si, have been discovered some ductile behavior in nanoscale mechanical test. One example is compression test of Si pillars. Fredrik Ostlund et al. found a brittle-to-ductile transition in the compression test when they decreased the Si pillar diameter from 1 μm to 300 nm [106]. The maximum engineering strain can reach 22% in the test, which is surprisingly high, especially considering the very brittle nature of Si. Another example is the work in the author's group. In the study of np-Si, it exhibited a sponge-like behavior in in-situ nanoindentation test. The thickness of the np-Si thin film was almost fully recovered after the indenter removed from the film [Jessie's paper, unpublished]. The maximum deformation in thickness was up to 33%. Even this number is not an actual strain because the ligaments subjected to different amount of deformation, and also different types of deformation (most of the ligament were bent rather than compressed under indenter), but the result is as impressive as the previous example of compression test on Si pillars.

On the other hand, it was reported that ligaments in np-Au exhibited extraordinary high yield strength [14, 15, 55]. Size effect was founded in np-Au when the ligament size decreasing from ~100 nm to ~10 nm. Will the ligaments in np-Ir, which have a typical size

of less than 5nm, also display high yield strength, and how was size effect working for np-Ir? Will the ligaments in np-Ir perform plastic or brittle deformation during tension and compression tests? These question will be answered in this study. And it is believed that this study will help further understanding the deformation mechanism of Ir in nanometer scale.

This research work was supported by NSF CAREER grant as well.

7.2 Challenges and methodology

Some potential challenges existed in this study, including:

1. Preparation of bulk np-Ir is difficult. First, due to the brittle nature of Ir, bulk np-Ir may subject to cracking and even pulverization. Second, dealloying polycrystal bulk IrNi is even more challenging due to the vulnerable grain boundary to cracks. Moreover, as discussed in chapter 6.4.1, electrodealloying of IrNi had to be performed at a potential up to 1.2-1.3 V due to passivation of Ni under this voltage. This voltage is so high to etch most kinds of metals (e.g., stainless steel). The container or carrier of bulk sample has to be carefully selected to avoid being etched in dealloying.
2. Dealloying thin film IrNi was already time-consuming as indicated in Table 6.1. Dealloying bulk IrNi was expected to take days even weeks.

Both IrNi and IrMg thin films yielded np-Ir with nice nanoporous structure. However, IrNi was selected as the precursor alloy to prepare bulk np-Ir due to very limited volume contraction in dealloying of IrNi thin films.

IrNi precursor alloy was prepared by arc melting mixed pure Ir and pure Ni pellets. With previous experience in dealloying bulk gold silver (Au-Ag) samples, a two-step dealloying procedure was planned used here to dealloy bulk IrNi as well.

Mechanical behavior of bulk np-Ir was studied by nanoindentation and micro compression test (didn't be able to carry out) due to the ease access to nanoindentation system and micro specimen test system. Nanoindentation has been widely used to study mechanical behavior of np-Au, which can easily measure yield strength of the sample. However, previous study in author's group found that yield strength measured from indentation differed from that directly measured from tensile test by an order of its magnitude [16]. Mechanical properties of bulk np-Ir would be evaluated by both indentation and compression test for comparison.

7.3 Experimental

7.3.1 Vacuum arc melting

Bulk Ir-Ni sample was created by vacuum arc melting from Professor David Johnson in Purdue University. Pure Ir (99.9%) lumps and Ni (99.98%) wires were cut and weighed to prepare alloy of various composition, i.e. 13.5, 15, 18, 20 at% Ir. The samples were melt with flowing in mixture of Ar and H_2 (5%), and each sample was flipped 5 times to improve homogeneity. The base pressure was at 65 mtorr, and the chamber was purged 3 times before final melting.

7.3.2 Sample preparation before dealloying

The arc melted sample had to be cut into proper shape before performing future experiments. Depending on the requirements of mechanical tests, different sample geometry and dimension would be used. Samples for nanoindentation were nothing special, but had to be flat. Otherwise, undesirable non-equilateral indenter prints would be produced after indentation. The samples were first cut by a diamond saw (Isomet, Buehler) into a disc shape with thickness of ~1 mm. To make sample flat, the sample were then grind and polished on both side by using disc grinder (Gatan). In addition to make the sample flat, it is important to make the two surfaces parallel as well. It was achieved by mounting the sample with little crystal bond, and before crystal bond becoming rigid, the sample with holder was pressed upside town on a flat surface.

7.3.3 Dealloying

Dealloying of bulk IrNi sample were conducted in nitric acid as well. Both free corrosion and electrochemical dealloying were exploited to establish the best way to create bulk np-Ir. Generally, dealloying bulk IrNi started at a very slow rate to avoid formation of cracks on the grain boundary. A diluted nitric acid solution (1 acid : 3 H_2O) was used in the first step with no heating or agitation. The weight was recorded every 24 hours to monitor progress of dealloying. After one or two days, a slightly stronger acid solution (1 acid: 2 H_2O) replaced the solution in step one. And so on, 1:1 diluted was used in the next step. After these, electrochemical dealloying was conducted on the sample by applying a constant potential of 1.2 V. The setup was similar to that in Figure 6.1, and sample was placed in a stainless steel mesh, and immersed in a 1:4 diluted nitric acid electrolyte. The

dealloying in this step was monitored by current reading in an ampere meter. However, stainless steel was etched as well when subjected to 1.2 V potential. Indeed, as dealloying going, sample surface became more and more Ir rich, which became an undesirable protection layer. Instead, etching of stainless steel became relatively easier. Therefore, a galvanization couple formed on the working electrode, and Ir alloy was protected by the stainless steel from being further dealloyed. Other containers to hold the bulk sample were also tried out, such as Au coated kapton, Ir coated kapton, and even a Au mesh. However, none of these worked out, and they all acted as the sacrificial component when coupled with bulk IrNi sample.

Due to the unsuccessful dealloying by applying potential, bulk IrNi were dealloyed merely by free corrosion. The following procedure is for an 18 at.% IrNi precursor sample. The beginning step (step 1) was still in 1:3 diluted nitric acid, with no heating or agitation. After one day, the solution was slightly heated to 35 ℃ and dealloying was held for two days. And then heating was increased to 50 ℃, and this step (step 3) was kept for 50 hours. The stronger solution (1:1 diluted nitric acid) was used in step 4, and dealloying were performed for 232.5 hours with heating at 50 ℃. The next step (step 5) was conducted in even stronger acid (2:1 diluted nitric acid) for 337 hours with heating at 50 ℃.

7.3.4 Nanoindentation

Nanoindentation was performed to dealloyed bulk sample in a Micro Materials Nanoindenter. Measurements were run in load control mode, and maximum loads of 1 mN, 3 mN, 5 mN, 8 mN, 12 mN and 15 mN were used. To improve the reliability of

measurement, test in each load was repeated for 25 times. A loading and unloading rate of 0.025mN/s was used all the cycles.

7.3.5 Characterization

Morphology of dealloyed bulk IrNi sample was characterized by both optical microscope (BX41, Olympus) and SEM (S900 and S3200, Hitachi). Optical microscope was convenient and quick to check cracks after and during each step of dealloying. Additionally, electron microscope was used to measure the indenter print size after nanoindentation.

7.4 Results and discussion

7.4.1 Dealloying of bulk IrNi

Small IrNi pieces of each composition were dealloyed according to the procedure in Table 7.1. As discussed in section 7.3.3, electrochemical dealloying was not exploited. Dealloying of 13.5 at.% precursor alloy was not accomplished due to pulverization on sample surface. It was suspected having too much sacrificial element (Ni), in precursor alloy. Dealloying of sample with 15 at% and higher Ir content can be finished with heating and agitation, but for a fairly long time. And a lot of cracks were formed in the dealloyed samples. Dealloying 18 at. % Ir sample was not finished either, but it was on purpose to avoid further cracking.

Table 7.1. List of the fabrication and dealloying conditions for synthesizing np-Ir from bulk Ir-Ni samples of 13.5-20 at.% Ir.

Precursor alloy[1]	13.5 at.% Ir	15 at.% Ir	20 at.% Ir	18 at.% Ir
Original weight	0.0430 g	0.0262 g	0.0409 g	0.0239 g
Original composition[2]	15.9 at.% Ir 38.2 wt.% Ir	16.7 at% Ir 39.6 wt.% Ir	24.5 at% Ir 51.5 wt.% Ir	21.3 at.% Ir 47.0 wt.% Ir
Dealloying procedure	1. 1:1, 50 ℃, agitation, 61.5 h. 2. Conc., 50 ℃, agitation, 71 h.	1. 1:1, 50 ℃, no stirring, 42.5 h. 2. 3:1, 50 ℃, no stirring, 7 h. 3. 3:1, 50 ℃, agitation, 55 h. 4. Conc., 50 ℃, agitation, 154 h. 5. Conc., 70 ℃, agitation, 78 h.	1. 1:3, RT, no stirring, 22 h. 2. 1:1, RT, no stirring, 119 h. 3. 1:1, 50 ℃, no stirring, 5.5 h. 4. 1:1, 50 ℃, agitation, 47.5 h. 5. 2:1, 50 ℃, agitation, 93 h. 6. Conc., 30 ℃, no stirring, 5 h. 7. Conc., 50 ℃, no stirring, 24 h. 8. Conc., 50 ℃, stirring, 233 h. 9. Conc., 70 ℃, stirring, 96.5 h.	1. 1:3, RT, no stirring, 27.5 h. 2. 1:3, 35 ℃, no stirring, 45 h. 3. 1:3, 50 ℃, no stirring, 50 h. 4. 1:1, 50 ℃, no stirring, 236.5 h. 5. 2:1, 50 ℃, no stirring, 337 h.
Final weight	0.0297 g	0.0114 g	0.0243 g	0.0162 g
Final composition[3]	27.4 at.% Ir 55.2 wt.% Ir	76.0 at.% Ir 91.2 wt.% Ir	68.1 at.% Ir 87.5 wt.% Ir	40.2 at.% Ir 68.8 wt.% Ir

[1] Composition in this row was calculated based on mass of each element prepared for arc melting.

[2] Composition in this row was measured from EDS.

[3] Composition in this row was calculated based on final weight in row 6 and original composition in row 3 (assuming that only Ni was removed in dealloying).

7.4.2 Morphology of dealloyed film

Dealloyed samples suffered serious cracking, as shown in optimal micrographs in Figure 7.1. Figure 7.1a shows plan-view image of the undealloyed bulk sample (18 at.% Ir) in Table 7.1. Figure 7.1b-f corresponds to plan-view images after each dealloying step for this sample. Cracks formed in dealloying step 4 (Figure 7.1e), in diluted 1:1 nitric acid and heating at 50 ℃. It was suspected that agitation of the etchant would initialize or speed up cracking. However, it had been tested out not being the main reason causing cracking sine in dealloying of this sample no agitation of etchant was applied. Most of the cracks started from grain boundaries, as in Figure 7.1e. With further dealloying, some transgranular cracks were also formed in grains, as in Figure 7.1 d. Therefore, to avoid cracking, single crystal may have to be used as precursors.

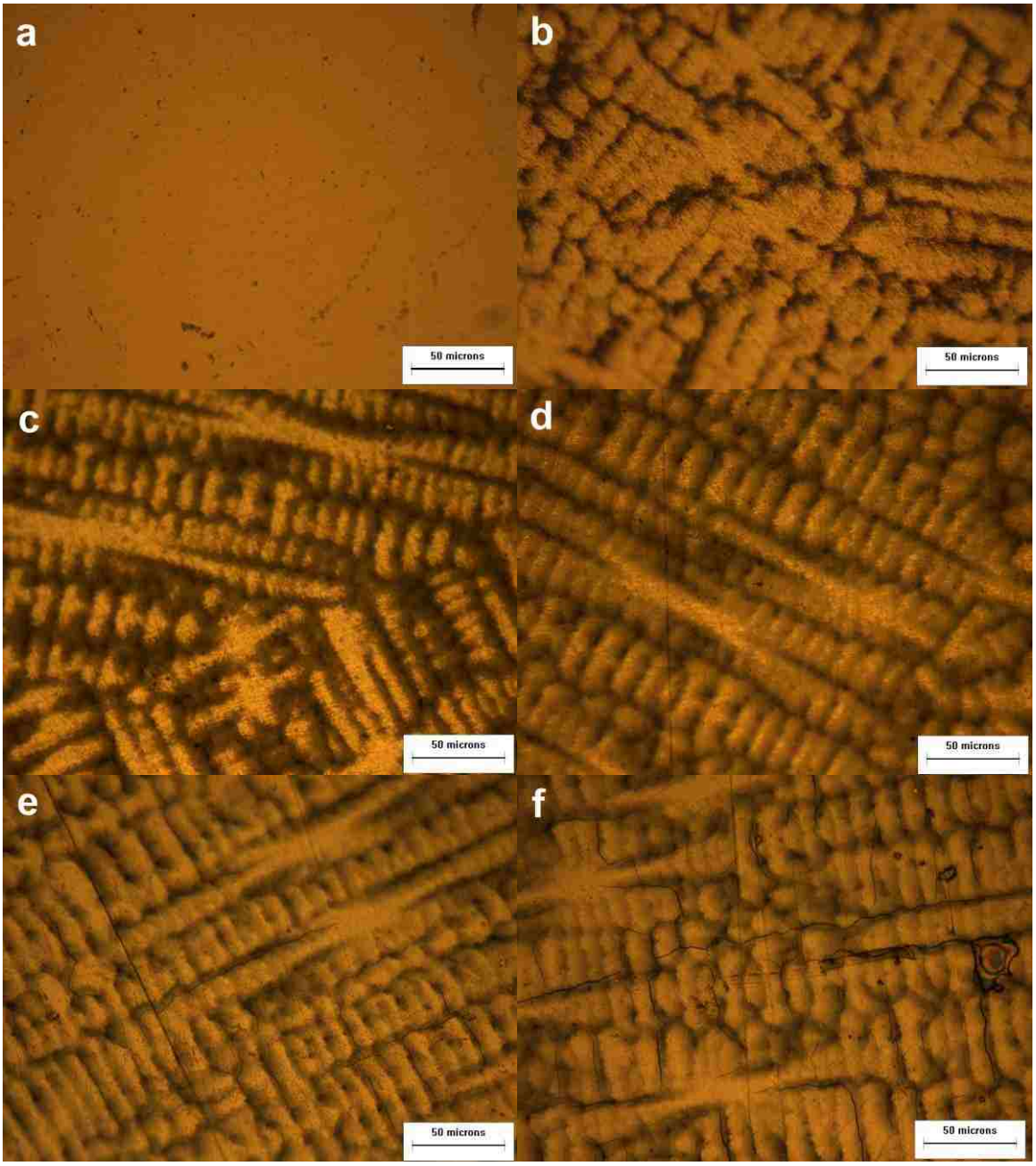

Figure 7.1. Surface morphologies of bulk IrNi (18 at.%Ir in precursor alloy) before (a) and after each dealloying step (b-f). The images were taken under optical microscopy. Cracks were formed after step 4, in diluted 1:1 nitric acid and heating at 50 ℃.

Dealloyed bulk IrNi were also observed in SEM, as displayed in Figure 7.2. Images (a) and (b) are np-Ir created by dealloying of 13.5 at.% Ir and 18 at.% Ir respectively. Even both samples still had considerable Ni, as indicated in Table 7.1, surface of the

samples was already purely nanoporous structure. And EDS measurement on these sample also proved that the surface layer (several micrometer) had Ir content up to 80 at.%. Dealloyed sample exhibited different ligament size. Nanoporous structure in Figure 7.2a exhibited ligaments as small as ~2-3 nm, whereas ligaments in Figure 7.2b are ~5-7 nm. This is likely due to the extended dealloying in the sample of 18 at.% Ir. Nanoporous Ir on the top surface layer was formed at the very beginning of dealloying stage, but it was still kept in the etchant, which caused ligament coarsening, as discussed in previous chapter 4.4.2. Sample in image (b) underwent 3 times longer dealloying time than that in image (a).

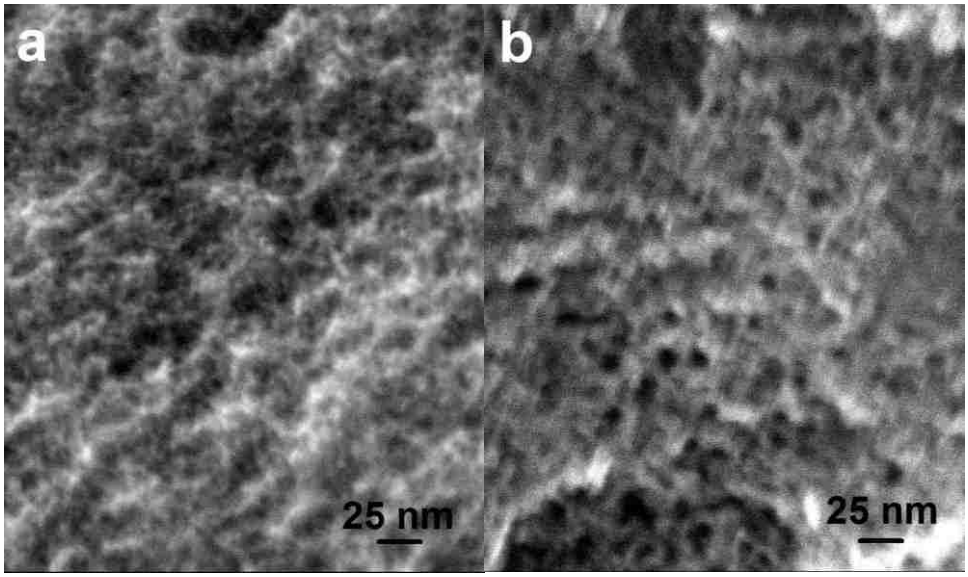

Figure 7.2. Surface morphology of bulk np-Ir, by dealloying 13.5 at.% Ir and 18 at.% Ir, respectively in (a) and (b).

7.4.3 Nanoindentation of bulk np-Ir

Even hardness can be obtained directly from the nanoindentation system, indenter prints were still observed in SEM in order to get more accurate results. Figure 7.3 shows 5 indenter prints on the 18 at.% Ir sample in Table 7.1. Due to the shape of a Berkovich tip, the indenter print displayed a triangle geometry. If the sample surface was horizontally flat,

the triangle impression should be an equilateral one. If not, it indicated uneven stress on the sample surface, and the depth measurement on the loading and unloading curve was therefore inaccurate. The prints, which were close to equilateral as in Figure 7.3, were selected to perform further calculation. Some prints were equilateral, but were close to cracks or right on cracks, and were not selected to calculate hardness either. Area of the prints were measured in Image J, and then hardness was calculated for each load. The results are listed in Table 7.2.

Table 7.2. Summary of measured indenter print size and hardness at each load.

Load (mN)	Average indenter print area (μm^2)	Hardness (MPa)
1 mN	1.48	674
3 mN	2.34	1282
5 mN	5.78	865
8 mN	6.78	1180
12 mN	7.10	1690
15 mN	7.17	2092

The calculated hardness is in the range of 674 – 2092 MPa. The hardness roughly tended to increase with higher load, which is opposite of the indenter size effect, i.e. the increase of indentation hardness with the decrease of the indentation depth. Instead, the increase of hardness is very likely caused by the effects of undealloyed IrNi sublayer. Indeed, the dealloying of this sample was not accomplished, as indicated in Table 7.1. Therefore, the discussion of hardness was developed based on the measurement at the lowest load 1 mN.

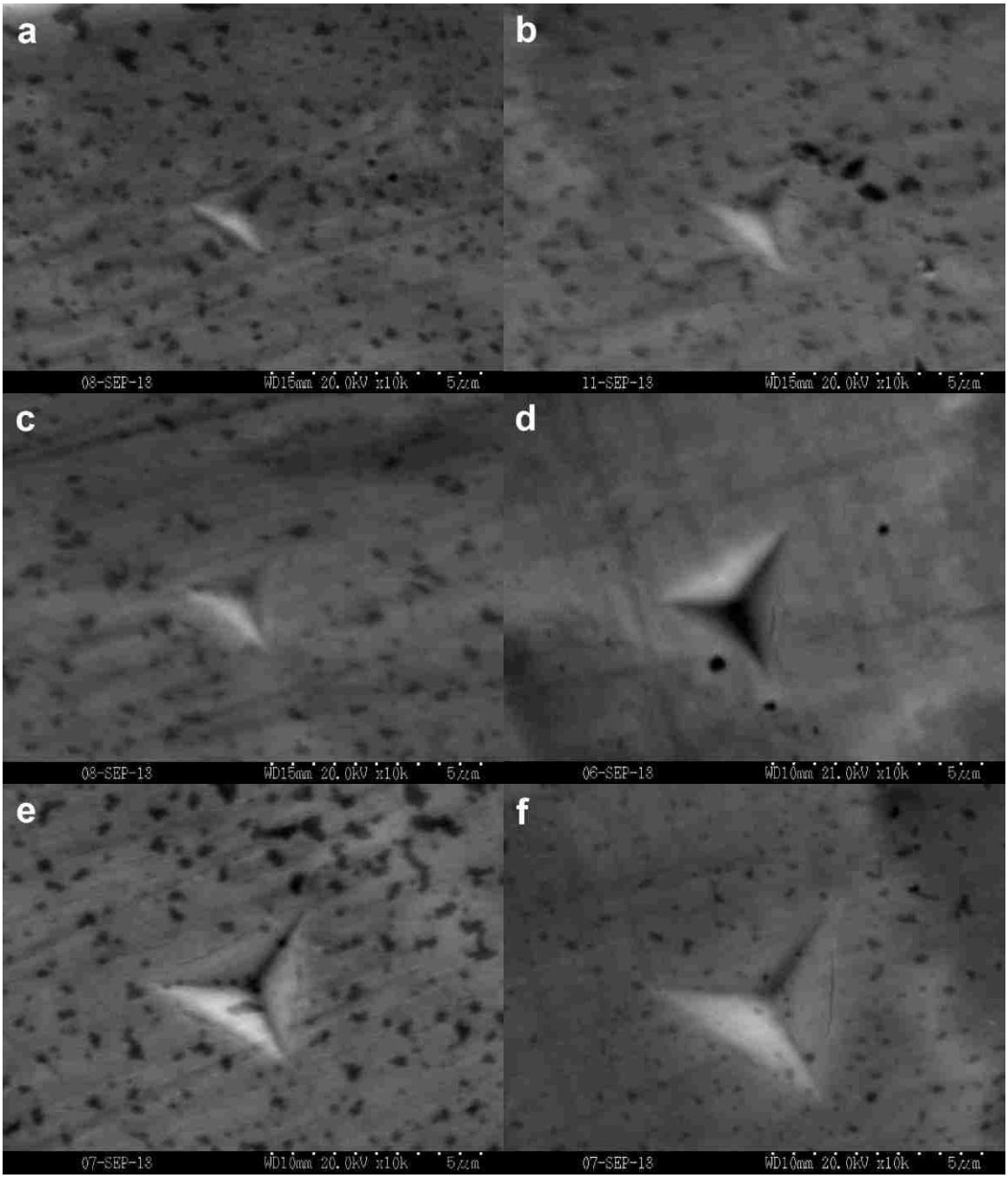

Figure 7.3. Indentation prints on np-Ir dealloyed from 18 at.% Ir precursor (dealloying condition is in fifth column of Table 7.1. Images (a-f) correspond to ones of maximum load of 1 mN, 3 mN, 5 mN, 8 mN, 12 mN, and 15 mN, respectively.

7.4.4 Using scaling equation to evaluate the measured hardness

Hardness of a material, H, is related to its yield strength, σ_y, by a relation as shown in Equation 7 [107],

$$\sigma_y = \frac{H}{3}(B)^n \qquad \text{Equation 7.1}$$

Where n is strain hardening coefficient, B is a materials constant, for aluminum and steel sample, $B = 0.1$.

However, for cellular materials, many believed hardness is equal to the yield strength, because Poisson's ratio of cellular materials, v^*, is believed as '0'. This relationship had been accepted widely in studying mechanical properties of np metals [15, 55, 108]. However, recent studies by Balk et al. [101] suggested Poisson's ratio of np metals is actually nonnegligible. They found v^* of np-Au is around 0.2. According to Shaw and Sata's study [109], hardness is related to yield stress of materials by Poisson's ratio. And for v^*=0.2, $H = 2.65\sigma$. The author's own study on np-Ir film also found a Poisson's ratio close to 0.3 [23]. It corresponds a relation of $H \cong 3\sigma$. Applying the hardness of np-Ir to this equation (H^*=674MPa according to Table 7.2 for maximum load of 1 mN). Therefore, yield strength of np-Ir σ^*= 225 MPa.

As the scaling equation for elastic modulus (Equation 6.5), the yield strength of porous materials, σ^*, is also related to that of their corresponding dense materials (or ligament materials), σ_s, by a power equation,

$$\frac{\sigma^*}{\sigma_s} = C\left(\frac{\rho^*}{\rho_s}\right)^n \qquad \text{Equation 7.2}$$

where, ρ^*/ρ_s is relative density of the material, and C and n are empirical constants. Different from the parameters in Equation 6.5, Gibson and Ashby predicted C=0.3, and

n=1.5 for yield strength. Relative density of np-Ir was calculated based on the precursor alloy composition (21.3 at.% Ir, 25.9 vol.% Ir). Assuming surface layer (down to several μm) was fully dealloyed and no volume contraction in dealloying, relative density of np-Ir is 0.26. Applying these known parameters into Equation 7.2, and then yield strength of dense Ir, σ_s, is calculated as 5.6 GPa.

One problem associated with the calculation above is that Gibson and Ashby's prediction of C=0.3 and n=1.5 was based on low relative density materials. As discussed in Chapter 6, relative density of np metals is usually in the range of 0.2-0.4, which is not considerable as low relative density.

Scaling relationship for yield strength had also been studied by Briot et al. based on the mechanical test on np-Au [16]. In their study, they also considered size effect to the stress. The coefficient and exponent are different from those predicted by Gibson and Ashby either, as shown in Equation 7.3.

$$\sigma^* = C[\sigma_0 + (k \cdot L^m)]\left(\frac{\rho^*}{\rho_s}\right)^n \qquad \text{Equation 7.3}$$

where σ_0 is the average yield strength of single crystal material, i.e. Au in their study. k *and* m are the size effect parameters, and are equal to 0.075 and -0.55 for np-Au. L is the ligament width with unit of meter. The part in the square bracket is actually yield strength of ligament materials, σ_s, and it is expressed in the format of Hall-Petch type equation due to ligament size effect. The parameters C and n were determined as 0.65 and 2.35 respectively. With this updated scaling equation, σ_s, or $\sigma_0 + (k \cdot L^m)$, is calculated to be 8.6 GPa.

Take out the Hall-Petch equation separately, it gives,

$$\sigma_y = \sigma_0 + k \cdot L^m \qquad \text{Equation 7.4}$$

σ_y is the same as σ_s, and σ_0 for Ir is taken as 50 MPa [110], m is taken the same as that for np-Au, -0.55. The coefficient, k, for np-Ir with ligament size ~6 nm, is determined as 0.17 if taking 5.6 GPa for σ_s, or 0.26 if taking 8.6 GPa for σ_s.

Theoretical yield strength of Ir is ~33 GPa ($\sigma_{th} = \frac{G}{2\pi}$, G is shear modulus, G_{Ir} = 210 GPa [111]). The calculated np-Ir ligament yield strength (5.6 GPa or 8.6 GPa) is very high, but still one order lower than theoretical yield strength. When comparing this yield strength with those of np-Au, the ratio of σ_y/G (same as σ_s/G) was considered. As shown in the Figure 7.4, results from nanoindentation [15, 55] and pillar micro-compression tests [14] of np-Au are included, indicated as open and black solid circles. σ_y/G was plotted vs. L/a, where L is ligament width, and a is lattice parameter. Nanoindentation of np-Au data were corrected by multiplying 0.38, because the original data were obtained by equaling hardness and yield strength, with the assumption that Poisson's ratio of np metal is '0'. However, as discussed earlier, Poisson's ratio of np-Au is not 0, and the yield strength of np-metal (np-Au) was about 1/3 of the hardness value measured by nanoindentation [16]. The red solid circles are the corrected data from those of open circles.

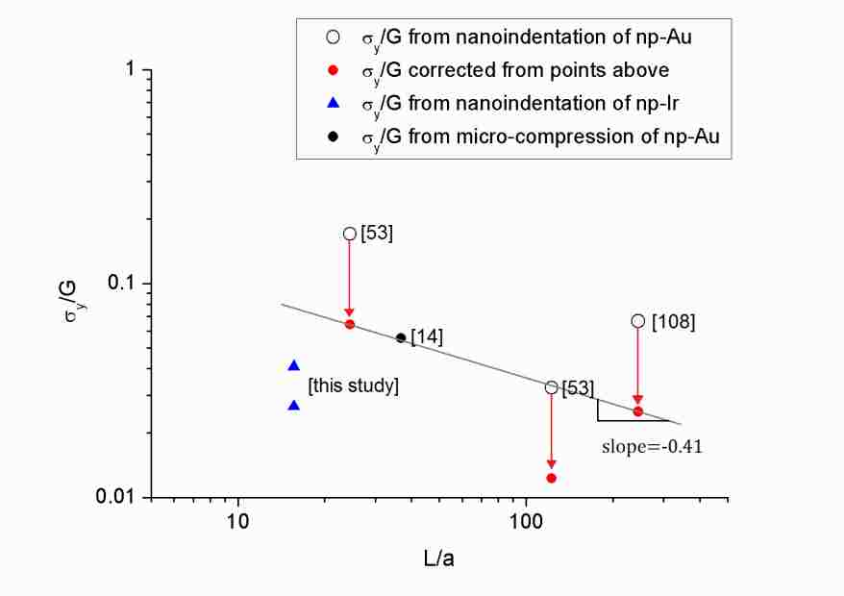

Figure 7.4. Log-log plot of σ_y/G vs. L/a. Data were from nanoindentation of np-Au, micro-compression test of np-Au, and nanoindentation of np-Ir. The referenced works are cited in the square bracket.

A linear extrapolation of the data from np-Au displayed in the plot as well. One point was not included in the fitting because it's far away deviated from other points. The fitted linear line had a slope of -0.41, which is close to -0.5. The trend of the linear fitting clearly displayed size effect to the ligament strength. But the data of nanoindentation of np-Ir was below this linear line. It implied the yield strength determined in this study is not as significantly high as those reported in mechanical tests of np-Au.

7.5 Conclusions and future work

The following conclusions can be made for this project,

1) Bulk np-Ir sample was fabricated by dealloying IrNi precursor. Due to intense dealloying in grain boundaries, dealloyed sample suffered from serious cracking.

2) Dealloying of bulk IrNi sample was finished by free corrosion with extended dealloying time (weeks or months). Electrochemical dealloying of bulk IrNi

sample was not employed due to the difficulty to find a container which can survive in 1.2V polarized electrolyte.

3) Strength of np-Ir was investigated by nanoindentation hardness test. The calculated yield strength is 5.6 GPa or 8.6 GPa. Considering size effect due to the extremely small ligaments, this value is reasonable.

Future work should be in improving dealloying to get crack-free bulk np-Ir. As discussed in previous section, single crystal IrNi may have to be used to solve this problem. Additionally, electrochemical dealloying could be feasible if the container to keep the IrNi sample is made of Ir, e.g., using Ir plate or Ir wire to hold the sample. Generally, more efforts should focus on avoiding cracking and also reducing dealloying time.

On the other hand, with crack-free bulk np-Ir samples, more mechanical tests can be carried out. With the micro-test machine available, tensile test and compression test can be used to directly measure yield strength, and then compare with that measured by nanoindentation.

Moreover, bulk np-Ir with different relative density can be achieved by dealloying precursor alloy with different compositions. By measuring yield strength (probably also ligament size), scaling equation for yield strength can be evaluated the same way as that for elastic modulus in Chapter 6.

8 Conclusions and future work

This doctoral work included the study of two nanoporous metal systems namely np-Ni and np-Ir. Significant findings were made on improving the fabrication of nanoporous metals by utilizing dealloying process. Mechanical behavior of np metals was further explored by thermal cycling experiments. The mechanical properties of np metals were compared with those of their dense counterparts to investigate the scaling behavior of np metals. In summary, the following was established during the course of these projects:

1) Thin film nanoporous nickel (np-Ni) with fine ligaments and high purity was synthesized from a Ni-Mg precursor. The relatively straightforward process of dealloying produced a crack-free nanoporous structure with ligaments and pores in the order of 7 nm.

2) It was discovered that Np-Ni ligaments have a native oxide coating but a metallic Ni core. This is a consequence of Ni's tendency to form a thin, protective native oxide, and does not hamper its ability as a catalyst. Instead, np-Ni in thin film would allow it to be applied as a (conformal) coating for specific surface, as opposed to the powder or slurry forms to which Raney Ni is restricted.

3) Thin film nanoporous iridium (np-Ir) with fine ligaments and high purity was fabricated from both Ir-Mg and Ir-Ni precursors. Dealloying Ir-Mg was found to be more effective because Mg etches very easily. However, dealloying Ir-Ni resulted in np-Ir with very limited thickness contraction.

4) A novel method to make layered np-metals by dealloying multilayer precursor was developed. This method was utilized to successfully fabricate np-Au and np-Ir, with controllable ligament, cell sizes, and even orientation. The unique feature

of multilayer fabrication would benefit applications which require nanoscale structure with high surface area as well as controlled length scale.

5) The thermomechanical behavior of np-Ir was investigated by thermal cycling of multilayer np-Ir films. Biaxial elastic moduli for np-Ir with different values of relative density were obtained from sequential thermal cycles, and were then used to determine the elastic scaling behavior of np-Ir. An updated scaling equation, with an exponent of 1.60, was determined for this nanoporous system.

6) A scaling equation describing the elastic behavior of porous materials with moderate relative density was determined by re-evaluating the classical Gibson and Ashby's unit cell model. The deformation of the structural beams (ligaments) were treated by considering both bending and compression/tension deformation. Relevant values of relative density were considered for nanoporous metals (0.28-0.50). The deduced scaling equation included an exponent of 1.52, which agreed very well with the experimental results.

One of key findings of the present work is a multilayer fabrication method to produce nanoporous metals with controllable ligament size and orientation. This key finding suggests that thin film np metals other than np-Ir should be fabricated in a similar manner. This ability to design nanoporous structures with predictable sizes and orientations could be used to improve properties which are highly sensitive to structure/size. For example, porous Si is an important optical materials, and if making it in multilayer structure, it can be used for wave-guide. The most commonly used fabrication method is to anodize Si wafer, by which layer spacing and pore size can be controlled by adjusting current

density. This multilayer fabrication method provides an alternative approach to fabricate layered porous materials. Compared with anodizing Si, it's more predictable and costless, and can achieve nanoscale pore size and layer spacing (typical layer spacing in anodized layered porous Si is in micrometer length).

Another key finding of this work is an updated scaling equation for elastic modulus. This scaling equation agreed well with the experimental scaling equation determined by thermal cycling of np-Ir thin film. Thermal cycling could be applied to other np metals, to determine biaxial moduli for np metal thin films with different relative densities. These measurements could further verify or improve the scaling equation established in this study.

Additionally, with newly available instruments, i.e. nanoindentation (in Dr. Cheng's group) and micro-test system (in Dr. Balk's group), multiple mechanical tests can be performed to determine mechanical properties of bulk np metals, including both yield strength and elastic modulus. Sample preparation for nanoindentation is simple, but the yield strength or elastic modulus cannot be directly measured by it. Therefore, micro-test (micro tensile or compressive test) is recommended. By measuring yield strength of bulk np metals e.g., np-Ir, in tensile or compressive tests with a variety of relative densities, an experimentally determined scaling equation for yield strength can be obtained. Further steps can be taken to derive scaling equations for yield strength, by utilizing the unit cell model (in Figure 6.13 or modified unit cell in Figure 6.16).

References

1. Cao, G. and Y. Wang, in *Nanostructures and Nanomaterials - Synthesis, Properties and Applications*, World Scientific.
2. Pavlic, A.A. and H. Adkins, *Preparation of a Raney Nickel Catalyst.* Journal of the American Chemical Society, 1946. **68**(8): p. 1471-1471.
3. Zielasek, V., et al., *Gold Catalysts: Nanoporous Gold Foams.* Angewandte Chemie International Edition, 2006. **45**(48): p. 8241-8244.
4. Liu, Z. and P.C. Searson, *Single Nanoporous Gold Nanowire Sensors.* Journal of Physical Chemistry B, 2006. **110**(9): p. 4318-4322.
5. Jin, H.-J., et al., *Nanoporous Au–Pt Alloys As Large Strain Electrochemical Actuators.* Nano Letters, 2009. **10**(1): p. 187-194.
6. Lang, X.Y., et al., *Three-dimensional nanoporous gold for electrochemical supercapacitors.* Scripta Materialia, 2011. **64**(9): p. 923-926.
7. Raney, M., *Method of producing finely-divided nickel*, U.S.P. 1628190, Editor 1927.
8. Pickering, H.W. and P.R. Swann, *Electron Metallography of Chemical Attack upon Some Alloys Susceptible to Stress Corrosion Cracking.* CORROSION, 1963. **19**(11): p. 373T-389T.
9. Pugh, D., A. Dursun, and S. Corcoran, *Formation of nanoporous platinum by selective dissolution of Cu from Cu0. 75Pt0. 25.* Journal of materials research, 2003. **18**(1): p. 216-221.
10. Zhang, Z., et al., *Generalized Fabrication of Nanoporous Metals (Au, Pd, Pt, Ag, and Cu) through Chemical Dealloying.* Journal of Physical Chemistry C, 2009. **113**(29): p. 12629-12636.
11. Li, Y. and A. Antoniou, *Synthesis of transversely isotropic nanoporous platinum.* Scripta Materialia, 2012. **66**(8): p. 503-506.
12. Li, W.-C. and T.J. Balk, *Preparation and Hydrogen Absorption/Desorption of Nanoporous Palladium Thin Films.* Materials, 2009. **2**(4): p. 2496-2509.
13. Li, R. and K. Sieradzki, *Ductile-brittle transition in random porous Au.* Phys. Rev. Lett., 1992. **68**: p. 1168-1171.
14. Volkert, C.A., *Approaching the theoretical strength in nanoporous Au.* Appl. Phys. Lett., 2006. **89**(6): p. 061920.
15. Biener, J., et al., *Nanoporous Au: A high yield strength material.* Journal of Applied Physics, 2005. **97**(2): p. 024301-024301-4.
16. Briot, N.J., et al., *Mechanical properties of single crystalling nanoporous gold investigated by small-scale tension and compressiont testing.* Philos. Mag., in review.
17. Hodge, A.M., et al., *Characterization and Mechanical Behavior of Nanoporous Gold.* Advanced Engineering Materials, 2006. **8**(9): p. 853-857.
18. Lu, G.Q. and X.S. Zhao, *Nanoporous Materials - Science and Engineering*, World Scientific.
19. Fujita, T., et al., *Unusually Small Electrical Resistance of Three-Dimensional Nanoporous Gold in External Magnetic Fields.* Physical Review Letters, 2008. **101**(16): p. 166601.
20. Ding, Y. and M. Chen, *Nanoporous Metals for Catalytic and Optical Applications.* MRS Bulletin, 2009. **34**(08): p. 569-576.
21. Fujita, T., et al., *Three-dimensional morphology of nanoporous gold.* Applied Physics Letters, 2008. **92**(25): p. 251902.
22. Sun, Y., *Linking the structure and mechanical behavior of nanoporous gold*, in *Chemical and Materials Engineering*2008, University of Kentucky. p. 156.
23. Wang, L. and T.J. Balk, *Thermal Cycling of Nanoporous Iridium Thin Films and a Modified Scaling Equation Describing Their Elastic Behavior*, in *Acta Materialia*.

24. Li, A.P., et al., *Hexagonal pore arrays with a 50-420 nm interpore distance formed by self-organization in anodic alumina.* Journal of Applied Physics, 1998. **84**(11): p. 6023-6026.
25. Liao, C.L., et al., *Fabrication of nanoporous metal electrode by two-step replication technique.* Journal of Alloys and Compounds, 2007. **441**(1–2): p. L1-L6.
26. Sun, L., C.-L. Chien, and P.C. Searson, *Fabrication of Nanoporous Nickel by Electrochemical Dealloying.* Chemistry of Materials, 2004. **16**(16): p. 3125-3129.
27. Erlebacher, J., *An atomistic description of dealloying porosity evolution, the critical potential, and rate-limiting behavior.* Journal of the Electrochemical Society, 2004. **151**(10): p. C614-C626.
28. Raney, M., *Method of producing finely-divided nickel*, U.s.p. office, Editor 1927: U.S.
29. Pickering, H.W. and P.R. Swann, *Electron metallography of chemical attack on some alloys susceptible to stress-corrosion cracking.* Corrosion (Houston, TX, U. S.), 1963. **19**(11): p. 373t-389t.
30. Swann, P.R. and H.W. Pickering, *Implications of the stress aging yield phenomenon with regard to stress corrosion.* Corrosion (Houston, TX, U. S.), 1963. **19**(11): p. 369t-372t.
31. Forty, A.J., *Corrosion micromorphology of noble metal alloys and depletion gilding.* Nature (London), 1979. **282**(5739): p. 597-8.
32. Sieradzki, K., et al., *The Dealloying Critical Potential.* Journal of The Electrochemical Society, 2002. **149**(8): p. B370-B377.
33. Newman, R., et al., *Alloy corrosion.* MRS BULLETIN-MATERIALS RESEARCH SOCIETY, 1999. **24**: p. 24-28.
34. Pugh, D.V., A. Dursun, and S.G. Corcoran, *Formation of nanoporous platinum by selective dissolution of Cu from Cu0.75Pt0.25.* Journal of Materials Research, 2003. **18**(1): p. 216-221.
35. Kabius, B., H. Kaiser, and H. Kaesche, *Micromorphological Study of Selective Dissolution of Cu from CuPd-Alloys.* Proceedings - The Electrochemical Society, 1986. **86-7**: p. 562-573.
36. Zhang, Z.H., et al., *Generalized Fabrication of Nanoporous Metals (Au, Pd, Pt, Ag, and Cu) through Chemical Dealloying.* Journal of Physical Chemistry C, 2009. **113**(29): p. 12629-12636.
37. König, T., *Fabrication and characterization nanoporous iridium in thin films*, in *Institution of materials science*2009, University of Karlsruhe: Karlsruhe.
38. Hakamada, M. and M. Mabuchi, *Preparation of nanoporous Ni and Ni-Cu by dealloying of rolled Ni-Mn and Ni-Cu-Mn alloys.* J. Alloys Compd., 2009. **485**(1-2): p. 583-587.
39. Erlebacher, J., et al., *Evolution of nanoporosity in dealloying.* Nature, 2001. **410**(6827): p. 450-3.
40. Yan, W., et al., *EPMA and XRD study on nickel metal thin film for temperature sensor.* Sensors and Actuators A: Physical, 2007. **136**(1): p. 212-215.
41. Kramer, D., R.N. Viswanath, and J. Weissmüller, *Surface-Stress Induced Macroscopic Bending of Nanoporous Gold Cantilevers.* Nano Letters, 2004. **4**(5): p. 793-796.
42. Kong, D.-S., et al., *Electrochemical fabrication of a porous nanostructured nickel hydroxide film electrode with superior pseudocapacitive performance.* Journal of Alloys and Compounds, 2011. **509**(18): p. 5611-5616.
43. Park, S., et al., *Structural and electrochemical features of 3D nanoporous platinum electrodes.* Electrochimica Acta, 2010. **55**(6): p. 2029-2035.
44. Wittstock, A., et al., *Nanoporous Au: An Unsupported Pure Gold Catalyst?* Journal of Physical Chemistry C, 2009. **113**(14): p. 5593-5600.

45. J. Zhang, C.M.L., *Nanoporous metals: fabrication strategies and advanced electrochemical applications in catalysis, sensing and energy systems.* Chem. Soc. Rev., 2012. **41**: p. 7016=7031.
46. Attard, G.S., et al., *Mesoporous Platinum Films from Lyotropic Liquid Crystalline Phases.* Science, 1997. **278**(5339): p. 838-840.
47. Meng, F. and Y. Ding, *Sub-Micrometer-Thick All-Solid-State Supercapacitors with High Power and Energy Densities.* Advanced Materials, 2011. **23**(35): p. 4098-4102.
48. Lu, Q., et al., *Supercapacitor Electrodes with High-Energy and Power Densities Prepared from Monolithic NiO/Ni Nanocomposites.* Angewandte Chemie, 2011. **123**(30): p. 6979-6982.
49. Arthur, T.S., et al., *Three-dimensional electrodes and battery architectures.* MRS Bulletin, 2011. **36**(07): p. 523-531.
50. Warren, W.E. and A.M. Kraynik, *Foam mechanics: the linear elastic response of two-dimensional spatially periodic cellular materials.* Mechanics of Materials, 1987. **6**(1): p. 27-37.
51. Gibson, L.J., et al., *The Mechanics of Two-Dimensional Cellular Materials.* Proceedings of the Royal Society of London series A, 1982. **382**(1782): p. 25-42.
52. Gibson, L.J. and M.F. Ashby, *The Mechanics of Three-Dimensional Cellular Materials.* Proceedings of the Royal Society of London Series A, 1982. **382**(1782): p. 43-59.
53. Gibson, L.J. and M.F. Ashby, *Cellular Solids- Structure and Properties*. Second ed. 1997: Cambidge.
54. Volkert, C.A., et al., *Approaching the theoretical strength in nanoporous Au.* Applied Physics Letters, 2006. **89**(6): p. 061920.
55. Biener, J., et al., *Size Effects on the Mechanical Behavior of Nanoporous Au.* Nano Letters, 2006. **6**(10): p. 2379-2382.
56. Ding, Y., Y.-J. Kim, and J. Erlebacher, *Nanoporous Gold Leaf: ldquoAncient Technologyrdquo/Advanced Material.* Advanced Materials, 2004. **16**(21): p. 1897-1900.
57. Sun, Y., et al., *The mechanical behavior of nanoporous gold thin films.* JOM Journal of the Minerals, Metals and Materials Society, 2007. **59**(9): p. 54-58.
58. Ohring, M., *Materials Science of Thin Films- Deposition& Structure*. Second ed. 2002: Academic Press.
59. Vilchez, J.B. *Scheme of the Burgers` vector in edge and screw dislocations*. 2008; Available from: http://en.wikipedia.org/wiki/File:Vector_de_Burgers.PNG.
60. Erlebacher, J., et al., *Evolution of nanoporosity in dealloying.* Nature, 2001. **410**(6827): p. 450-453.
61. Smith, W.F., *Foundations of Materials Science and Engineering*. 2006, New York: McGraw-Hill.
62. Youssef, K.M., et al., *Ultrahigh strength and high ductility of bulk nanocrystalline copper.* Applied Physics Letters, 2005. **87**(9): p. 091904-3.
63. Hodge, A.M., et al., *Scaling equation for yield strength of nanoporous open-cell foams.* Acta Materialia, 2007. **55**(4): p. 1343-1349.
64. Schiøtz, J., F.D. Di Tolla, and K.W. Jacobsen, *Softening of nanocrystalline metals at very small grain sizes.* System, 1977. **214**: p. 300-315.
65. Kadau, K., et al., *Molecular-dynamics study of mechanical deformation in nano-crystalline aluminum.* Metallurgical and Materials Transactions A, 2004. **35**(9): p. 2719-2723.
66. Conrad, H. and J. Narayan, *On the grain size softening in nanocrystalline materials.* Scripta Materialia, 2000. **42**(11): p. 1025-1030.

67. Dao, M., et al., *Toward a quantitative understanding of mechanical behavior of nanocrystalline metals.* Acta Materialia, 2007. **55**(12): p. 4041-4065.
68. Freel, J., W.J.M. Pieters, and R.B. Anderson, *The structure of Raney nickel: I. Pore structure.* Journal of Catalysis, 1969. **14**(3): p. 247-256.
69. Al-Saleh, M.A., et al., *Novel methods of stabilization of Raney-Nickel catalyst for fuel-cell electrodes.* Journal of Power Sources, 1998. **72**(2): p. 159-164.
70. Sun, L., C.-L. Chien, and P.C. Searson, *Fabrication of Nanoporous Nickel by Electrochemical Dealloying.* Chem. Mater., 2004. **16**(16): p. 3125-3129.
71. Mathieu, H.J., M. Datta, and D. Landolt, *Thickness of natural oxide films determined by AES and XPS with/without sputtering.* Journal of Vacuum Science & Technology A: Vacuum, Surfaces, and Films, 1985. **3**(2): p. 331-335.
72. Erlebacher, J. and K. Sieradzki, *Pattern formation during dealloying.* Scripta Materialia, 2003. **49**(10): p. 991-996.
73. Cullity, B.D. and S.R. Stock, *Elements of X-Ray Diffraction (3rd Edition)*. 2001: Prentice Hall.
74. Cortie, M.B., A.I. Maaroof, and G.B. Smith, *Electrochemical capacitance of mesoporous gold.* Gold Bulletin, 2005. **38**(1): p. 14-22.
75. Zhao, C., et al., *Fabrication and characterization of monolithic nanoporous copper through chemical dealloying of Mg–Cu alloys.* Corrosion Science, 2009. **51**(9): p. 2120-2125.
76. Zhang, C., et al., *Formation and microstructure of nanoporous silver by dealloying rapidly solidified Zn–Ag alloys.* Electrochimica Acta, 2012. **63**(0): p. 302-311.
77. Wagner, C.D., *Handbook of x-ray photoelectron spectroscopy: a reference book of standard data for use in x-ray photoelectron spectrocopy*. Vol. 190. 1979: Perkin Elmer.
78. Kong, D.-S., et al., *Electrochemical fabrication of a porous nanostructured nickel hydroxide film electrode with superior pseudocapacitive performance.* J. Alloys Compd., 2011. **509**(18): p. 5611-5616.
79. Weatherbee, G.D. and C.H. Bartholomew, *Effects of support on hydrogen adsorption/desorption kinetics of nickel.* Journal of Catalysis, 1984. **87**(1): p. 55-65.
80. Liu, C.L., et al., *EAM Study Of Surface Self-Diffusion Of Single Adatoms Of FCC Metals Ni, Cu, Al, Ag, Au, Pd, And Pt.* Surface Science, 1991. **253**(1-3): p. 334-344.
81. Tung, R.T. and W.R. Graham, *Single atom self-diffusion on nickel surfaces.* Surface Science, 1980. **97**(1): p. 73-87.
82. Canon, R.F. and J.P. Stark, *Grain Boundary Self-Diffusion in Nickel.* Journal of Applied Physics, 1969. **40**(11): p. 4366-4373.
83. Wazzan, A.R., *Lattice and Grain Boundary Self‐Diffusion in Nickel.* Journal of Applied Physics, 1965. **36**(11): p. 3596-3599.
84. Li, F., L. Zhang, and R.M. Metzger, *On the Growth of Highly Ordered Pores in Anodized Aluminum Oxide.* Chemistry of Materials, 1998. **10**(9): p. 2470-2480.
85. Loni, A., et al., *Porous silicon multilayer optical waveguides.* Thin Solid Films, 1996. **276**(1–2): p. 143-146.
86. Hakamada, M. and M. Mabuchi, *Fabrication of nanoporous palladium by dealloying and its thermal coarsening.* Journal of Alloys and Compounds, 2009. **479**(1–2): p. 326-329.
87. Li, W.C. and T.J. Balk, *Achieving finer pores and ligaments in nanoporous palladium–nickel thin films.* Scripta Materialia, 2010. **62**(3): p. 167-169.
88. Li, W.-C. and T.J. Balk, *Transition from single- to multi-layered structures in nanoporous gold–palladium ultrathin films.* Thin Solid Films, 2011. **519**(8): p. 2393-2397.
89. Göbel, H. and P. von Blanckenhagen, *A study of surface diffusion on gold with an atomic force microscope.* Surface Science, 1995. **331–333, Part B**(0): p. 885-890.

90. Fu, T.-Y., Y.-R. Tzeng, and T.T. Tsong, *Self-diffusion and dynamic behavior of atoms at step edges of iridium surfaces.* Physical Review B, 1996. **54**(8): p. 5932-5939.
91. Kong, T., *Fabricaiton and characterization of nanoporou iridium in thin films*, 2009.
92. Okada, Y. and Y. Tokumaru, *Precise determination of lattice parameter and thermal expansion coefficient of silicon between 300 and 1500 K.* Journal of Applied Physics, 1984. **56**(2): p. 314-320.
93. Halvorson, J.J. and R.T. Wimber, *Thermal Expansion of Iridium at High Temperatures.* Journal of Applied Physics, 1972. **43**(6): p. 2519-2522.
94. Gale, W.F. and T.C. Totemeier, *Smithells Metals Reference Book* 8th ed. 2004: Elsevier.
95. Hunt, L., *A History of Iridium.* Platinum Metals Review, 1987. **31**(1): p. 32-41.
96. Sun, Y., *Linking the structure and mechanical behavior of nanoporous gold*, in *Chemical and Materials Engineering*2008, Univeristy of Kentucky.
97. Roberts, A.P. and E.J. Garboczi, *Elastic properties of model random three-dimensional open-cell solids.* Journal of the Mechanics and Physics of Solids, 2002. **50**(1): p. 33-55.
98. Xi-Qiao, F., et al., *Surface effects on the elastic modulus of nanoporous materials.* Applied Physics Letters, 2009. **94**(1): p. 011916-011916-3.
99. Liu, R. and A. Antoniou, *A relationship between the geometrical structure of a nanoporous metal foam and its modulus.* Acta Materialia, 2013. **61**(7): p. 2390-2402.
100. Biener, J., A.M. Hodge, and A.V. Hamza, *Microscopic failure behavior of nanoporous gold.* Applied Physics Letters, 2005. **87**(12): p. 121908-121908-3.
101. Balk, T.J., et al., *Tensile and compressive microspecimen testing of bulk nanoporous gold.* JOM, 2009. **61**(12): p. 26-31.
102. Brookes, C.A., J.H. Greenwood, and J.L. Routbort, *Brittle Fracture in Iridium Single Crystals.* Journal of Applied Physics, 1968. **39**(5): p. 2391-2395.
103. Cawkwell, M.J., et al., *Origin of brittle cleavage in iridium.* Science, 2005. **309**(5737): p. 1059-1062.
104. Hecker, S., D. Rohr, and D. Stein, *Brittle fracture in iridium.* Metallurgical Transactions A, 1978. **9**(4): p. 481-488.
105. Panfilov, P. and A. Yermakov, *On brittle fracture in polycrystalline iridium.* Journal of Materials Science, 2004. **39**(14): p. 4543-4552.
106. Östlund, F., et al., *Brittle-to-Ductile Transition in Uniaxial Compression of Silicon Pillars at Room Temperature.* Advanced Functional Materials, 2009. **19**(15): p. 2439-2444.
107. Cahoon, J.R., W.H. Broughton, and A.R. Kutzak, *The determination of yield strength from hardness measurements.* Metallurgical Transactions, 1971. **2**(7): p. 1979-1983.
108. Hakamada, M. and M. Mabuchi, *Mechanical strength of nanoporous gold fabricated by dealloying.* Scripta Materialia, 2007. **56**(11): p. 1003-1006.
109. Shaw, M.C. and T. Sata, *The plastic behavior of cellular materials.* International Journal of Mechanical Sciences, 1966. **8**(7): p. 469-478.
110. Yermakov, A., P. Panfilov, and R. Adamesku, *The main features of plastic deformation of iridium single crystals.* Journal of Materials Science Letters, 1990. **9**(6): p. 696-697.
111. Balk, T.J., K.J. Hemker, and L.P. Kubin, *On anomalous strain hardening in iridium crystals.* Scripta Materialia, 2007. **56**(5): p. 389-392.

Vita of Lei Wang

Lei Wang was born in Yuncheng, Shanxi, China. She graduated from University of Science and Technology Beijing with a Bachelor's degree of Science in Materials Science and Engineering in 2007. In 2008, she joined Dr. Balk's group in University of Kentucky to start a PhD study in Materials Science and Engineering.

Papers

1. Wang, L., Briot N., Swartzentruber P., and T.J. Balk, *Magnesium Alloy Precursor Thin films for Efficient, Practical Fabrication of Nanoporous Metals*. Metall. Mater. Trans. A, 2013, in press.

2. Wang, L. and T.J. Balk, *Thermal Cycling of Nanoporous Iridium Thin Films and a Modified Scaling Equation Describing Their Elastic Behavior*. Acta Materialia, under review.

3. Wang, L. and T.J. Balk, *Synthesis of Nanoporous Nickel Thin Film from Various Precursors*. Philos. Mag. Lett., under review.

4. Wang, L. and T.J. Balk, *Using multilayer precursors to create nanoporous gold and nanoporous iridium thin films with layered architecture*. Metall. Mater. Trans. A, under review.

Presentations in Conferences

1. Wang, L., and T. J. Balk, *Fabrication of Nanoporous Nickel as An Alternative To Raney Nickel* (Poster). Kentucky Innovation & Enterpreneurship Conference (KIEC), 2009, 2010, and 2011.

2. Wang, L., Scherwitz M., and T.J. Balk, *Thermal Cycling and Stress Relaxation of Nanoporous Nickel Thin Films* (Poster). Gordon Conference, 2010.

3. Wang, L., Jiang X., and T.J. Balk, *Structure and Thermal-Mechanical Behavior Study of Nanoporous Nickel Thin Films* (Talk). TMS, 2012.

4. Wang, L., and T.J. Balk, *Fabrication and Mechanical Behavior Study of Nanoporous Iridium* (Poster). TMS, 2013.

5. Jiang, X., Tochigi E., Minor A., and Balk T.J., *Mechanical Behavior of Nanoporous Silicon Subjected to Extensive Deformation* (Talk, given by Lei Wang). TMS, 2013.

6. Wang, L., and T.J. Balk, *Fabrication and Characterization of Multilayer Nanoporous films* (Talk). TMS, 2014.

7. Briot, N., Wang, L., and T.J. Balk, *Mechanical Properties and Scaling Behavior of Bulk Nanoporous Gold and Iridium* (Talk). TMS, 2014.